Title
Validations of Computational Codes of Molten Salt Reactors

Author
Shen, Dan

Publication Date
2019

Peer reviewed|Thesis/dissertation

Validations of Computational Codes of Molten Salt Reactors

by

Dan Shen

A dissertation submitted in partial satisfaction of the

requirements for the degree of

Doctor of Philosophy

in

Engineering - Nuclear Engineering

in the

Graduate Division

of the

University of California, Berkeley

Committee in charge:

Professor Massimiliano Fratoni, Chair
Professor Per F. Peterson
Professor Haiyan Huang

Fall 2019

Validations of Computational Codes of Molten Salt Reactors

Dan Shen

Abstract

Validations of Computational Codes of Molten Salt Reactors

by

Dan Shen

Doctor of Philosophy in Engineering - Nuclear Engineering

University of California, Berkeley

Professor Massimiliano Fratoni, Chair

As one of the six advanced reactor concepts selected by the 2002 Generation IV roadmap as a technology meriting future research, Molten Salt Reactors (MSRs) attracted broad attention and multiple private and public entities are working towards its commercialization. Facing stringent regulatory requirements, validations of computational codes used to calculate and prove the safety characteristics of MSRs play a key role.

This project developed the world-first, MSR-related reactor physics benchmark basing on the series of zero-power experiments of the Molten Salt Reactor Experiment (MSRE) for the International Reactor Physics Experiment Evaluation Project (IRPhEP) handbook, in order to fill the knowledge gap of MSR benchmarking.

The role of the MSRE was to demonstrate the practicality of this high-temperature fluid-fuel reactor concept. Design of the MSRE was initiated at the Oak Ridge National Laboratory (ORNL) in 1960. It was a successful experiment, demonstrating key features of the liquid-fuel MSR, enhancing confidence in the practicality and performance of MSRs and leaving numerous experimental data from nuclear operation.

To reconstruct the MSRE, a three-dimensional high-fidelity benchmark model was developed by Monte Carlo neutron transport code Serpent2 with new methods developed to account for the unique feature of fuel salt motion in the core. The calculated effective multiplication factor, k_{eff}, for the criticality experiment, when ^{235}U was progressively added to the fuel salt in order to achieve criticality with stationary salt and isothermal conditions, was 1.02132 ($\pm$3 pcm). The total uncertainty for experimental k_{eff} was estimated to be 420 pcm. The calculated k_{eff} is 2.154% larger than the experimental and benchmark model value, which is approximately 5 times the benchmark model uncertainty. It is to be noted that, for systems containing large volume of graphite (or other carbonaceous materials), Monte Carlo codes tend to overestimate the k_{eff} of the benchmark model by 1% to 2%. The bias is possibly due to uncertainties in the impurity content of the graphite blocks, the accuracy of the neutron

capture cross section of carbon and the accuracy to model the nuclear-grade graphite.

The calculated reactivity coefficient of ^{235}U concentration on the MSRE benchmark model (0.2228 ± 0.0014, represented as the change of reactivity over the relative change of ^{235}U mass in loop) matches well with the experiment value (0.223 ± 0.006), strengthening the confidence of accurate representation of the fuel salt composition in the MSRE benchmark. Most of other reactivity effect calculations, including the control rod bank worth, reactivity effects of fuel circulation and isothermal and fuel temperature coefficients show good agreement with experiment values (within 1σ) as well.

This dissertation also illustrates the scenario of building a series of neutronics benchmarks for the Fluoride-salt-cooled High-temperature Reactor (FHR), a conceptual MSR without fueled experiments to compare. This is a code-to-code verification benchmark and can be used to verify the credibility of neutronics codes in modeling reactors with TRISO particle type fuel and a pebble bed geometry.

Acknowledgments

I would like to express my deepest appreciation to Professor Fratoni, my supervisor. The completion of my dissertation would not have been possible without his encouragement, support and guidance.

Special thanks to my parents, my husband and my son for supporting me spiritually all the time.

Contents

List of Figures

List of Tables

Chapter 1

Introduction

1.1 Background

1.1.1 Molten salt reactor

With the growing population on the earth and improved living standards for a better life, the demand for clean, safe and low-cost energy supplies is increasingly urgent, especially aiming to fight the global climate change. Nuclear energy is the prominent energy resource option that can supply reliable base load electricity in a large scale with very low carbon emission. Currently, most nuclear power plants in operation are Light Water Reactors (LWRs) that use light water as coolant and neutron moderator. The LWR brought the following safety concerns[8]:

- Danger of steam explosion (Chernobyl accident);
- Danger of pressure vessel failure due to high operating pressure;
- Danger of fuel melting due to high core afterheat during accidents (Three Mile Island and Fukushima accidents);
- Potential hydrogen generation during accidents (Fukushima accident).

Also, the thermal efficiency of LWRs (below 35%) is limited by the coolant outlet temperature. With the potential to alleviate all of these issues, in recent years, the Molten Salt Reactors (MSRs) have gathered worldwide interest by multiple private and public entities working towards the commercialization of such reactor concept. The MSR is one of the six advanced nuclear reactor concepts selected by the 2002 Generation IV roadmap as a technology meriting future research considering its performance in the four broad areas of sustainability, economics, safety and reliability, and proliferation resistance and physical

protection[7]. There are two primary variants of MSRs: 1) the liquid-fuel MSR with fuel dissolved in the circulating molten salt and 2) the solid-fuel MSR where salts only serve as the coolant. In both MSR designs, cooling is provided by high-temperature liquid-salt.

For thermal-spectrum MSRs, the ideal primary coolant salt should have low neutron absorption cross section, reasonable melting point and appropriate chemical characteristics. A summary of properties of several candidate coolant salts along with other traditional coolants are listed in Table 1.1. All coolant salts listed in Table 1.1 have high boiling points (up to 1430 °C) and melting points below 500 °C. Hence, MSRs could operate at high temperature ($\sim$ 700 °C), improving electrical generation efficiency to over 44%[8]. Serving as a good neutron moderator itself, FLiBe is the most neutronically favorable of all candidate salts which also has excellent thermal hydraulic characteristics such as the highest volumetric heat capacity. Compared to sodium, water, helium and other traditional coolants, FLiBe shows attractive properties as well, featuring high boiling point to be able to operate at atmospheric pressure and high temperature, high volumetric heat capacity to support high core power density, low neutron absorption rate with enriched ^{7}Li and so on.

Table 1.1: Physical properties of coolants (ρ = density, ρC_ρ = volumetric heat capacity, k = thermal conductivity, salt properties provided at 700 °C and 1 atm[9])

Coolant[a]	Melting point, °C	Boiling point, °C	ρ, kg/m^3	ρC_p KJ/m^3°C	k W/m°C
Li_2BeF_4 (FLiBe)	459	1430	1940	4670	1.0
59.5NaF-40.5ZrF_4	500	1290	3140	3670	0.49
26LiF-37NaF-37ZrF_4	436		2790	3500	0.53
31LiF-31NaF-38BeF_2	315	1400	2000	4080	1.0
8NaF-92$NaBF_4$	385	700	1750	2640	0.5
Sodium[b]	97.8	883	820	1040	62
Lead	328	1750	10540	1700	16
Helium (7.5 MPa)			3.8	20	0.29
Water (7.5 MPa)[c]	0	290	732	4040	0.56

[a] Salt compositions are shown in mole percent.
[b] Sodium properties are at 550 °C.
[c] Pressurized water data are shown at 290 °C for comparison.

Investigation of MSRs started in the late 1940s for aircraft propulsion[22]. The Aircraft Reactor Experiment (ARE) was built at Oak Ridge in 1954 in order to investigate and demonstrate MSR system's stability in high temperature operation. The ARE salt was a mixture of NaF, ZrF_4 and UF_4 with BeO as the moderator. After successfully operated for 100 hours, ARE was found to be stable which led to recognition of the potential of MSRs

for economical electricity production[13]. By 1960, many conceptual designs of MSRs had emerged and scientists at that time realized that another MSR experiment was needed to investigate some key technologies for this type of reactors.

The design of the 8MWth Molten Salt Reactor Experiment (MSRE) was begun in 1960 at the Oak Ridge National Laboratory (ORNL). The MSRE fuel salt, a mixture of uranium, lithium-7, beryllium, and zirconium fluorides, circulates through the primary loop where the unclad graphite lattice serves as the moderator and all other parts of the system exposed to salt are made from the nickel-base alloy, INOR-8, which was specially developed in the aircraft program for use with molten fluorides. Reactor heat was transferred from the fuel salt to a similar coolant salt and was then dissipated to the atmosphere.

The MSRE reactor equipment operated reliably: the salt handling is quite practical; there is practically no corrosion; the radioactive liquids and gases were contained safely and the system's performance was stable during operation[13]. The MSRE successfully demonstrated key features of the liquid-fuel MSR concept, resolving many issues related to the operation of MSRs, the stability of molten salt fuel and material compatibility. The MSRE enhanced confidence in the practicality and performance of MSR. It was shut down in 1969 after four years of operation because the technical feasibility and promise of MSR systems had been demonstrated and more funds were needed for further investigation[16].

Research on MSRs regained attention when a salt-cooled, solid-fuel MSR concept, the Advanced High-Temperature Reactor (AHTR), was designed in 2002 aiming to achieve very high core outlet temperature (750 to 1000 °C) for efficient electricity and thermochemical H_2 production[10]. The AHTR uses TRISO fuel particles (see Figure 1.1) similar to that used in High Temperature Gas-cooled Reactors (HTGRs) and a liquid-salt coolant. The uranium fuel kernel is coated with multiple layers of carbon and silicon carbide in order to prevent release of radionuclides at very high temperature. Even at 1600 °C, such design can prevent significant fission product release for hundreds of hours. The coated particles are incorporated into a graphite-matrix fuel compact that, in turn, is incorporated into a graphite-matrix fuel assembly with several shape options such as hexagonal block, pebble bed with small balls or long cylinders in order to support different design goals. Although TRISO particles are the preferred choice for high temperature operation, they cause high manufacturing cost and the dilute fuel loading generates small heavy metal loading. The use of solid-fuel and molten salt coolant in the AHTR, different from the MSRE where fissile materials and fission products were dissolved in the salt, minimize the radioactivity in the coolant and also minimize the system corrosion due to a "clean" salt. The AHTR also features improved inherent and passive safety characteristics.

As mentioned before, the MSR was selected among the six advanced reactor concepts by the 2002 Generation IV roadmap and since then, research and development of MSRs have been conducted worldwide such as the Pebble-Bed Fluoride-salt-cooled High-temperature Reactor

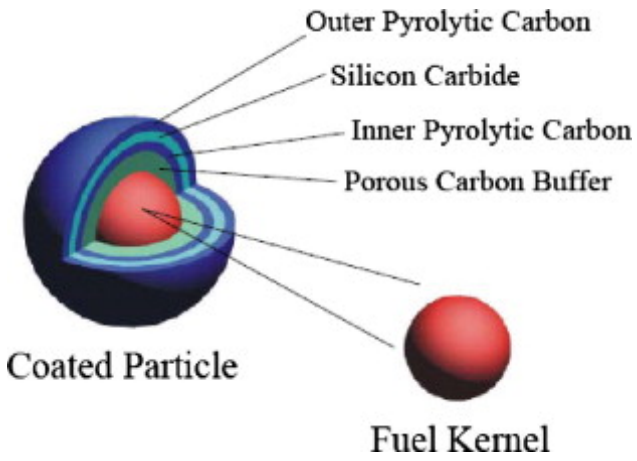

Figure 1.1: Illustrative cutaway drawing of a TRISO fuel particle[18].

(PB-FHR) designed by the University of California, Berkeley[23], the Thorium Molten Salt Reactor (TMSR) developed by the Shanghai Institute of Applied Physics (SINAP) since 2011[27], etc.

1.1.2 Computational code validation for neutronics physics

Although MSRs have many attractive characteristics, there are still many technology challenges remaining to be solved such as:

- The extreme radiation environment for liquid-fuel MSRs poses difficulty to operations and maintenance;
- Fuel salt chemistry control and material compatibility are research areas of vital importance;
- Tritium release problem requires support from tritium separation technology.

Perhaps more critically, there are limited validation benchmarks available for MSR modeling and no operating MSRs in the world. In order to support the licensing process of MSRs, it is necessary to validate the computational codes used to prove their safety characteristics.

A code-to-experiment validation can be achieved through a peer-reviewed, world-widely recognized reactor physics benchmark. The International Reactor Physics Experiment Evaluation Project (IRPhEP)[3], which was initiated as a pilot activity in 1999 by the Organization of Economic Cooperation and Development (OECD) Nuclear Energy Agency (NEA) Nuclear

Science Committee (NSC), collects reactor physics experimental data from nuclear facilities worldwide and evaluates those data to develop extensively peer-reviewed integral benchmark data sets. The benchmark included in the IRPhEP handbook can be used by the international nuclear data community for testing and improvement of nuclear data files and by the international reactor physics and computation communities for validation of analytical methodologies used for reactor safety analysis, design and advanced modeling efforts[4]. The 2019 edition of the IRPhEP handbook contains data from 166 different experimental series that were performed at 56 different nuclear facilities.

Although the experimental data from operation of the MSRE encouraged numerous benchmark attempts, no official benchmark was created for the IRPhEP handbook. On top of that, the IRPhEP handbook does not contain any benchmark related to MSR technology currently, which is a deficiency that has been specifically noted as a knowledge gap of high priority. The University of California, Berkeley and ORNL have collaborated to create the first MSR-type reactor physics benchmark based on the MSRE for the IRPhEP handbook, which will be available in the 2019 edition.

As an important part of this dissertation, research of the MSRE benchmark provides a peer-reviewed set of reactor physics data and a fully-detailed MSRE model for reactor designers and safety analysts to validate their analytical tools and establish the safety basis for MSRs. The final scope of this benchmark effort is to cover the full series of start-up zero-power experiments conducted in June 1965[19]. First of all, the initial criticality experiment determined the minimum ^{235}U concentration needed in the fuel salt in order to achieve criticality under the following conditions: core isothermal, fuel salt stationary and control rods withdrawn. The actual system power was about 10 W. Following the initial criticality experiment, more experiments were conducted to gather information on the following experimental parameters:

- The differential worth of one control rod as a function of position, both with the fuel salt stationary and with it circulating;
- The rod-drop effect which can provide an independent check of the integral worth of various control rod configurations;
- The rod-shadowing effect which reflects the change in the critical position of the regulating rod (rod No. 1) as the shim rods (rods No. 2 and No. 3) were inserted into the core;
- The ^{235}U concentration coefficient of reactivity;
- The effect of fuel salt circulation on reactivity;
- The isothermal temperature coefficients of reactivity;
- The pressure coefficient of reactivity.

1.2 Thesis scope and outline

The main objective of this dissertation is to validate the computational codes for MSR neutronics physics analysis through creating a series of neutronics benchmarks to make a code-to-experiment validation on a liquid-fuel MSR experiment, the MSRE.

The three-dimensional high-fidelity benchmark model for use in the MSRE benchmark was developed with Monte Carlo neutron transport code Serpent2[14] and multiple nuclear data evaluations (ENDF/B.VII and JENDL). Monte Carlo transport code simulates each particle's physical process independently as a probabilistic process and with this stochastic nature, it can model very complex geometries and guarantee high flexibility and accuracy required for the benchmark.

To accurately reproduce several reactivity effect measurements of the MSRE, new methods were developed basing on the Serpent2 model in order to account for unique features of the MSRE (for example, the fuel salt motion in the core). Uncertainty quantification is an essential part of an IRPhEP benchmark. The uncertainty caused by each important parameter in the benchmark model was evaluated independently. Also, with the new features developed in Serpent2 that is a collision history-based approach to calculate sensitivity and uncertainty[2], the sensitivity coefficients and total uncertainty for the k_{eff} from nuclear data uncertainties in each element in all the materials were quantified. Given the complexity of the MSRE benchmark model, it might be challenging for many codes to reproduce the full details of the model. Therefore, the impact of some geometry modification was provided as well.

Chapter 2 introduces the models and methodologies for benchmarks of the MSRE. After reconstructing the MSRE along with resolving inconsistency among different documentations, a fully-detailed MSRE model was created and the series of MSRE zero-power physics experiment were evaluated step by step. Novel methodologies were developed to model various reactivity effect experiments required in the benchmark.

Chapter 3 summarizes the code-to-experiment validations between Serpent2, combined with novel methodologies developed to account for unique characteristics in the MSRE benchmark model, and MSRE first zero-power experiments including the criticality experiment and control rod calibration experiments measuring the control rod worth, rod-drop effect, rod-shadowing effect, ^{235}U concentration coefficient of reactivity, effect of fuel salt circulation on reactivity and isothermal temperature coefficients at various ^{235}U concentration levels.

To further exploit MSR benchmark research, Chapter 4 introduces the benchmark work of FHR, which is a conceptual solid-fuel MSR without fueled experiments conducted to compare. Without code-to-experiment validation capability, early-stage benchmarking of FHR must rely heavily on code-to-code comparisons, also called code-to-code verification. The design of the FHR neutronics benchmark starts with a simple, infinite cell containing pebbles

and is examined with varying levels of homogenisation. These unit cell models focus on neutronically small systems with large leakages, which is a challenging problem for calculation methods used for reactor neutronics physics analysis. The second FHR benchmark scenario includes a graphite reflector and black boundaries to simulate a simplified reactor geometry in order to compare performance of computational codes in a full-core FHR case. The main concern of the FHR benchmark is to compare the key parameters such as k_{eff} calculated by different codes and to investigate the reasons for any differences in results.

At the end, Chapter 5 summarizes the conclusions and future work.

Chapter 2

Models and Methodologies

2.1 Overview of MSRE

2.1.1 MSRE reactor design features

The MSRE fuel-salt-circulating system is the reactor primary system which consists of the reactor vessel, the fuel circulating pump, the fuel heat exchanger, and the interconnecting piping, as illustrated in Figure 2.1 and Figure 2.2. The major components of this system are contained within the reactor cell, which is a cylindrical carbon steel vessel (7.32 m in diameter and 10.06 m in height), with a hemispherical bottom and a flat top. These components in the reactor cell are laid out in order to be removed by the use of long-handled tools from above[13]. During operation of the reactor, the fuel salt was circulated through the primary system at a rate of 4.54 m^3/min. Table 2.1 provides the volume of each component of the fuel loop and the time that fuel salts requires to flow through each section. Dry, deoxygenated helium gas at 5 psig blankets the fuel salt at the fuel pump bowl and also sweeps the highly radioactive xenon and krypton towards the off-gas disposal system. All metal components were electrically heated to keep the fuel salt molten in zero-power condition. Materials used in the MSRE are summarized in Table 2.2 and the composition of INOR-8 is shown in Table 2.3.

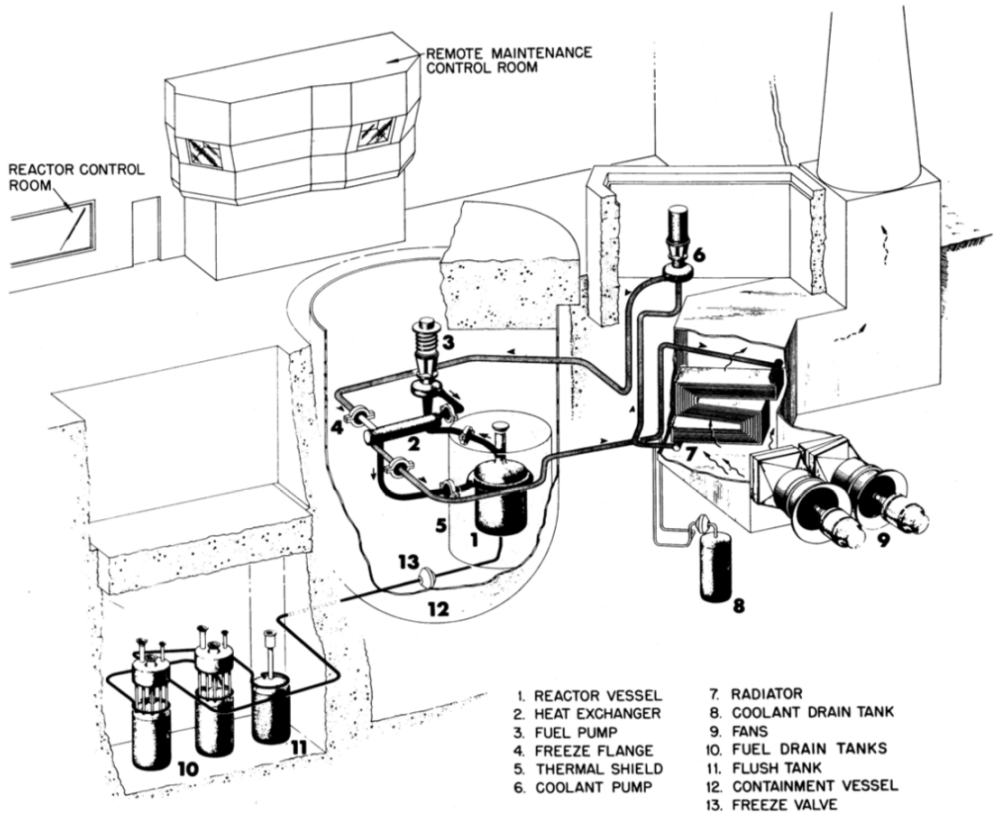

Figure 2.1: MSRE layout[21].

Table 2.1: Salt volume and salt residence times in the components of the fuel loop at 649 °C and 4.54 m^3/min, all values from [21]

Component	Volume, m^3	Time, s
Core	0.708	9.4
Upper head	0.297	3.9
Reactor vessel to pump	0.059	0.8
Pump bowl main stream	0.025	0.3
Pump bowl outside main stream	0.091	-
Pump to heat exchanger	0.023	0.3
Heat exchanger	0.173	2.3
Heat exchanger to reactor vessel	0.062	0.8
Vessel inlet	0.275	3.6
Lower head	0.283	3.8
Total in the fuel loop	1.996	25.2
Total in the fuel loop, drain line and drain tank heel	2.073	-

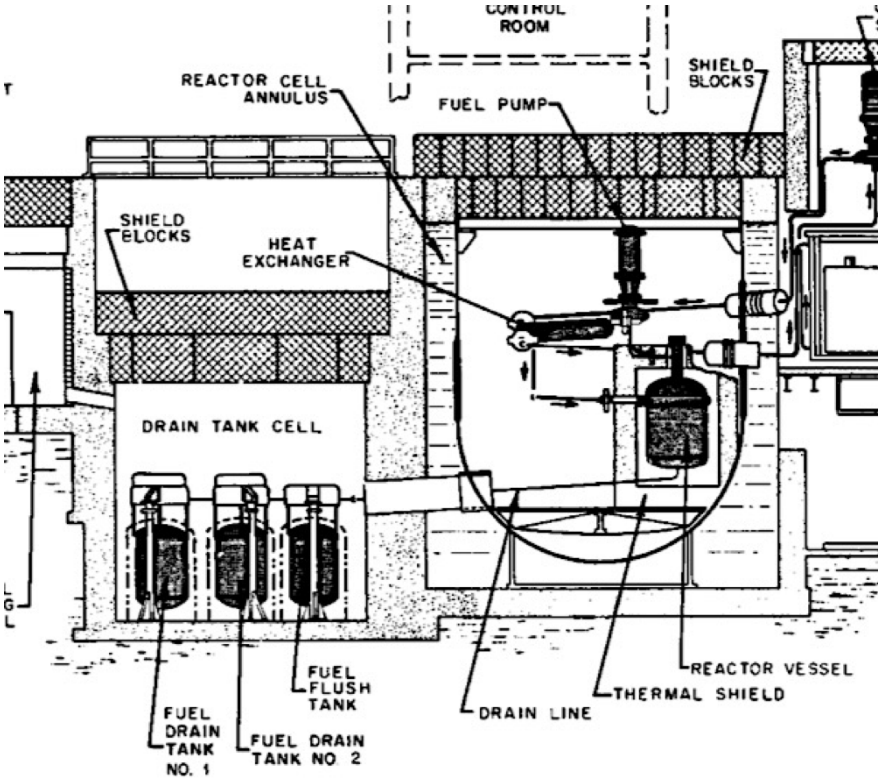

Figure 2.2: Vertical layout of the MSRE reactor cell and drain tank cell[21].

Table 2.2: Materials used in the MSRE[13]

Fuel Salt	LiF-BeF_2-ZrF_4-UF_4
Coolant salt	LiF-BeF_2
Moderator	Graphite
Salt containers	INOR-8
Cover gas	Helium

Table 2.3: Composition of INOR-8 used in the MSRE[21]

Element	Mass fraction,%
Ni	66-71
Mo	15-18
Cr	6-8
Fe, max	5
C	0.04-0.08
Ti + Al, max	0.50
S, max	0.02
Mn, max	1.0
Si, max	1.0
Cu, max	0.35
B, max	0.010
W, max	0.50
P, max	0.015
Co, max	0.20

The characteristics of the MSRE are illustrated as follows:

- The homogeneous liquid fuel salt allows online refueling, processing, and fission product removal, avoiding the high cost of fuel fabrication and the need to shut down the reactors for refueling. In addition, lower core excess reactivity can be maintained;
- Fissile materials and most fission products form stable fluorides in the fuel salt, decreasing the risk of severe radioactive release to the environment in an accident. The only exception is the noble metal group which does not form stable fluorides but was found to be plated out on graphite and alloy surfaces exposed to the salt or go into the cover gas above the fuel salt as a smoke or aerosol of sub-micron particles[13]. The high radiation level in the primary loop makes remote maintenance and interior shielding necessary. In the MSRE, there is a thermal shield with a thickness of 40.64 cm surrounding the reactor vessel. It contains 125 tons of steel balls and circulating water to absorb most of the energy of neutrons and gamma ray escaping the reactor vessel. In addition, the MSRE was under remote maintenance. As shown in Figure 2.1, the reactor primary loop and the drain tank system are shielded and installed in containment vessels while the heavily shielded remote maintenance control room is located above the operating floor[21];

- Fluoride salts have reasonably good heat transfer properties, are not damaged by radiation, do not react violently with air or water, and are inert to some common structural metals;
- The high coolant outlet temperature supports high-efficiency electricity production. In addition, the system operates at low pressure (about 5 psig), reducing the capital cost of the reactor vessel;
- The system has good neutron economy. The use of unclad graphite in the core and the rapid removal of gaseous fission products result in good fuel utilization, avoiding control problems of xenon poisoning as a bonus;
- Inherent safety in the MSRE is afforded by the design of freeze valves. Salt was introduced into the primary circulating system or drained from it through the vessel drain line running from the bottom of the reactor vessel (see Figure 2.3). The valve controlling the drain line is a freeze valve which was closed by a frozen plug of salt. When a drain is requested, the temperature of the freeze valve in the drain line will be increased and the frozen salt plug will be thawed in 10 to 15 min. A power failure accident can also result in a drain because the cooling air required to keep the valves frozen is interrupted[13].

The MSRE reactor vessel is compact, with an inner diameter of 147.32 cm and a height of 233.90 cm (as shown in Figure 2.3 and Figure 2.4). The fuel salt enters the flow distributor through the fuel inlet, which is arranged tangentially to the top of the vessel. The flow distributor is half-circular in cross section with an inside radius of 10.16 cm. The fuel is distributed evenly around the circumference of the vessel while passing the flow distributor and then flows turbulently downward in a spiral path through a 2.54-cm-wide annulus between the vessel wall and the core can. The salt loses its rotational motion in the 48 straightening vanes in the lower plenum and flows upward through the graphite matrix in the core can. Elimination of the swirl in the bottom head reduces the radial pressure gradient and promotes even flow distribution through the core.

The reactor vessel has two torispherical domes with 147.32-cm inner diameter and 2.54-cm thickness as the upper and lower plenum. The wall thickness of the cylindrical portion of the vessel is 1.429 cm, except for the top 40.64 cm of the vessel, which has a wall thickness of 2.54 cm. The core can, or core container, inside the vessel has an inner diameter of 140.97 cm and was rolled from 0.635-cm-thick INOR-8 plate. The core can is supported, and also held down when salt is in the reactor, by a ring at the top which is bolted to 36 lugs welded to the inside wall of the reactor vessel. The can, in turn, supports the graphite in the reactor.

The graphite matrix is an assembly of vertical stringers with a 5.08 cm by 5.08 cm cross section as shown in Figure 2.5. Fissioning occurs when the fuel salt flows through the

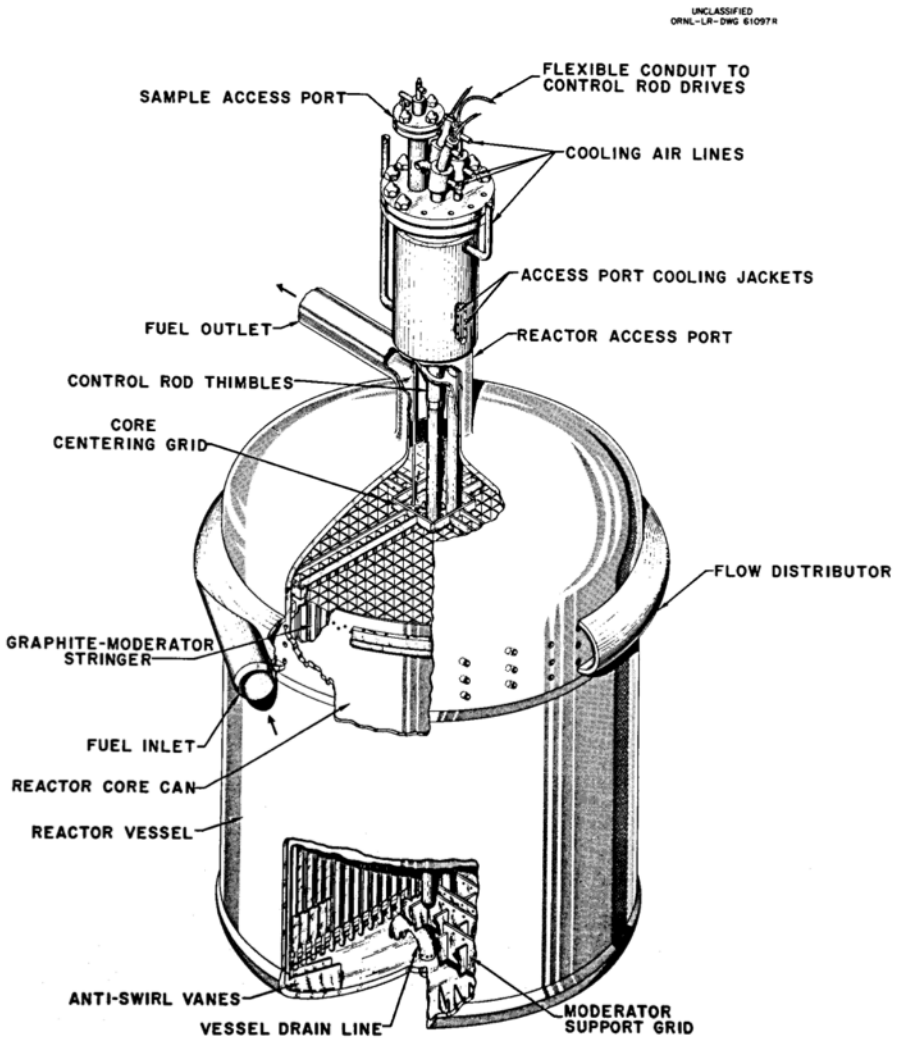

Figure 2.3: Cutaway of the MSRE reactor vessel[21].

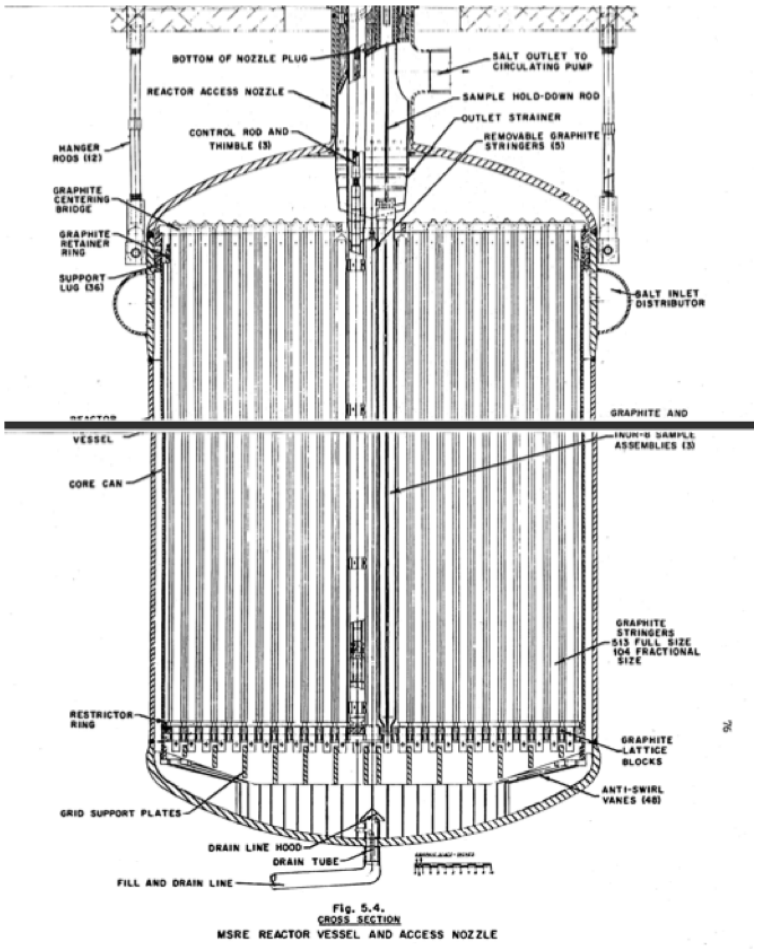

Figure 2.4: Vertical cross section of the MSRE vessel[21].

channels formed by grooves in the 4 sides on the stringers. These channels are 1.016 cm by 3.048 cm with round corners of radius 0.508 cm (see Figure 2.6). The graphite stringers are 170.03 cm long and are mounted in a vertical close-packed array. There are a total of 1140 equivalent full-size passages, counting fractional sizes. The dimensions of the flow channel were chosen to provide a passage that would not be blocked by small pieces of graphite and also to obtain a nearly optimum fuel-to-graphite ratio in the core.

The MSRE graphite has an average density of 1.86 g/cm^3, lighter than the salt density which is approximately 2.3275 g/cm^3. When not buoyed up by being immersed in the fuel salt, the vertical graphite stringers rest on a lattice of graphite blocks, with a 2.54 cm by 4.1275 cm cross section, that is laid horizontally in two layers at right angles to each other. Holes in the lattice blocks, with a diameter of 2.642 cm, accept the 2.54-cm-diameter doweled section at the lower end of each stringer. The upper horizontal surface of the vertical graphite stringers

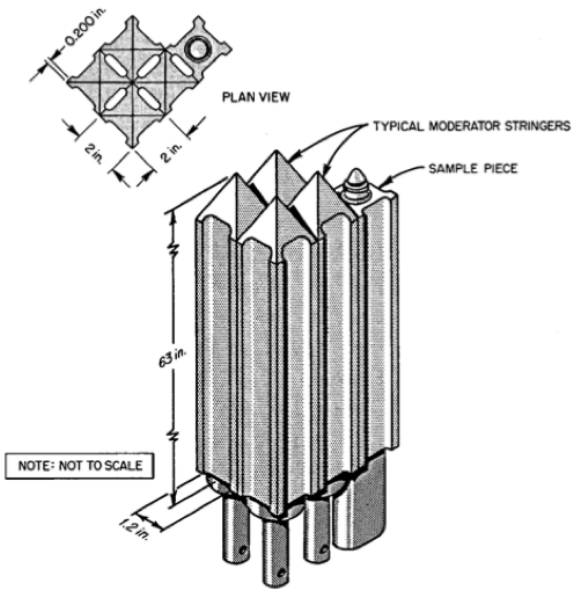

Figure 2.5: Dimensions and arrangement of the graphite stringers[21].

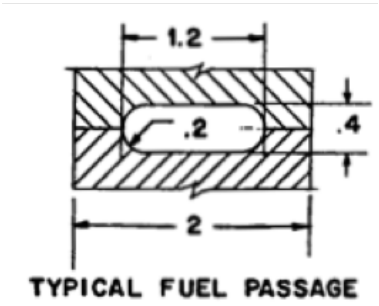

Figure 2.6: Dimensions and arrangement of the fuel channel (the unit of length is inch)[21].

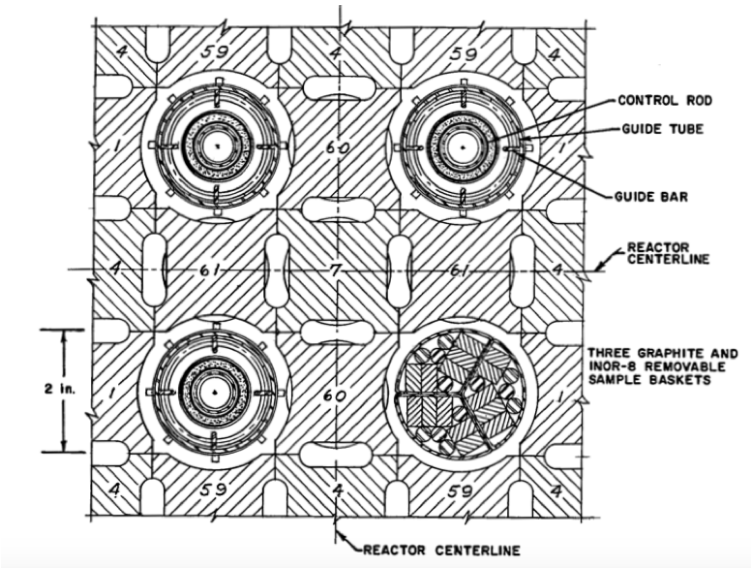

Figure 2.7: Control rod and sample baskets of the MSRE[21].

is tapered to ensure no salt remains after on it after a salt drainage as shown in Figure 2.5.

4 graphite stringers were left out to leave space for three control rod thimbles and a surveillance assembly consisting of graphite and INOR-8 sample baskets, which are arranged equidistantly near the center of the core as shown in Figure 2.7. One of the objectives of the MSRE was to investigate the behavior of the uncladded graphite moderator and INOR-8 in the reactor environment. Thus, the reactor was designed for periodic removal of graphite specimens from near the center of the core. The 5 graphite stringers enclosed by the control rods and sample baskets, labeled 7, 60, 61 in Figure 2.7, are of a special design so that they could be easily removed out of the core for examination. In the surveillance assembly, there are three identical sample baskets mounted vertically and each basket is formed of 0.079-cm-thick INOR-8 plate and has 0.238-cm-diameter holes and contains four 0.635-cm diameter and 167.64-cm long samples of INOR-8, and five graphite sample bars 0.635 cm $\times$ 1.1938 cm with a length of 167.64 cm.

The control rod thimbles have a 5.08-cm outer diameter and 0.1651-cm thick wall tubing. The control rods are segmented (see Figure 2.8 and Figure 2.9) to provide the flexibility needed to pass through the bends in the control rod thimbles (see Figure 2.10). The poison material is a mixture of 70 wt. % Gd_2O_3 and 30 wt. % Al_2O_3. Three ceramic cylinders are canned in an Inconel shell to form one control rod element. Each control rod is made of 38 elements for total length of the poison section of 150.774 cm. The segments are threaded, bead-like, on a 1.905-cm outer diameter by 1.5875-cm inner diameter helically wound, flexible stainless steel. Two 0.3175-cm diameter braided Inconel cables run through this hose to restrain it

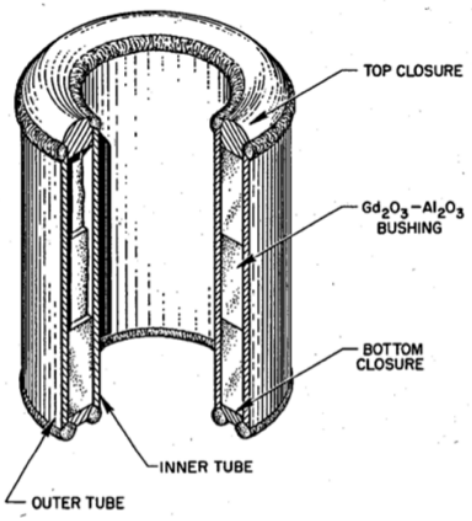

Figure 2.8: Cutaway of an MSRE control element[26].

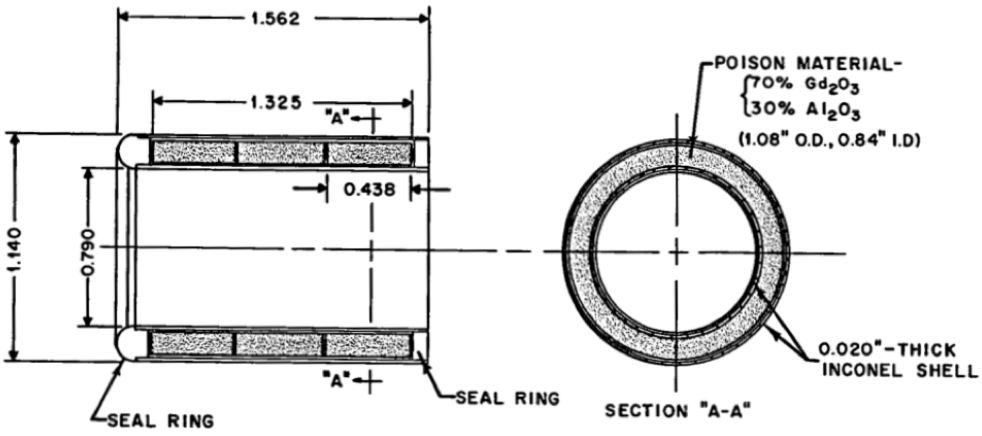

Figure 2.9: Control rod poison element geometry (the unit of length is inch)[21].

from stretching when dropped in free fall. This hose passes upward through the thimble to the positioning chain on the control-rod drive mechanism. A position indicator is provided for the lower end of the rod which permits re-calibration of the position-indicating devices related to the upper end of the rod, should there be variations in the length.

The reactor vessel is installed in a thermal shield that supports the vessel and forms the outer wall of the reactor furnace. The shield, consisting of a tank of stainless steel filled

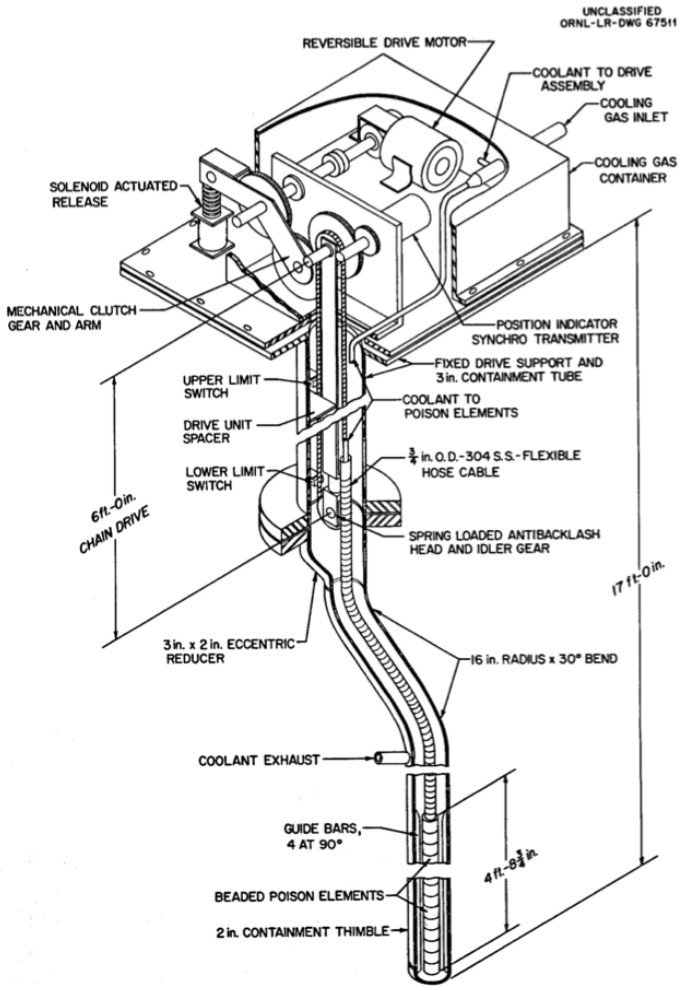

Figure 2.10: Control rod and drive[21].

with steel balls and circulating water, has an approximate outer diameter of 317.5 cm, an inner diameter of 236.22 cm and a height of 383.54 cm, as shown in Figure 2.11. Besides absorbing energy of neutrons and gamma ray escaping from the core, the shield also cuts down on neutron activation of components in the reactor cell[13]. The inside of the thermal shield is lined with 15.24 cm of high temperature insulation (vermiculite). And the reactor vessel is supported from the top removable cover of the thermal shield.

2.1.2 Initial zero-power criticality experiment

ORNL conducted a program of zero-power nuclear experiments on the MSRE in June 1965 to establish the basic nuclear characteristics of the reactor system and to provide a baseline

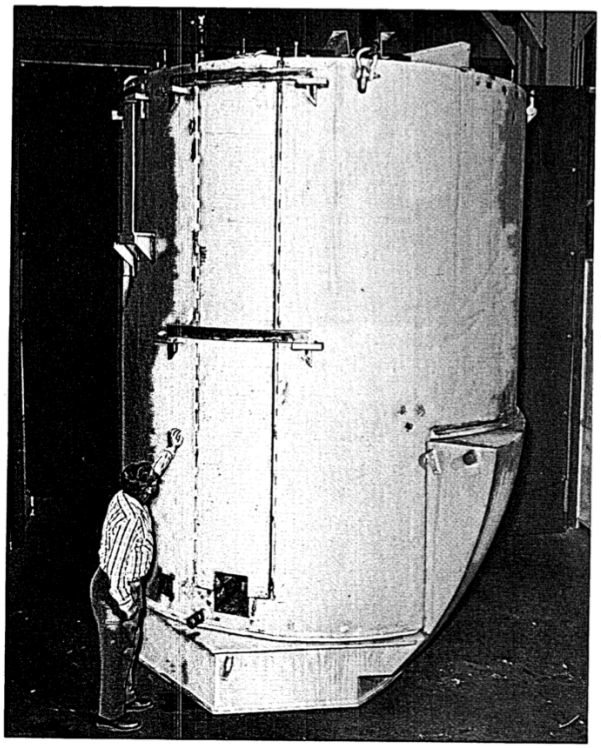

Figure 2.11: Image of the thermal shield[21].

for evaluation of the system performance during operation[19].

This program started from the first criticality experiment that established the initial critical ^{235}U loading under the simplest possible conditions, that is, with core isothermal, fuel salt stationary and control rods withdrawn to their upper limits. The first criticality experiment basically consisted in adding increments of enriched uranium concentrate to the fuel salt, LiF-BeF_2-ZrF_4-UF_4, and observing the progress toward the critical concentration by the increased neutron source multiplication. Successive additions of kilogram quantities of ^{235}U to the salt in the drain tanks, followed each time by a fill of the core and multiplication measurements, occurred until the reactor contained approximately 98% of the critical mass. The remainder was added in 85-g batches through the sampler-enricher. The sampler-enricher system can lower small capsules into the pump bowl to take samples from or add salt into the main circulating stream. Four neutron counting channels were used: two fission chambers in the instrument shaft, a BF_3 chamber in the instrument shaft, and another BF_3 chamber in the thermal shield as shown in Figure 2.12.

The salt was prepared in three lots: (1) carrier salt (65LiF-30BeF_2-5ZrF_4, salt compositions

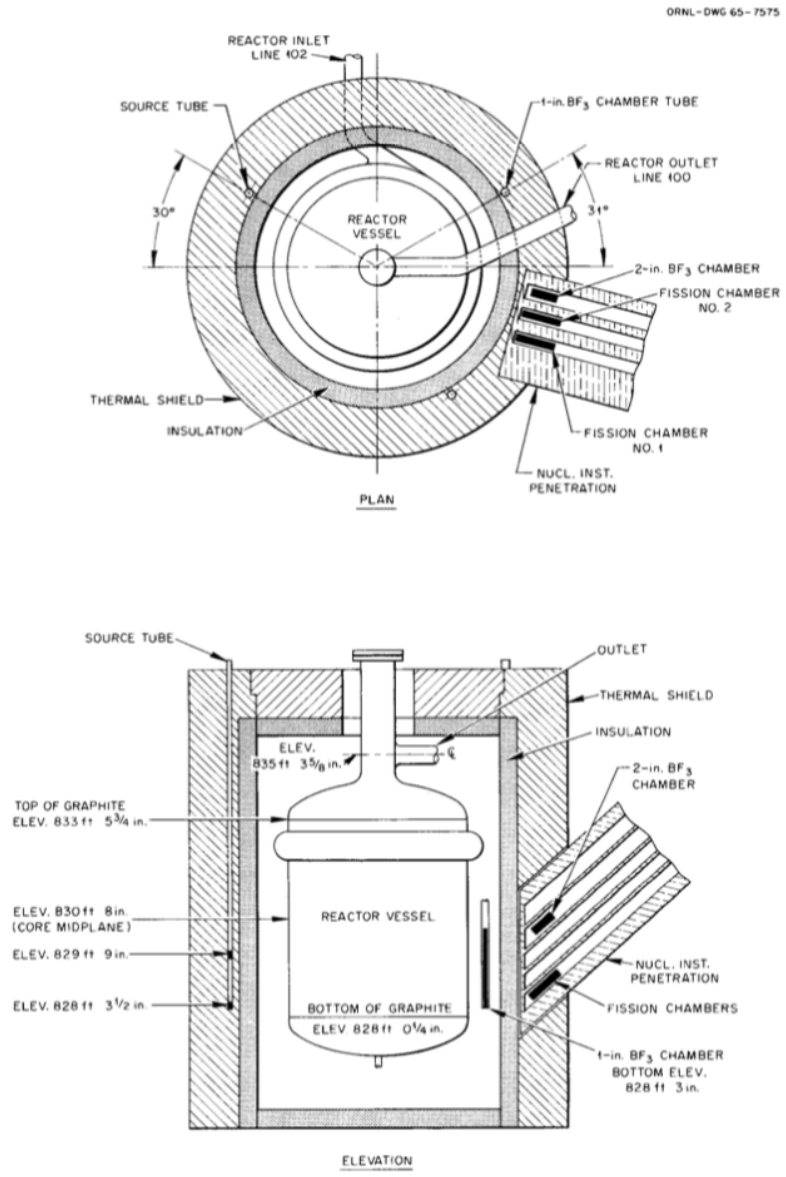

Figure 2.12: Source and instrumentation in initial criticality experiment[19].

.

are expressed in mole percent), containing the beryllium, zirconium and most of the lithium fluorides; (2) depleted uranium eutectic (73LiF-27UF_4), containing 150 kg of depleted uranium; and (3) highly-enriched eutectic, containing 90 kg of ^{235}U at 93 % ^{235}U enrichment. Thirty-five cans of carrier salt (containing 4558.1 kg of carrier salt) and two cans of depleted uranium eutectic (containing 236.2 kg of LiF-$^{238}UF_4$) were blended as they were charged into a drain tank[25]. This mixture of salt was then circulated for ten days at 649 °C while the sampler-enricher was tested, and 18 samples were analyzed to establish the initial composition. The criticality experiment then consisted in progressively increasing the enriched uranium content to bring the ^{235}U concentration up to the critical point.

On June 1, 1965, at approximately 6:00 pm, the reactor reached the critical point with fuel salt stationary[19]. Criticality was verified by leveling the power at successively higher level with the same rod position. The actual system power was about 10 W. The mass fraction of ^{235}U in the fuel salt was (1.408 ± 0.007) wt. % after considering the small amount of dilution of the fuel salt from residues of flush salt left in freeze valves and drain tank heels when the fuel salt was charged. The core temperature at the time of criticality was measured to be 638 °C instead of 649 °C as initially estimated. The fuel salt density was (2.3275 ± 0.0160) g/cm^3. One rod was inserted at 46.6 in. (the relation of rod position in the control rod thimble and elevations is shown in Figure 2.13) while the other two rods were held at 51 in., the upper limit.

2.1.3 Reactivity effects and reactivity coefficients measurements

Following the initial zero-power criticality experiment conducted on the MSRE in June, a series of control rod calibration experiments measuring reactivity effects were performed by ORNL.

The general method of increasing the uranium concentration in the fuel salt was to add 85 g ^{235}U in a capsule at a time through the sampler-enricher. The insertion of the regulating control rod (rod No. 1, the top right rod in Figure 2.7) always acts to follow and compensate for any net excess reactivity from the additions of uranium or any change of the core configuration. Figure 2.14 depicts the procedure of these control rod calibration experiments. Each curve in Figure 2.14 is a qualitative graphical description of the change in the static reactivity as a function of regulating rod position and various curves represent different ^{235}U loadings, increasing in the direction shown by the arrow. The static reactivity, ρ_s, corresponding to each specific rod position and ^{235}U loading is defined by the following equation:

$$\rho_s = \frac{\nu - \nu_c}{\nu} \tag{2.1}$$

where ν is the actual number of neutrons emitted per fission, and ν_c is the fictitious value

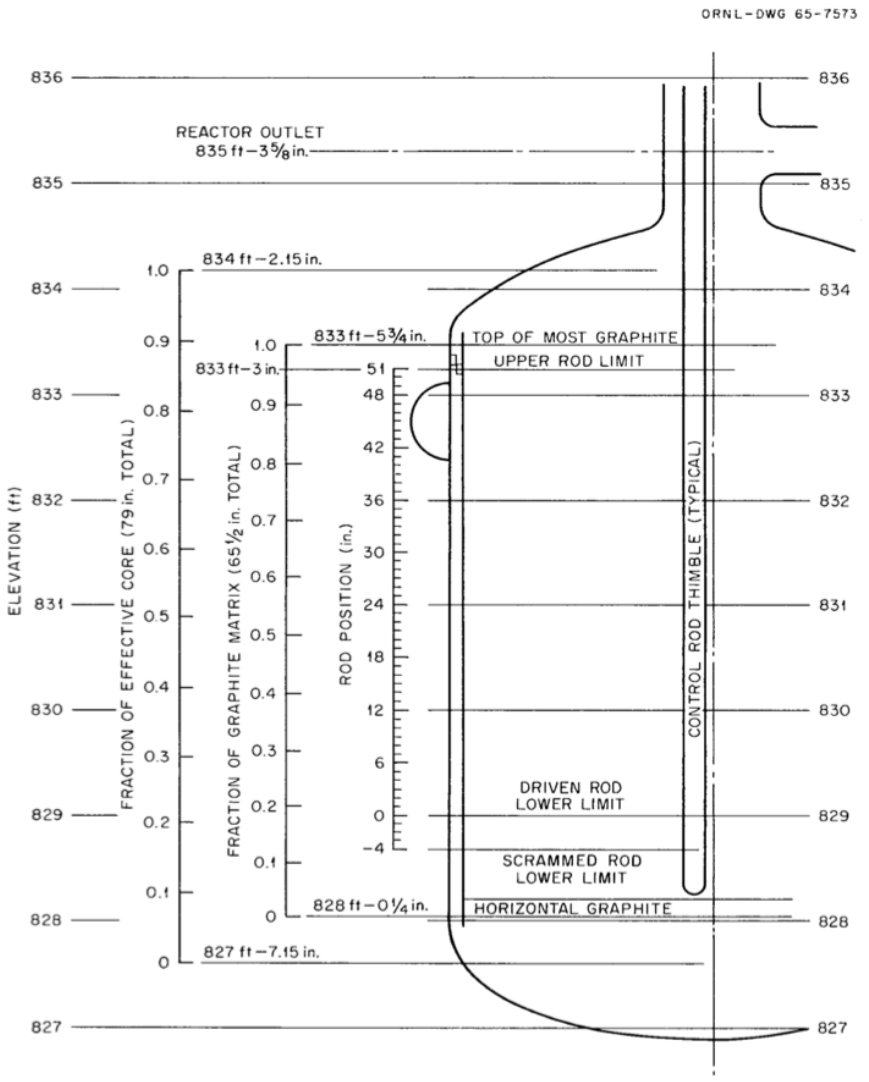

Figure 2.13: Relation of rod position and levels in reactor vessel[19].

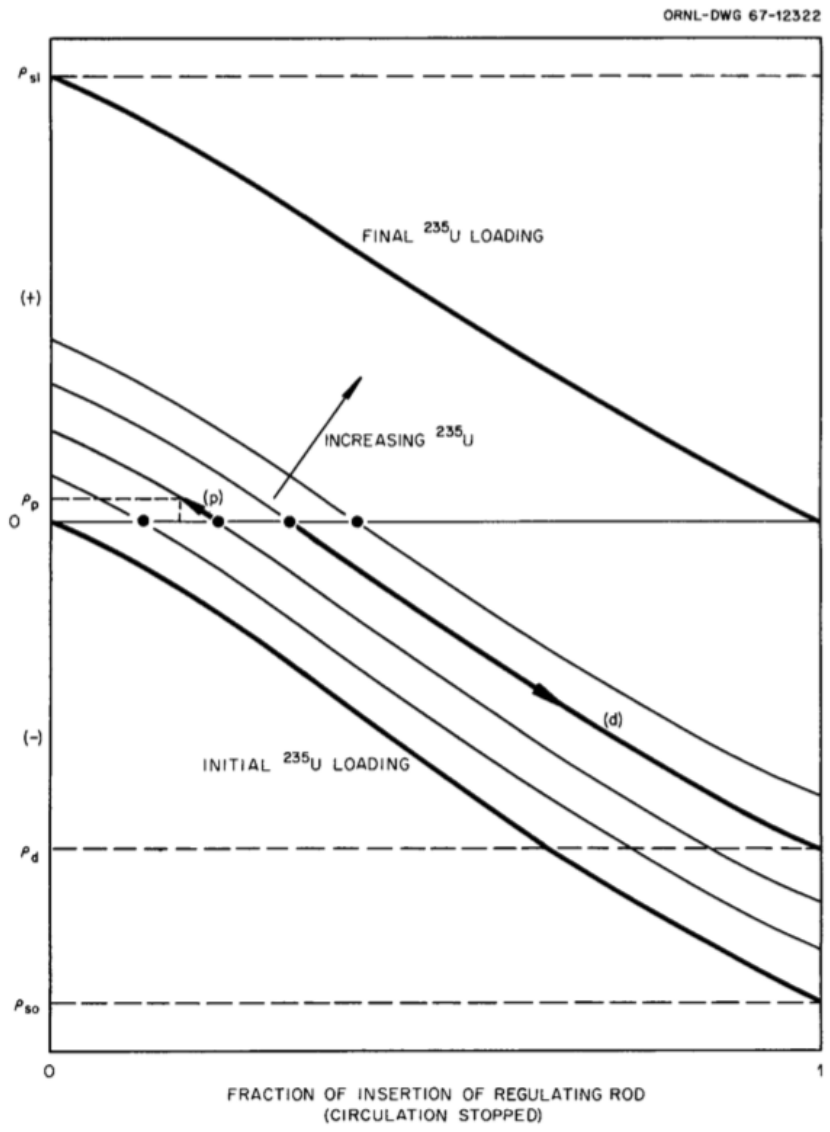

Figure 2.14: Graphical description of control rod calibration experiments[19].

for which the reactor with the specified rod position and material composition, and with the fuel stationary, would be just critical. An equivalent expression is:

$$\rho_s = \frac{k_{\text{eff}} - 1}{k_{\text{eff}}} \tag{2.2}$$

where k_{eff} is the effective multiplication constant of the reactor.

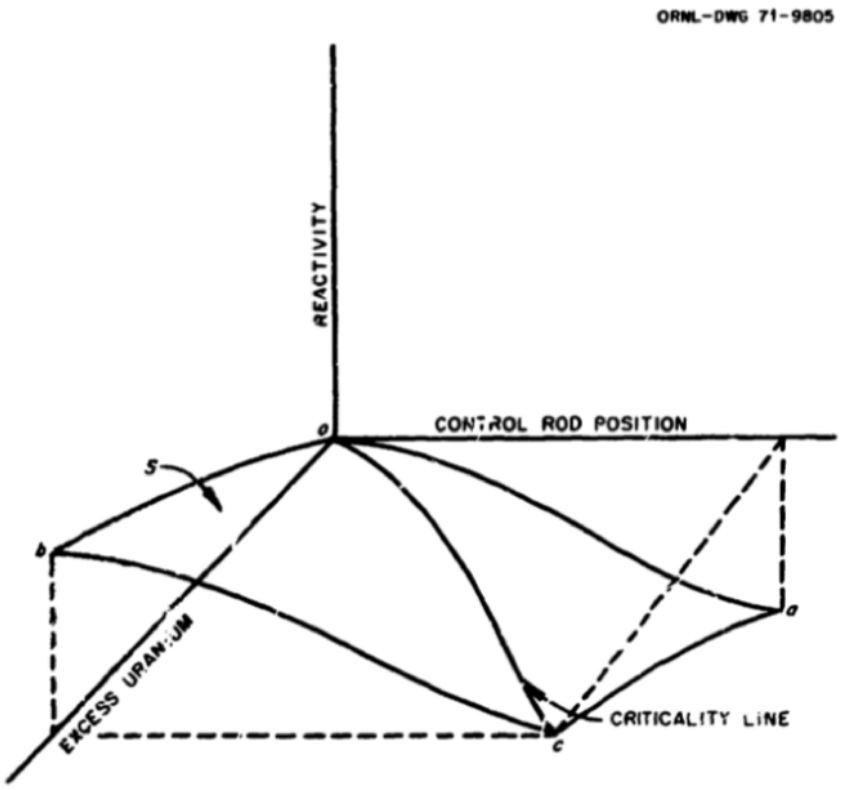

Figure 2.15: Parameter region in zero-power rod-calibration experiments[20].

There are two types of kinetic measurements occurred, the stable period measurement for the period-differential control rod worth experiment and the rod-drop experiment:

- A typical measurement of the stable period corresponds to a motion of the control rod from its critical position upward (same as moving to the left along the short segment marked (p) in Figure 2.14). The measured change in reactivity along the vertical axis, ρ_p, is divided by the increment in rod motion, and this differential worth is ascribed to the mean position;
- A typical rod-drop experiment is indicated in Figure 2.14 by the segment marked (d), extending from the initial critical control rod position into the subcritical region. The purpose of this experiment is to measure the negative reactivity inserted by the drop, marked ρ_d.

Figure 2.15 depicts the parameter region of the rod calibration experiments in the MSRE. The solid curve *oc* lying in the horizontal plane (reactivity = 0) is the only relation directly accessible from experiments[20]. To obtain knowledge of the complete surface S, it is necessary to "reach" into the vertical dimension, either by performing kinetic experiments or by performing theoretical calculations.

According to [20], the static reactivity concept, which often used to describe the off-critical state, can be relate to the reactivity inferred from kinetic measurements if the model used is sufficiently realistic and can give an exact description of the critical state. For the period-differential worth and rod-drop integral-worth experiments in the MSRE, the differences in the static reactivity, defined by Eq 2.1, and the reactivity inferred from kinetic measurements are operationally insignificant. The use of correction factors, wherever necessary to keep consistency in the uranium concentration, and the design of measurement procedures that avoids instances where important differences between the two kinds of reactivity can occur achieve the goal. Therefore, the static reactivity concept and scale was regarded as a basis for an integrated and unified interpretation of the measured reactivity for the MSRE.

The detailed descriptions of MSRE control rod calibration experiments can be found in [19] or in the official MSRE benchmark for the IRPhEP handbook. A brief overview is provided here.

First of all, the differential reactivity worth of control rod No. 1 as a function of position was measured, both with the fuel salt stationary and with it circulating. At the same time, the critical control rod configurations as a function of uranium concentration were obtained and the reactivity equivalent of ^{235}U additions can be determined from the previous rod worth measurement. As shown in Figure 2.14 and Figure 2.15, only the reactivity equivalent of the ^{235}U addition was compensated by insertion of control rod. Therefore, calibration of the rod by independent experiments can provide an empirical determination of the reactivity worth of the additional ^{235}U. Following that, the effect of fuel salt circulation on reactivity and control rod shadowing effects were measured. The control rod shadowing effects refer to the change in the critical position of the regulating rod (rod No. 1) as the shim rods (rods No. 2 and No. 3) were inserted into the core. Rod-drop experiments were performed to provide an independent verification of the integral worth of various control rod configurations. Sufficient excess uranium was added during this program to permit calibration of one control rod over its entire length of travel. The final amount of ^{235}U was to be enough to be critical at 649 °C with the fuel stationary and one rod fully inserted.

The isothermal temperature coefficient and fuel temperature coefficient were measured basing on the results of control rod calibration experiments. At three fixed ^{235}U concentrations, the reactor system temperature was varied slowly (about 15 °F/h) by adjusting electric heaters while the critical position of the regulating rod was observed. The change in critical position of the regulating rod was converted to reactivity by use of the rod calibration results. This

experiment gave the overall temperature coefficient, that is, the sum of fuel and graphite coefficients.

An attempt was made to separate the fuel (rapid) and graphite (sluggish) temperature coefficients by an experiment in which the fuel was kept in circulation and the coolant loop was stagnant. After heating the stagnant coolant salt about 20 °F hotter than the fuel salt, the coolant pump was started, introducing a hot slug of fuel into the heat exchanger and subsequently into the core. In this test, then, the change in reactivity was due entirely to the change in fuel temperature.

As the essential basis for all the following experiments, the stable period measurements for rod differential worth is further illustrated here.

At certain ^{235}U concentration level, the control rod No. 1 was first adjusted to make the reactor critical at about 10 W and then it was pulled a prescribed distance and held there until the power had increased by about two decades. Two fission chambers driving log-count-rate meters and a two-pen recorder were used to measure the period (generally in the range of 30 sec to 150 sec). For the measurements with the pump off, the standard inhour relation was used to calculate the reactivity increment corresponding to ω, the observed stable inverse period, as below:

$$\rho = \omega\Lambda + \sum_{i=1}^{6} \frac{\beta_i \omega}{\omega + \lambda_i} \tag{2.3}$$

The decay constants, λ_i, and the effective delay fractions, β_i, used in these calculations, are listed in Table 2.4. The neutron generation time, Λ, was 2.6×10^{-4} sec for the initial critical loading, obtained from theoretical analysis[19].

Table 2.4: Delayed neutron fractions used for reactivity inference in MSRE differential rod worth measurements, all values from [19]

Group	Decay constant, sec^{-1}	Actual delay fraction$\times 10^4$	Effective delay fraction[a]$\times 10^4$
1	0.0124	2.11	2.23
2	0.0305	14.02	14.57
3	0.1114	12.54	13.07
4	0.3013	25.28	26.28
5	1.140	7.40	7.66
6	3.010	2.70	2.80

[a] With fuel stationary.

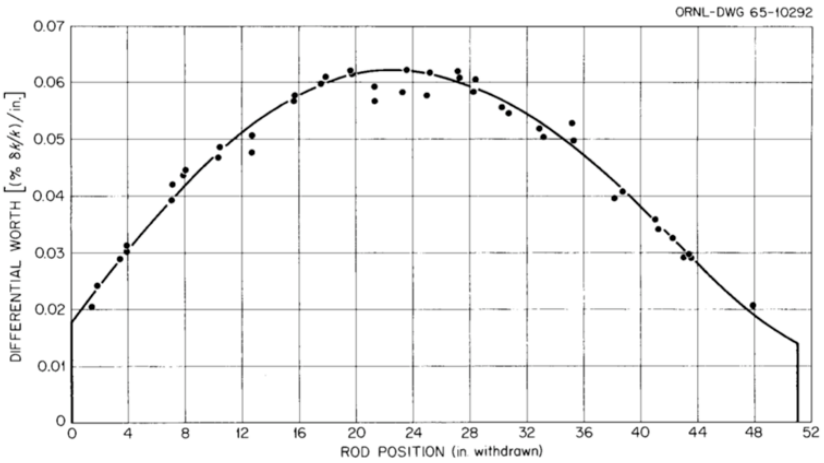

Figure 2.16: Differential worth of control rod No. 1, measured with fuel stationary and normalized to initial critical ^{235}U loading[19].

The differential-worth measurements made with the fuel pump off are plotted in Figure 2.16. Theoretical corrections have been applied to these measurements to put them all on the basis of one ^{235}U concentration, arbitrarily chosen as the initial critical concentration that is 65.25 kg ^{235}U in loop. The approximate correction factors which were applied to the rod sensitivity measurements increase linearly with ^{235}U concentration, up to 1.087 for the measurements made near the final concentration that is 71.71 kg ^{235}U in loop. As stated before, it is useful for purposes of consistency to interpret the combined reactivity measurements, over the whole range of rod movement, on the basis of a single mass of ^{235}U. Theoretical calculations of the rod worth by ORNL were used to determine the effects of the ^{235}U concentration on the rod worth.

Serving as an independent check for the integral worth of various control rod configurations, the rod-drop experiment is further illustrated here.

After 30, 65 and 87 capsules of enriched uranium additions, rod-drop effects were observed, which consists of the intentional scram of a rod, or rod group, from an initially critical configuration and the recording of the decay of the neutron flux as a function of time following the scram. The flux decay trajectory is characterized by a sharp drop immediately following the scram, corresponding closely with the actual fall of the rod. After that, the curve rapidly and continuously evolves into one with a much slower rate of flux decrease, governed by the decay of the initial distribution of delayed neutron precursors (DNPs). The integral neutron count, rather than log n, as a function of time following the rod drop was recorded to serve the requirements of fast response, good counting statistics, and reproducibility. The results of the rod-drop experiments made after additions of 30 and 65 capsules of enriching salt are

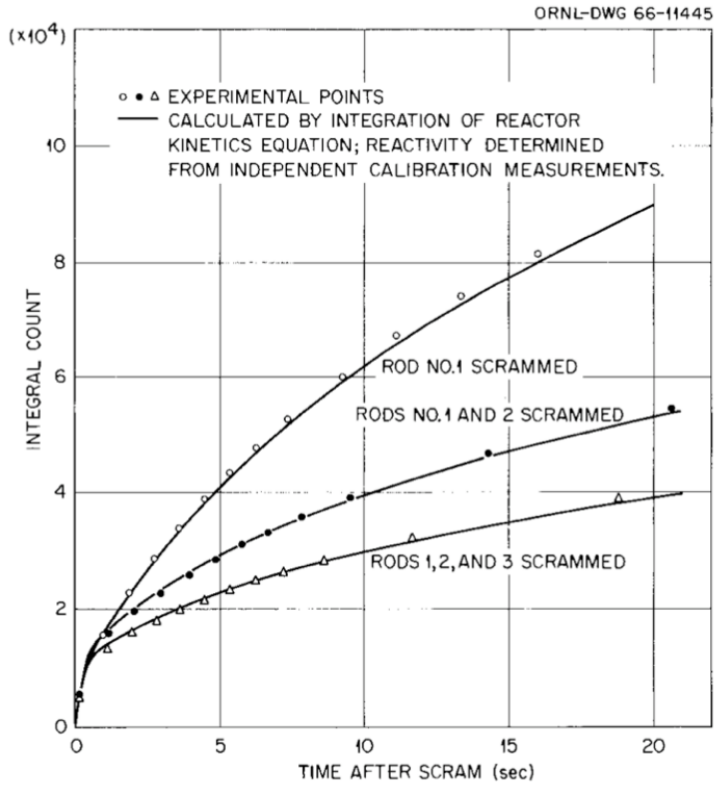

Figure 2.17: Results of rod-drop experiments after 30 capsule additions[19].

shown in Figure 2.17 and Figure 2.18.

2.2 Modeling of the criticality experiment

2.2.1 Serpent2 model

A benchmark model of the MSRE first criticality experiment was prepared and analyzed by Serpent2 with as much detail as feasible. In this benchmark model, the dimensions for the graphite lattice, control rod thimbles, sample baskets, reactor vessel shell, flow distributor and thermal shield are those obtained from design data and/or blueprints while the fuel inlet pipe, fuel outlet pipe, fuel outlet strainer, reactor access port (Figure 2.3), the external loop outside the thermal shield and the base for the thermal shield are neglected. The bias from neglecting these components in the benchmark was evaluated by creating a fully-detailed model (see Figure 2.19) which contains the fuel inlet pipe, fuel outlet pipe, fuel outlet strainer, reactor access port and thermal shield base and the biases on k_{eff} was calculated to be (-22 ± 5) pcm.

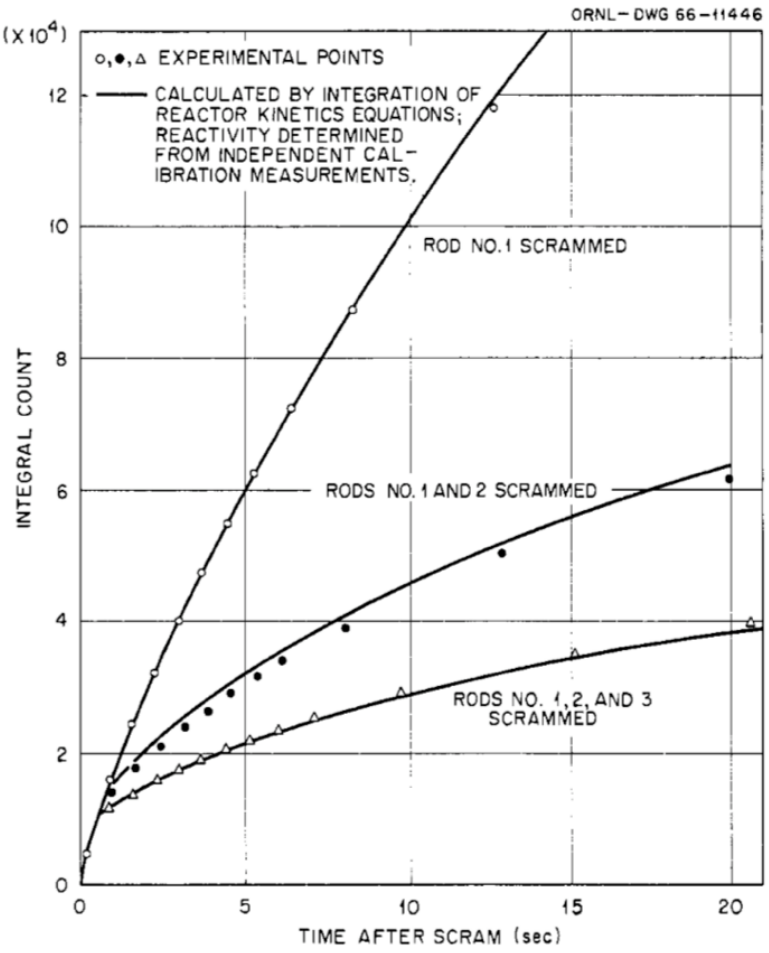

Figure 2.18: Results of rod-drop experiments after 65 capsule additions[19].

There are other simplifications in the MSRE benchmark model which are believed to have no significant effect on k_{eff}. The lower head of the reactor vessel is simplified as a homogeneous mixture of fuel salt and INOR-8 with a volume ratio of 90.8:9.2 according to [12]. The upper head of the reactor vessel is simplified to a pure salt region. The insulation layer and thermal shield are also simplified as homogeneous mixture.

All the dimensions are "hot" dimensions (at 638 °C) in the benchmark model. Since all the dimensions provided in the reference were at room temperature, the thermal expansion of graphite and metal components was performed in the reactor vessel from 20 °C (the room temperature) to 638 °C (the operating temperature) of the experiment. According to [21], the thermal expansion coefficient for graphite lattice is 1.5×10^{-6}/°F and is 7.8×10^{-6}/°F for metal components. To simulate the thermal expansion, the reactor vessel was freely

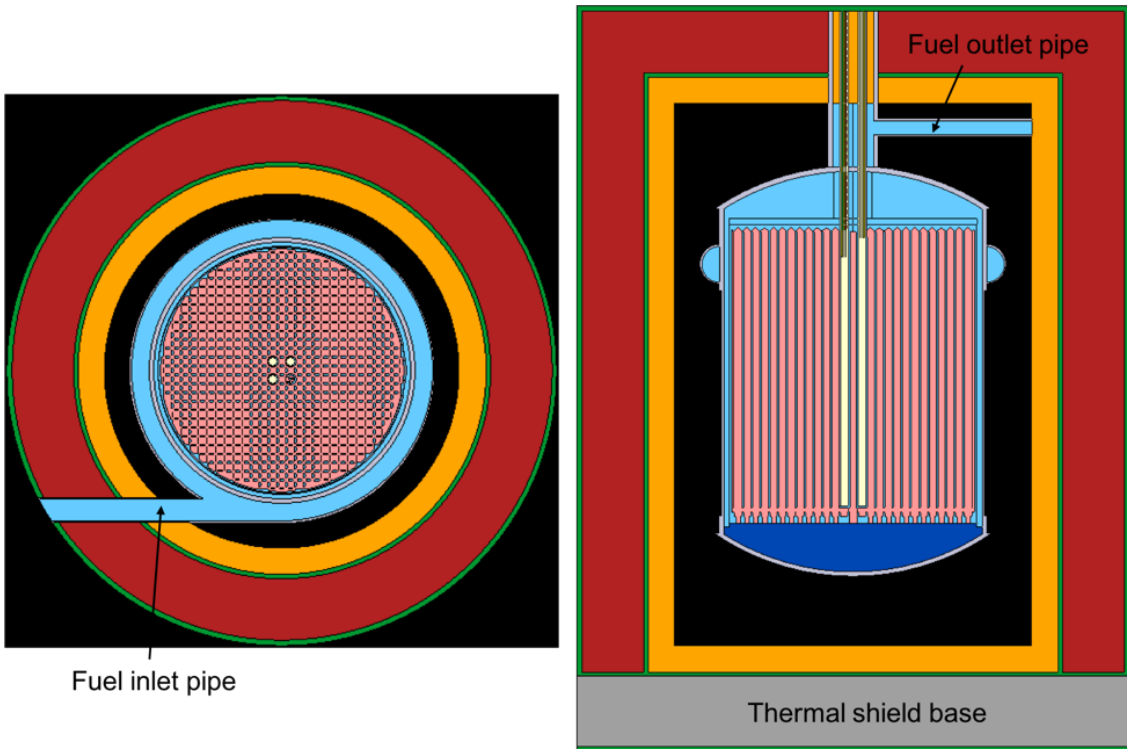

Figure 2.19: Horizontal cross section at $z = 145.396$ cm (left) and vertical cross section of the core offset by 5.08339 cm from the center (right) of the full detailed MSRE model.

expanded downward from the interface between the outlet pipe and the upper insulation layer, as shown in Figure 2.12. The horizontal graphite lattice was connected with the vessel at its bottom, labeled as $z = 0$ plane in the model, and the vertical graphite stringers were held by the horizontal graphite lattice; therefore, in the benchmark model considering thermal expansion, the horizontal graphite lattice was first moved together with the vessel to a new $z = 0$ plane and then thermally expanded upward from the $z = 0$ plane. Finally, the thermally expanded vertical graphite stringers were put upon the horizontal graphite lattice.

Table 2.5: Comparisons of "cold" and "hot" dimensions of the MSRE

Dimension	At 20 °C	At 638 °C
Graphite lattice radius, cm	70.168	70.285
Core can inner radius, cm	70.485	71.097
Core can outer radius, cm	71.120	71.737
Reactor vessel inner radius, cm	73.660	74.299
Reactor vessel outer radius, cm	76.200	76.862
Graphite stringer width, cm	5.075	5.084
Fuel channel width, cm	1.016	1.018
Fuel channel length, cm	3.048	3.053
Graphite stringer height, cm	170.027	170.311
Total height of the vessel, cm	269.771	272.113
Length of the control rod inserted, cm	76.414	77.077

Figure 2.20 and Figure 2.21 provide an overview of the benchmark models, including axial location respect to the bottom of the horizontal graphite lattice and radial dimensions. The arrangement of the graphite stringers is disrupted in the center by three control rods and the sample baskets as shown in Figure 2.22. The control rods and sample baskets are housed in a cylindrical channel of 3.1992 cm radius. The space in between the graphite and the control rod thimbles and basket is filled with salt.

As the most important component in the core geometry, the vertical graphite lattice is formed by vertical graphite stringers whose cross section is a square with side length of 5.08339 cm; 1.01770 cm by 3.05309 cm fuel channels with round corners (radius is 0.50885 cm) are machined at the center the four sides of the stringers as shown in Figure 2.23. At the boundary of the lattice some stringers are cut and some channels are partially closed, as shown in Figure 2.24, according to MSRE drawings and blueprints.

At the top of the graphite stringers, a centering bridge (as shown in Figure 2.3 and Figure 2.4) holds two rows of stringers at right angles to each other and these two rows of stringers are higher than regular ones. This centering bridge that helps to prevent shifting of the entire stringer assembly was modeled in detail as shown in Figure 2.25.

Detail dimensions of each component of the core are provided in the official MSRE benchmark specification which will be released with the 2019 IRPhEP handbook.

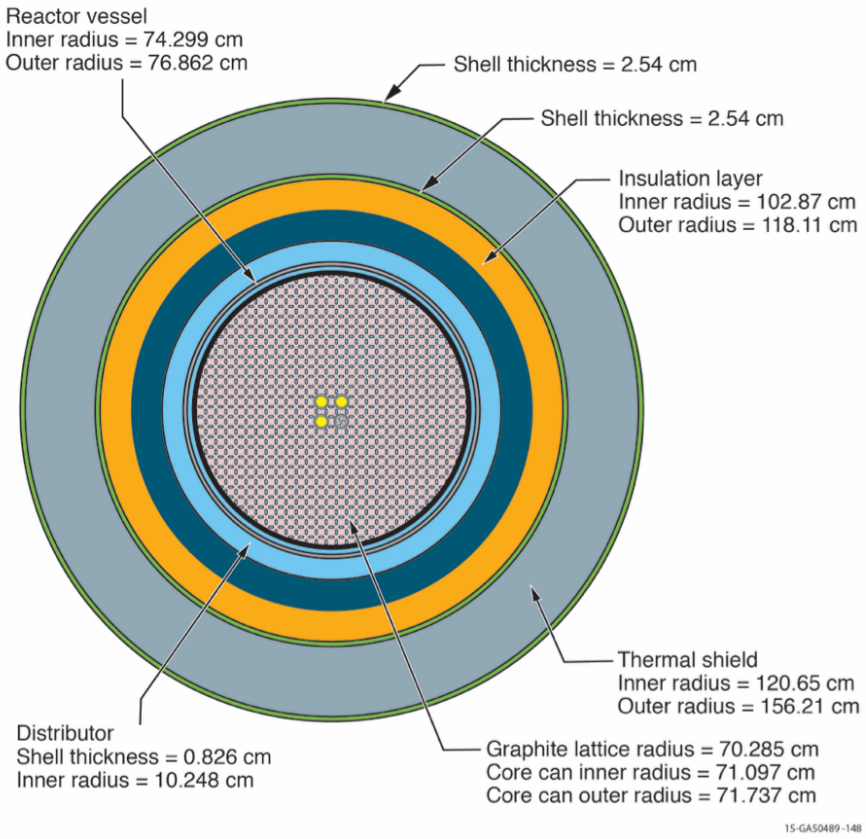

Figure 2.20: Horizontal cross section of the MSRE model at 638 °C. The cross section is located at the centerline of the flow distributor (z = 145.396 cm in Figure 2.21). Credit: David R. Sharp, Idaho National Laboratory.

2.2.2 Materials

As stated before, the MSRE fuel salt was comprised of three parts: (1) the carrier salt, containing the beryllium, zirconium and most of the lithium fluorides; (2) depleted uranium eutectic (73LiF-27UF_4), with the following uranium composition 0.00% ^{234}U, 0.22% ^{235}U, 0.00% ^{236}U, 99.78% ^{238}U; and (3) highly-enriched uranium eutectic (73LiF-27UF_4), with the following uranium composition 0.95% ^{234}U, 92.95% ^{235}U, 0.39% ^{236}U, 5.70% ^{238}U. [25] provides the chemical composition of the MSRE fuel salt after calibration according to comparisons between the nominal salt isotopic composition and the results of mass spectrometric analyses, as shown in Table 2.6. According to [25], only 89.07% of the fuel salt was transferred into the primary loop (this part was referred to as the loop charge) and the rest of the salt remained in the drain tank.

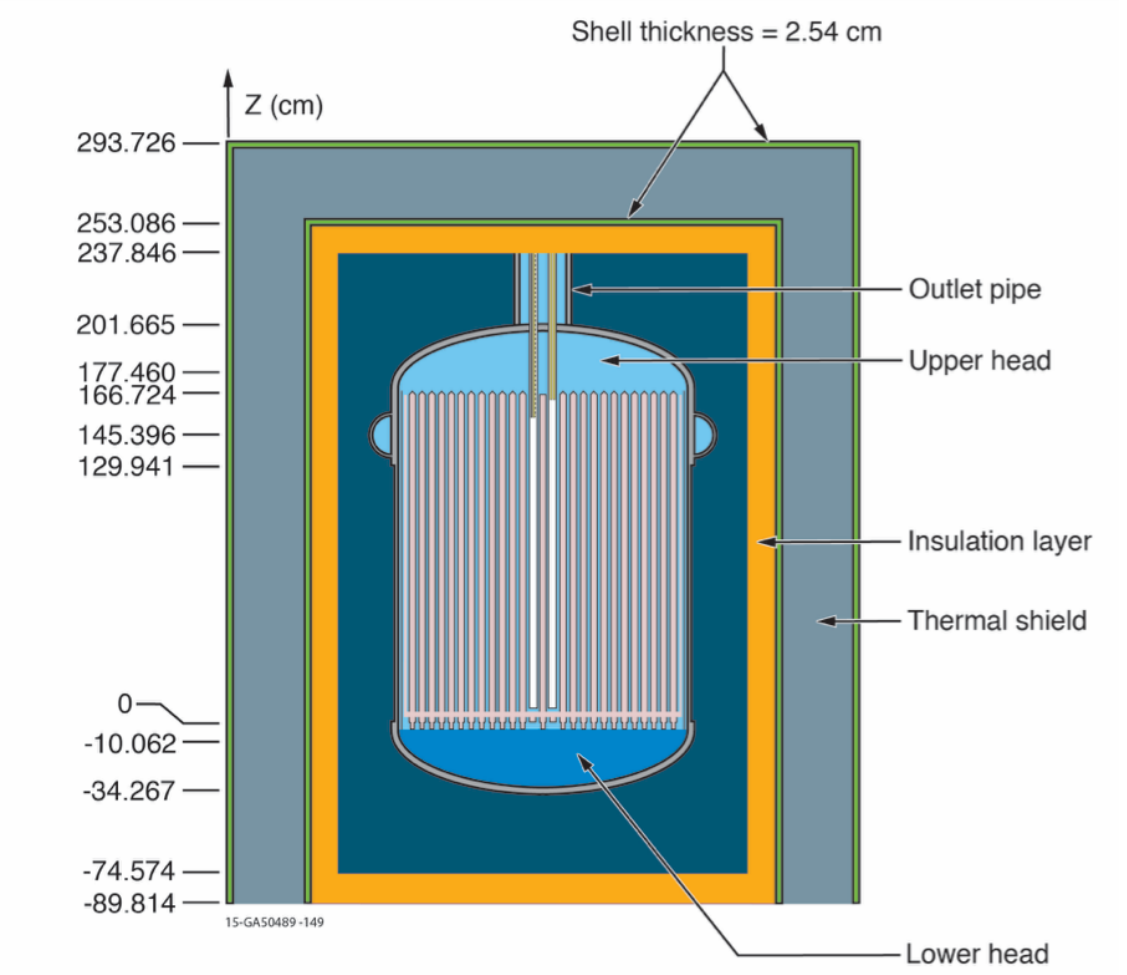

Figure 2.21: Vertical cross section of the MSRE model at 638 °C. The cross section is offset by 5.08339 cm from the center of the graphite stinger lattice in order to show control rods. Location $z = 0$ corresponds to the bottom of the horizontal graphite lattice. Credit: David R. Sharp, Idaho National Laboratory.

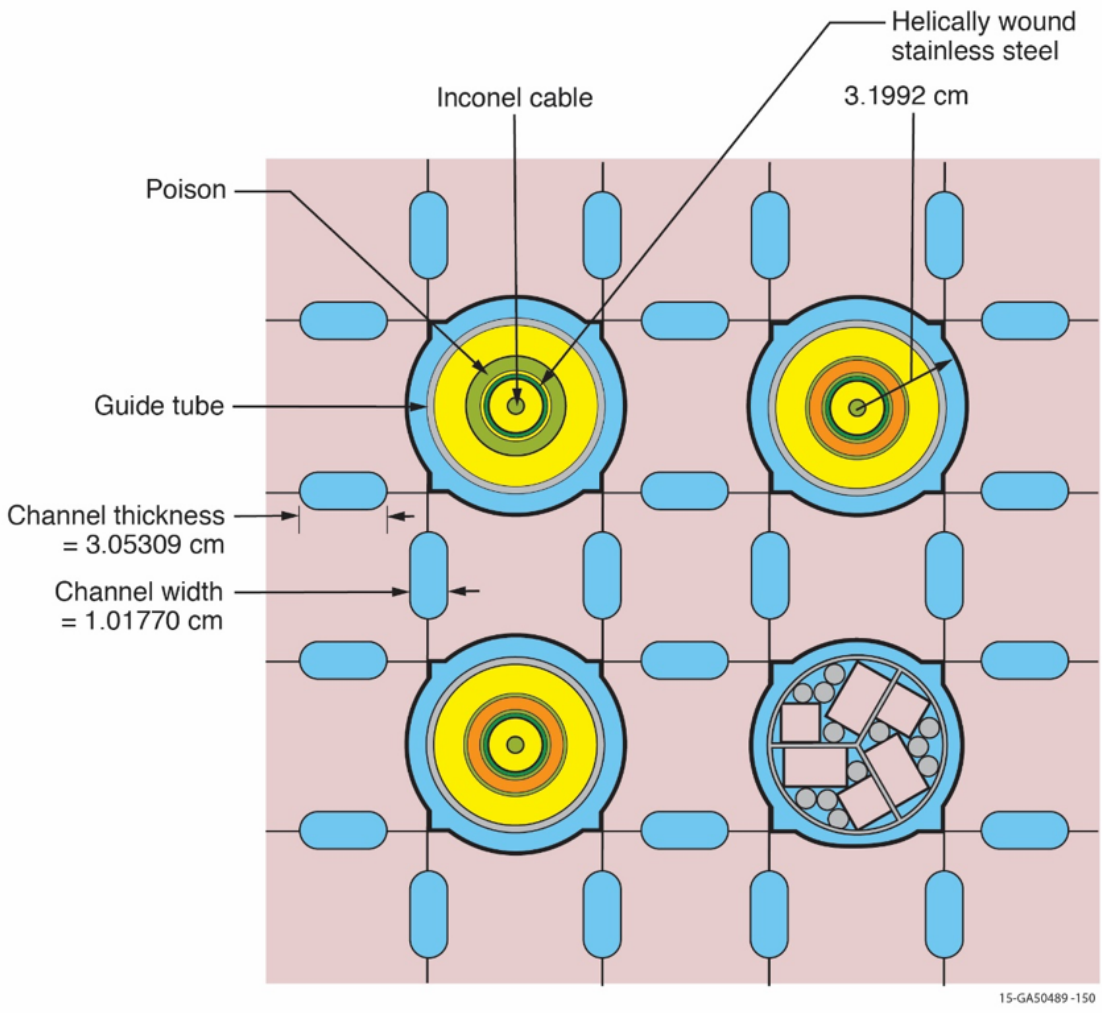

Figure 2.22: Horizontal cross section of control rods and the sample basket at 638 °C. Credit: David R. Sharp, Idaho National Laboratory.

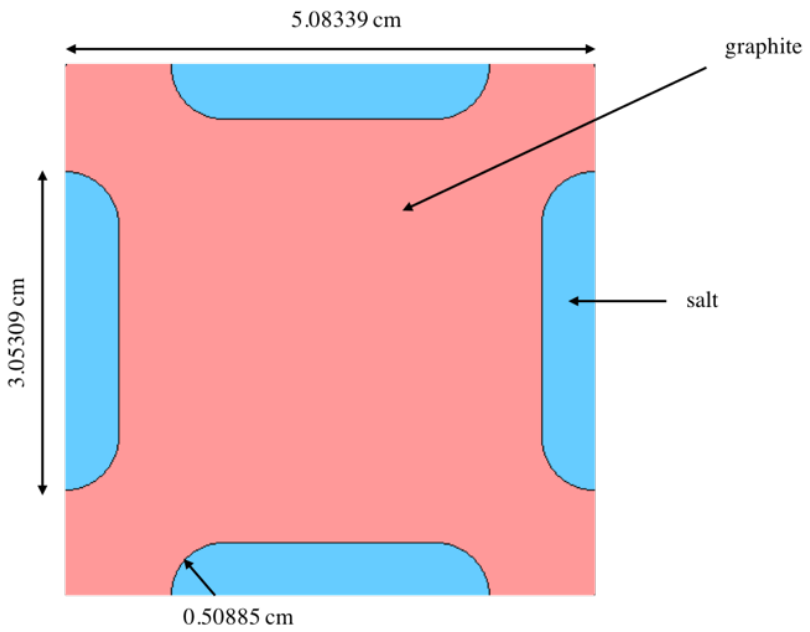

Figure 2.23: Horizontal cross section of single graphite stringer.

Table 2.6: Chemical composition of the MSRE fuel salt, all values from [25]

Salt type	Li	Be	Zr	U	Sum
Carrier salt, kg	519.16	309.62	541.36	0	4520.0
Depleted uranium eutectic, kg	11.55	0	0	145.60	234.5
Highly-enriched uranium eutectic, kg	5.84	0	0	73.59	118.55
Total fuel salt, kg	534.30	309.62	541.36	219.19	4873.05
Loop charge (89.07%), kg	475.90	275.78	482.19	195.23	4340.43

The fuel salt composition at the time of criticality was calculated as 64.88LiF-29.27BeF_2-5.06ZrF_4-0.79UF_4 (expressed as mole percent) from Table 2.6. [25] provides the isotopic composition of uranium in the MSRE fuel salt during initial loading operation, as shown in Table 2.7. ^{7}Li enrichment was 99.995%. The tolerance range for ^{6}Li enrichment in the salt was between 0.004% and 0.006%.

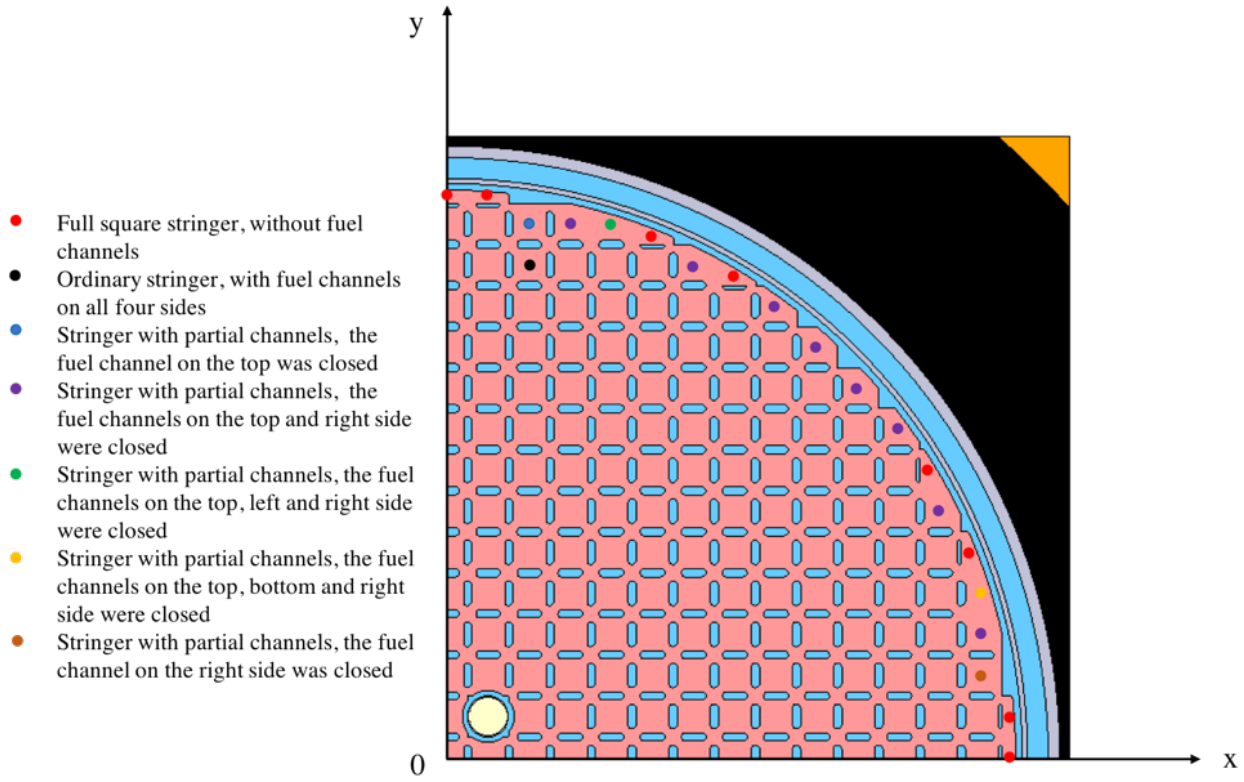

Figure 2.24: Horizontal cross section of 1/4 of the graphite lattice region at $z = 50\,\text{cm}$. The size of the stringers at the edge is determined by a cylinder with center corresponding to the center of the core and a radius of 70.285 cm.

Table 2.7: Isotopic composition of uranium in the MSRE fuel salt during initial loading operation, all values from [25]

Event	Total U, kg	^{234}U, kg	^{235}U, kg	^{236}U, kg	^{238}U, kg
Loading of depleted uranium eutectic	145.600	0.000	0.323	0.000	145.277
Additions of highly-enriched eutectic on May 25, 1965	47.490	0.452	44.143	0.187	2.708
Additions of highly-enriched eutectic on May 30, 1965	26.100	0.249	24.261	0.102	1.488
Total in the detail tank (before charge)	219.190	0.701	68.727	0.289	149.473
Loop charge (89.07%)	195.233	0.624	61.215	0.257	133.136

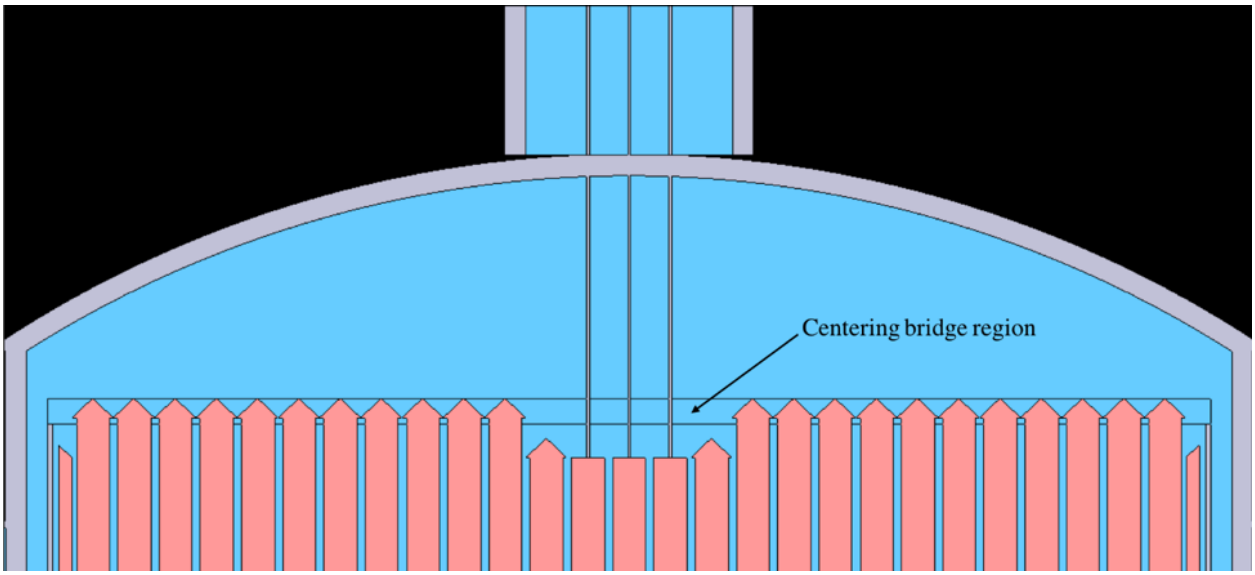

Figure 2.25: Vertical cross section of the MSRE core at $y = 0$, zooming in the centering bridge region.

According to [19], at the time of criticality the density of fuel salt was (2.3275 ± 0.0160) g/cm^3 and the mass fraction of ^{235}U in the salt was (1.408 ± 0.007) wt. %. The calculated mass fraction of ^{235}U in the salt from the above salt compositions is 1.409 wt. % (as shown in Table 2.8) and it agrees well with the tolerance range provided in [19].

Table 2.8: Mass fraction of uranium isotopes in the MSRE fuel salt at the time of criticality

Isotope	^{235}U	^{234}U	^{236}U	^{238}U
Mass fraction in total salt, wt. %	1.409	0.014	0.006	3.065

The concentration of impurities of fuel salt is provided in Table 2.9. According to [16], the primary corrosion mechanism in the MSRE fuel salt system was selective removal of chromium by:

$$2\,UF_4 + Cr(\text{in alloy}) \rightleftharpoons 2\,UF_3 + CrF_2(\text{in salt})$$

and the concentration of chromium in salt serves as the primary indicator of corrosion.

Table 2.9: Concentration of impurities in the MSRE fuel salt, all values from [25]

Element	Concentration, ppm
Fe	162
Cr	28
Ni	30
O	490

The zirconium tetra-fluoride used for the MSRE fuel salt was essentially hafnium free ($<$ 50 ppm Hf). In addition to the impurities provided in Table 2.9, it was postulated that undissolved helium could be present if entrained in the circulating fuel through the action of the fission product gas stripping device. Nevertheless, a gamma-ray densitometer positioned on the reactor inlet line detected no measurable helium void. The sensitivity of the void measurement was 0.076 vol%[6]. The expansion coefficient of the fuel salt is $-1.18\times10^{-4}/°\mathrm{F}$.

The salt-containing piping and equipment are made of INOR-8, a special high-nickel and molybdenum alloy having a good resistance to attack by fuel and coolant salts at temperatures at least as high as 816 °C. The density of INOR-8 is $8.7745\,\mathrm{g/cm^3}$ with the nominal composition of 68%Ni-17%Mo-7%Cr-5%Fe.

The graphite for the MSRE is a special grade, given the designation "CGB" by the National Carbon Company. The designed properties of the MSRE graphite are listed in Table 2.10. [5] evaluated the as-built MSRE graphite and found that the bulk density ranged from 1.83 to 1.87 $\mathrm{g/cm^3}$, with an average value of $1.86\,\mathrm{g/cm^3}$. The CGB graphite is a new material of high density and small pore size at the time of the MSRE experiments. The fuel salt does not wet the graphite and therefore should not enter the pores, even at pressure well above the operating pressure. Extremely small quantities of salt may penetrate the graphite either through pores or cracks and there is $<$ 2 g of uranium in the 3,700 kg of graphite in the entire core after 2.5 years exposure in the MSRE fuel salt[13]. The MSRE graphite was expected to release the oxygen in the form of water vapor during the planned pretreatment[5]: the graphite was carefully heated in dry helium to desorb water vapor after installation in the reactor and a purge salt was thoroughly circulated through the primary system to remove all but trace amounts of oxygen before any fuel salt was introduced. The graphite core lattice is sufficiently unrestrained and the coefficient of thermal expansion is provided in Table 2.11.

Table 2.10: Properties of MSRE core graphite - CGB, all values from [21]

Property	Value
Bulk density, g/cm^3	1.83 - 1.89
Salt absorption at 150 psig, vol. %	0.20
Ash, wt. %	0.0005
Boron, wt. %	0.00008
Vanadium, wt. %	0.0009
Sulfur, wt. %	0.0005
Oxygen, cm^3 of CO(STP) per 100 cm^3 of graphite	6.0

Table 2.11: Thermal expansion coefficient of the graphite and INOR-8 in the 70 °F - 1200 °F range, all values from [21]

Material	Coefficient of thermal expansion, 1/°F
Graphite	$1.3 - 1.7 \times 10^{-6}$
INOR-8	7.8×10^{-6}

2.3 Modeling of reactivity effect experiments

The geometry arrangements of the benchmark model for determination of the reactivity effects measurements are identical to those of the first zero-power critical core configuration described above with the exception of the control rod position and temperature. The reactivity effect experiment was operated at 649 °C, rather than 638 °C (the temperature for the criticality experiment). Therefore, the dimensions of the reactivity benchmark model differ from the criticality benchmark model but simplifications applied to both models remain the same. Novel methods were developed to model required characteristics and experimental parameters in the MSRE model as follows.

2.3.1 Control rod worth

The three control thimbles are centered at (5.08339 cm, 5.08339 cm), (-5.08339 cm, 5.08339 cm) and (-5.08339 cm, -5.08339 cm) as shown in Figure 2.26, regarding the center of the graphite lattice as the origin. Each control rod element is modeled as a cylinder with a flat surface at the top and bottom closures (see Figure 2.27). Control rod elements are packed vertically inside each control rod thimble.

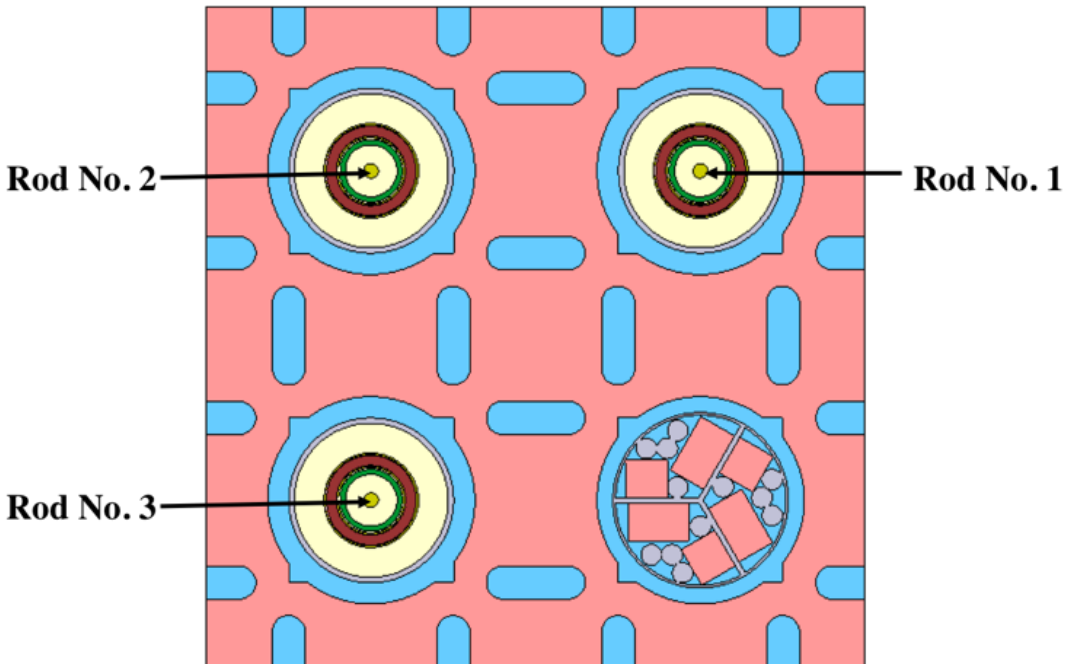

Figure 2.26: Horizontal cross section of three control rods, rod No. 1 is the regulating rod and rod No. 2 and 3 are the shim rods.

To calculate the differential and integral control rod worth, rod No. 1 (the upper right one shown in Figure 2.26) was moved $\pm\Delta x$ cm from specified configurations to obtain the difference of reactivity from the difference of rod positions. Control rod No. 2 and No. 3 are withdrawn to the upper limit at this moment and the differential worth of rod No. 1 at position x was calculated applying the following equation:

$$f(x) = \frac{\rho(x + \Delta x) - \rho(x - \Delta x)}{2\Delta x} \tag{2.4}$$

Due to the complex shape of the control rod elements and the way they were threaded in the stainless steel tube, it would be time-consuming to write new Serpent2 input every time with a change of parameter related to control rods. A Python script was developed to automatically generate the Serpent2 input with user-specified rod-related parameters such as rod position and temperature. Also, given a predefined bottom position of the poison part and Δx, the step of vertically moving distance, the Serpent2 inputs with control rod No. 1 moving from the top to the bottom of the control rod thimble can be generated, as shown in Figure 2.28.

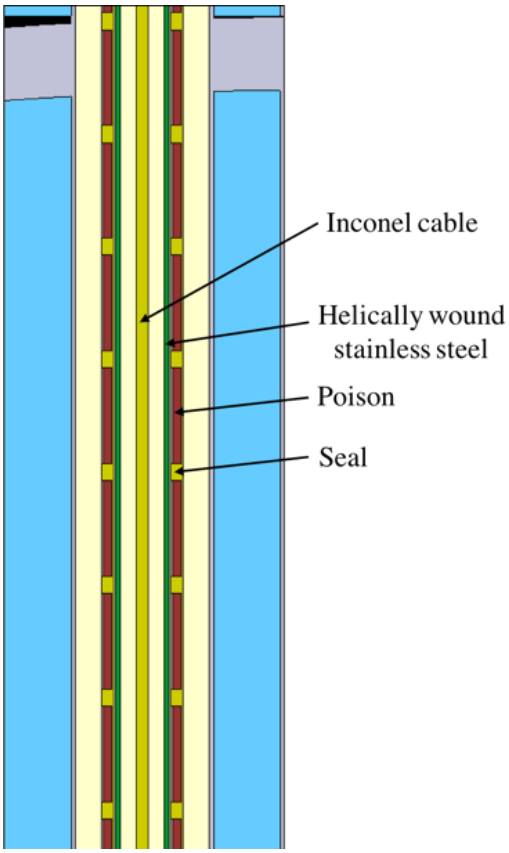

Figure 2.27: Vertical cross section of the control rod in the Serpent2 model.

2.3.2 Reactivity coefficient of ^{235}U concentration

The reactivity coefficient of ^{235}U concentration is defined as the ratio of change in reactivity to the fractional change in ^{235}U loadings in loop while holding the control rods still and it can be obtained from:

$$\Delta\rho = \frac{K(C - C_0)}{C} \tag{2.5}$$

where C is the loadings of ^{235}U in the salt, C_0 is the value at the minimum critical loading which is 65.25 kg, and K is the reactivity coefficient of ^{235}U concentration.

To obtain the reactivity coefficient of ^{235}U concentration, reactivity for cases with various ^{235}U loadings in the loop and the same control rod position was calculated (the core configuration was set as all control rods withdrawn to their upper limit). If the assumption

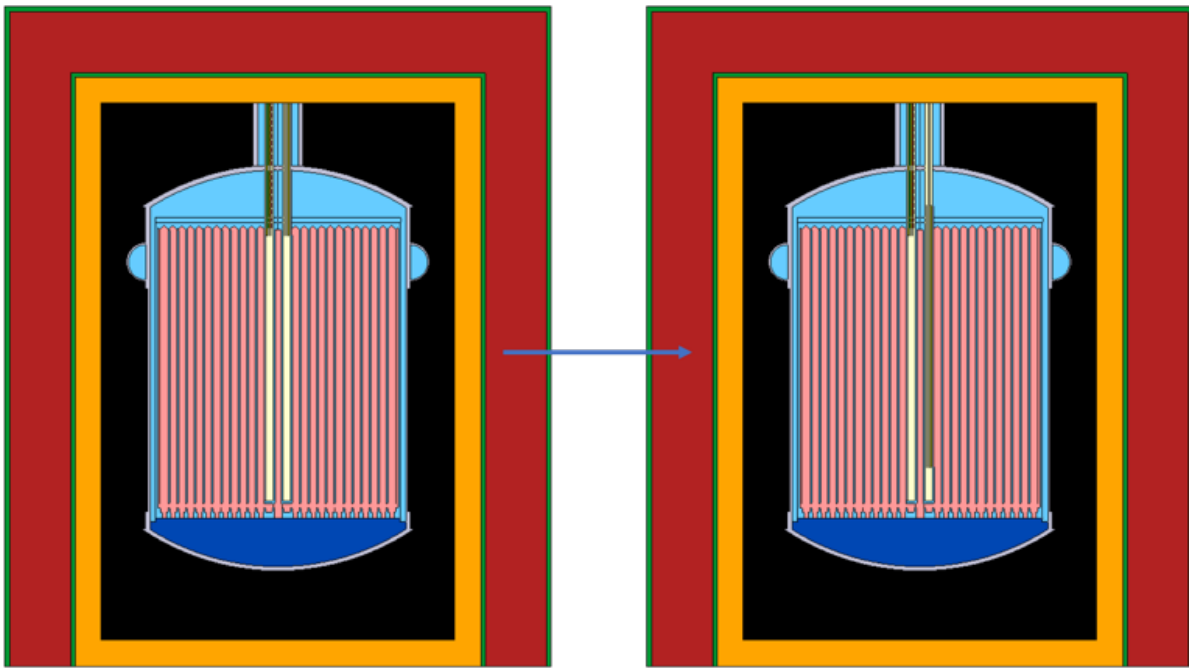

Figure 2.28: Vertical cross section of the control rods, moving rod No.1 from 51 in. (the top) to -2 in. (the bottom), inch was the unit of length to describe control rod travel as in [19].

recognized by ORNL experimenters, that the reactivity coefficient of ^{235}U is nearly independent of ^{235}U mass over the range during the experiment[19], holds true, the average value of this reactivity coefficient can be obtained as the linear regression coefficient as shown in Figure 2.29.

It was found that the accuracy of this calculation relied heavily on the knowledge of fuel salt composition, with certain amount of excess ^{235}U addition for every calculation step. The initial composition of the fuel salt in loop for the rod calibration experiments is listed in Table 2.12 and this composition was calculated by applying a factor of 94.94 % to the total fuel salt composition listed in Table 2.6 to make the ^{235}U loading in loop equal to 65.25 kg, the value specified in [19] as the minimum critical loading. The control rod calibration experiments were performed right after the first zero-power criticality experiment and the reason for the discrepancy between the loop charge of ^{235}U listed in Table 2.6 and the reported value of 65.25 kg in [19] is due to some unknown reasons. This discrepancy won't affect the salt composition used in the criticality benchmark since the total density of salt is settled. However, the control rod calibration experiments are very sensitive to this parameter since the total volume of salt starts to have an impact with excess ^{235}U added. To agree better

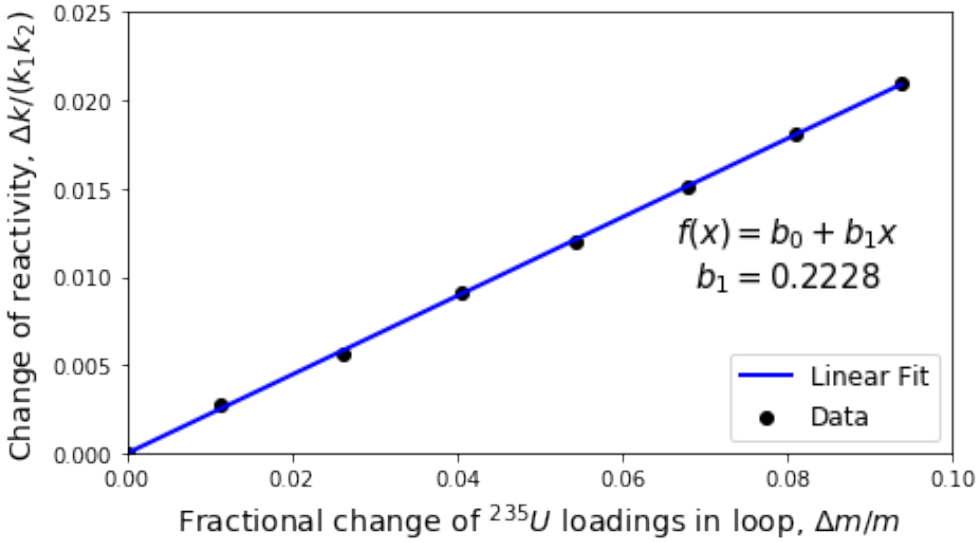

Figure 2.29: Effect of ^{235}U mass on reactivity.

Table 2.12: Composition of fuel salt at the beginning of control rod calibration experiment, applying a factor of 94.94% to the chemical composition of the total fuel salt provided in Table 2.6

Fuel salt component	Value, kg
Li	507.27
Be	293.96
Zr	513.97
U	208.10
^{234}U	0.67
^{235}U	65.25
^{236}U	0.27
^{238}U	141.91
F	3103.22

with the control rod calibration experiments, the value of 65.25 kg for the initial loading of ^{235}U was accepted. Also, with this total ^{235}U in the loop and the corresponding total salt mass of 4626.52 kg in the loop, the total salt volume in the loop was then calculated to be 1.9936 m^3, which agrees well with the reported value of 1.996 m^3 in Table 2.1.

The density of fuel salt at the initial criticality moment was reported as 2.3275 g/cm^3 at 638 °C. Since the fuel salt expansion coefficient is -1.18×10^{-4}/°F, the salt density at 649 °C was calculated to be 2.3223 g/cm^3.

Table 2.13 provides the salt compositions for cases with ^{235}U loading ranging from 65.25 kg to 72 kg in loop. On each step, highly-enriched uranium eutectic (73LiF-27UF_4) was added to exhaust the required ^{235}U loadings. It is assumed that the total salt volume won't be changed significantly during the addition of enriched uranium eutectic and the salt density for each case was calculated by the ratio of salt mass and salt volume.

Table 2.13: Salt composition with various ^{235}U loadings at 649 °C, represented as loadings (in kg) in loop

Case	1	2	3	4	5	6	7	8
Li	507.27	507.33	507.42	507.50	507.59	507.67	507.76	507.85
Be	293.96	293.96	293.96	293.96	293.96	293.96	293.96	293.96
Zr	513.97	513.97	513.97	513.97	513.97	513.97	513.97	513.97
Hf	0.0029	0.0029	0.0029	0.0029	0.0029	0.0029	0.0029	0.0029
U	208.10	208.91	209.98	211.06	212.14	213.21	214.29	215.36
^{234}U	0.67	0.67	0.68	0.69	0.70	0.71	0.72	0.73
^{235}U	65.25	66.00	67.00	68.00	69.00	70.00	71.00	72.00
^{236}U	0.27	0.28	0.28	0.29	0.29	0.29	0.30	0.30
^{238}U	141.91	141.96	142.02	142.08	142.14	142.20	142.26	142.32
Fe	0.75	0.75	0.75	0.75	0.75	0.75	0.75	0.75
Cr	0.13	0.13	0.13	0.13	0.13	0.13	0.13	0.13
Ni	0.14	0.14	0.14	0.14	0.14	0.14	0.14	0.14
O	2.27	2.27	2.27	2.27	2.27	2.27	2.27	2.27
F	3103.22	3103.65	3104.22	3104.79	3105.36	3105.93	3106.51	3107.08
Total	4629.80	4631.10	4632.84	4634.57	4636.30	4638.03	4639.77	4641.50

2.3.3 Rod-shadowing effect

During the additions of enriching capsules, the change in the critical position of the regulating rod (rod No. 1) was recorded as the shim rods (rods No. 2 and No. 3) were inserted into the core. As shown in Figure 2.30, both the effect of inserting a single shim rod (rod No. 2) with rod No. 3 held fixed in the fully withdrawn position, and the effect of inserting rods No. 2 and 3 as a bank (at identical elevation) were recorded . The 45° line represents the situation where the moved shim rod and the regulating rod were at equal position.

This experiment was not incorporated into the MSRE benchmark due to lack of experimental uncertainty information and difficulty to be reproduced accurately. The strategy to make a

preliminary code-to-experiment comparison is provided here.

1. The banked critical positions of rod No. 1, 2 and 3 (all three control rods were inserted together at identical positions) while total ^{235}U loading in loop was 67.94 kg, 69.94 kg and 71.71 kg were measured to be 39.0, 33.3 and 28.4 in. from Figure 2.30. The k_{eff} for these 3 cases were calculated and regarded as the baseline k_{crit} for these three levels of ^{235}U concentration. The reason behind this approach is that the k_{eff} yielded by the benchmark model is biased from unity and this bias may not be constant with different ^{235}U loadings in the system.

2. The objective is to calculate the critical position of the shim rods for each data point in Figure 2.30 while the position of rod No. 1 was set the same as in the figure.

3. For each data point with a certain ^{235}U level and rod No. 1 position, the k_{eff} of 2 cases with the shim rods set with 2 inches apart, surrounding the potential critical position, were calculated.

4. Calculate the critical position of the shim rods by linearly interpolation from the data obtained from the previous step, as shown in Figure 2.31.

5. For each data point, check the k_{eff} obtained from the calculated critical shim rods position to make sure the difference between k_{eff} (calculated) and certain k_{crit}(the baseline) is within 20 pcm. Otherwise, repeat from step 2.

2.3.4 Drift of delay neutron precursors

As discussed in [24], an important phenomenon that is typical of circulating fuel reactors is the drift of DNPs and the consequent effect on reactivity. As fuel circulates in and out of the core relatively rapidly, DNPs drift from the fission location to a new location, inside or outside of the core, before releasing a neutron. Typically, this corresponds to a loss in reactivity as delayed neutrons are either emitted outside of the core, thus, are lost, or in the core, but in a lower importance region, i.e., closer to the core periphery.

In the MSRE the reactivity impact of salt circulation was first evaluated during the initial campaign of zero-power criticality experiments by determining the difference in the required load of ^{235}U in order to make the reactor critical with the fuel salt stationary and circulating. It was found that following the initial critical experiment with fuel salt stationary, when the salt pumping was activated another 8 capsules containing 85 g ^{235}U each were needed to be added to the loop to return the system critical. The reactivity loss due to fuel salt circulation was then estimated to be (-212 ± 4) pcm, given by the vertical difference between the curves in Figure 2.32.

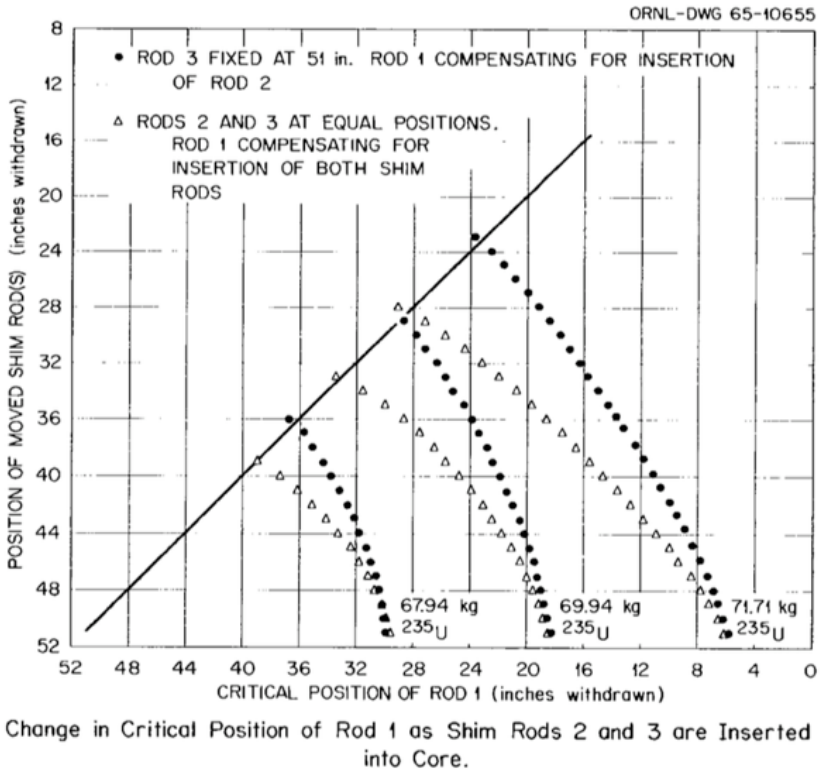

Figure 2.30: Change in critical position of rod No. 1 as shim rods No. 2 and 3 are inserted into core[19].

The assessment of reactivity change due to fuel motion was replicated using the benchmark model. However, the base model was slightly modified as shown in Figure 2.33. The distributor was removed and the shape of the vessel was changed to a cylinder while keeping the volume of the upper head and lower head unchanged. Such modification supports the assumption of a flat velocity profile for the salt through each region and it is not expected to significantly impact the results of the assessment.

The main impact of salt circulation on reactivity is due to a change in the effective delayed neutron fraction, β_{eff}. In order to obtain β_{eff} for the circulating case, the following considerations are made. The ratio between β_{eff} with circulating and stationary salt can be determined as follows[1]:

$$\frac{\beta^c_{eff}}{\beta^s_{eff}} = \frac{\int_{core} D^c(\vec{r}) I^c(\vec{r}) dV}{\int_{core} D^s(\vec{r}) I^s(\vec{r}) dV} \tag{2.6}$$

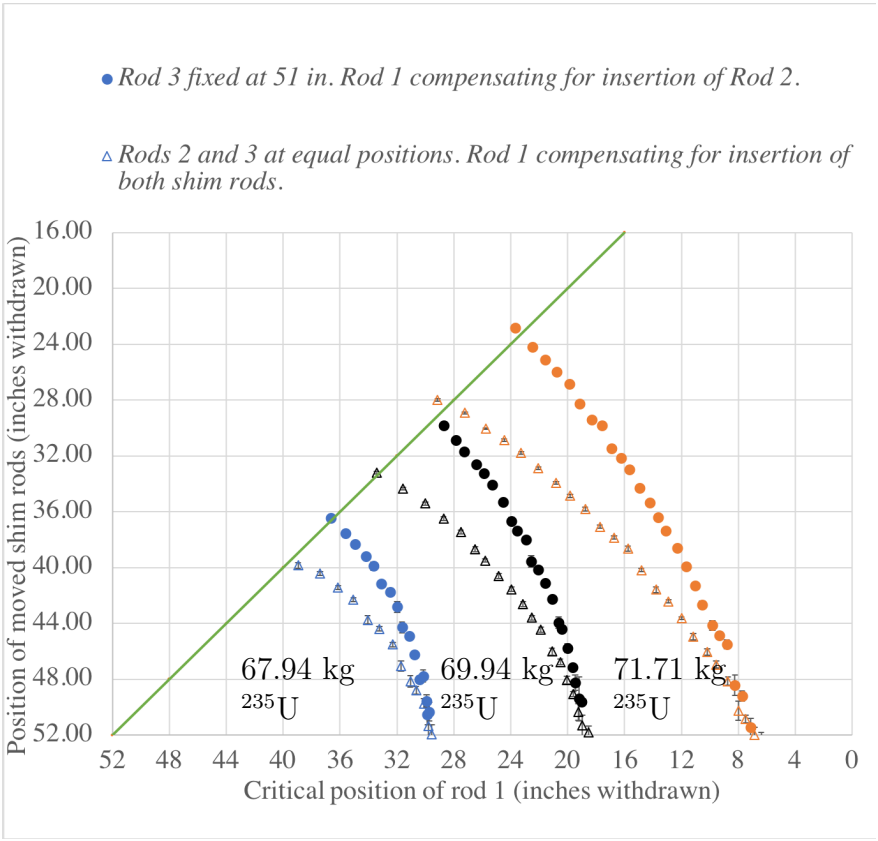

Figure 2.31: Calculated change in critical position of rod No. 1 as shim rods No. 2 and 3 are inserted into core.

where $D(\vec{r})$ is the probability density for DNPs to decay in position $\vec{r}$, and $I(\vec{r})$ is the spatial dependence of the neutron importance. β_{eff} can be calculated through the following equation where k_p is the multiplication factor for prompt neutrons only, which is the same in the circulating and the stationary salt case because prompt neutrons do not flow with the fluid:

$$\beta_{eff} \simeq 1 - \frac{k_p}{k_{eff}} \tag{2.7}$$

Given k_{eff} and β_{eff} in the stationary salt case, k_{eff} in the circulating case is obtained combining Eq 2.6 and Eq 2.7. $I(\vec{r})$, $D^s(\vec{r})$ and $D^c(\vec{r})$ are determined as in Eq 2.8, Eq 2.9 and Eq 2.10,

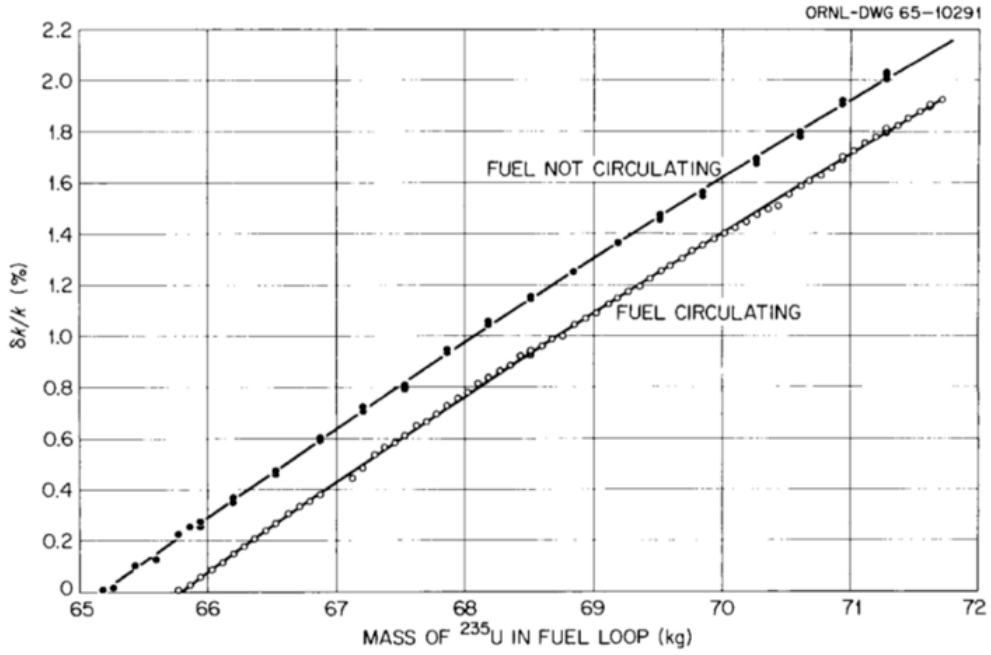

Figure 2.32: Effect of ^{235}U mass on reactivity with and without fuel circulating[19].

respectively. It is assumed that the neutron importance function is the one for a bare, cylindrical core. R_e and H_e represent extrapolated radius and height of the core, respectively. In the stationary case DNPs decay where they are generated, therefore, D^s resembles the fission power distribution. The radial dependence of the fission rate distribution is assumed in the shape of J_0 Bessel function. The axial distribution is obtained as a product of the ratio of fuel salt volume to total volume $\alpha(z)$, and the linear fission rate in the fuel salt $f(z)$ calculated using the simplified MSRE model discussed above. In the case of circulating fuel (Eq 2.10), the DNP drift is accounted for by introducing the term P(z', z) that is the probability for a DNP created in z' to decay in z as determined by the DNP decay constant λ, and the salt's speed v (Eq 2.11). Furthermore, since not all DNPs decay within their first loop an additional term is necessary (Eq 2.10) where $P_{null}(z)$ represents the probability for a DNP born in z does not decay during the first loop, and T is the total time the salt requires for each loop. It is assumed that DNPs perfectly mix before reentering the core, and at the core entrance are evenly distributed over the radial location.

$$I(r,z) = J_0(\frac{2.405r}{R_e})cos(\frac{\pi z}{H_e}) \tag{2.8}$$

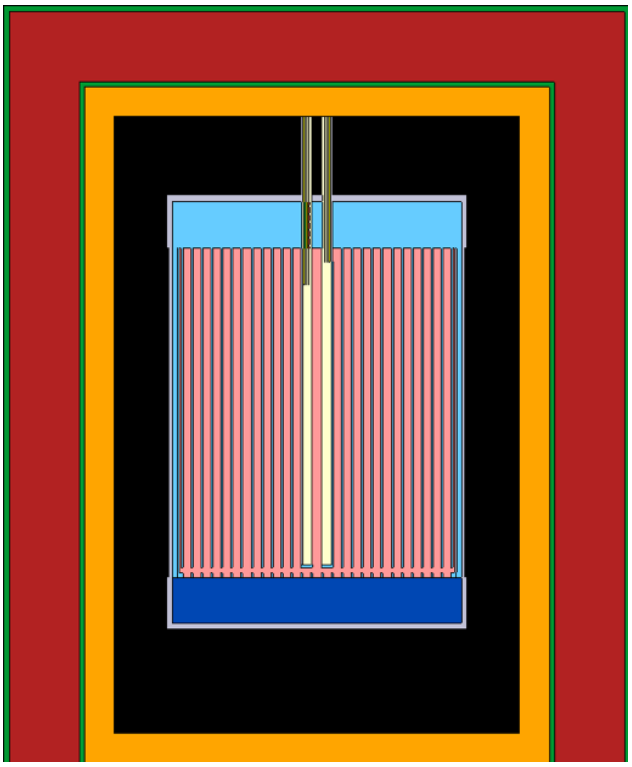

Figure 2.33: Vertical cross section of the simplified MSRE model to calculate the reactivity effect of fuel salt circulation.

$$D^s(r,z) = J_0(\frac{2.405r}{R_e})\alpha(z)f(z) \tag{2.9}$$

$$D^c(r,z) = [\int_{-H/2}^{z} \alpha(z')f(z')P(z',z)dz']J_0(\frac{2.405r}{R_e})+ \frac{\int_{-H/2}^{H/2}\alpha(z')f(z')P_{null}(z')dz'\int_0^R J_0(\frac{2.405r}{R_e})2\pi r'dr'}{\pi R^2} \times P(-H/2,z) \times \frac{e^{\lambda T}}{e^{\lambda T}-1} \tag{2.10}$$

$$P(z_1,z_2) = exp(-\lambda t(z_1,z_2))\frac{\lambda}{v(z_2)} \tag{2.11}$$

2.3.5 Rod-drop effect

In rod-drop experiments, the position of the fission chambers was adjusted to obtain an initial count rate at criticality of $\sim$ 30000 counts/sec. The MSRE instrument shaft was placed remotely relative to the reactor core (see Figure 2.12), minimizing errors due to changes in the spatial flux shape during the rod-drop experiment. Hence, the theoretical time-integrated flux following the rod-drop can be obtained by solving the standard space-independent reactor kinetics equations[19]:

$$\frac{d\psi}{dt} = n(t) \tag{2.12}$$

$$\frac{dn(t)}{dt} = \frac{\Delta\rho(t) - \beta}{\Lambda} n(t) + \sum_{i=1}^{6} \lambda_i C_i(t) \tag{2.13}$$

$$\frac{dC_i(t)}{dt} = \lambda_i C_i(t) + \frac{\beta_i n(t)}{\Lambda}, i = 1, 2, ..., 6 \tag{2.14}$$

where

$\psi(t)$ = time-integrated count rate following the scram,

$n(t)$ = detector count rate following scram,

$C_i(t)$ = DNP concentrations, normalized to detector count rate,

$\Delta\rho(t)$ = reactivity addition vs time following scram,

β_i = production fraction for ith group of delayed neutrons,

λ_i = radioactive decay constant for ith group precursors,

Λ = prompt neutron generation time.

The initial conditions are:

$$\psi(0) = 0, \tag{2.15}$$

$$n(0) \sim 30,000 \text{ counts/sec, initial count rate at critical condition,} \tag{2.16}$$

$$C_i(0) = \frac{\beta_i n(0)}{\Lambda \lambda_i} \tag{2.17}$$

The time variation of the reactivity is governed by:

$$\Delta\rho(t) = \rho(y_0) - \rho[y(t)] \tag{2.18}$$

$$\begin{aligned} y(t) &= y_0, && 0 \le t \le t_e \\ &= y_0 - \frac{1}{2}at^2, && t_e \le t \le t_e + t_m \\ &= y_s, && t_e + t_m \le t \end{aligned} \tag{2.19}$$

where

y = rod position; initial critical position, y_0; scram position, y_s,

$\rho(y)$ = magnitude of reactivity worth corresponding to rod position y,

t_e = effective lag time between scram signal and start of rod drop, ∼20 msec,

a = acceleration during rod fall (∼15 ft/sec^2, basing on drop-time measurements on the MSRE control rods made during pre-nuclear testing[19]),

t_m = time to fall to scram position.

Applying the integral worth curve $\rho(y)$ of different rod group and ^{235}U loadings, after a certain amount of capsules of enriching salt was added, and β_{eff} calculated from the MSRE Serpent2 model, the integrated count rate curve can be obtained by a Python script to solve these equations above. This experiment is not covered in the MSRE benchmark due to lack of experimental uncertainty information. But a preliminary code-to-experiment comparison can be made following the strategies described above.

Chapter 3

Results

3.1 Multiplication factor

3.1.1 Code-to-experiment validation

The experimental k_{eff} for the MSRE first criticality experiment was unity. The assessed bias of the benchmark model (described in Chapter 2) from simplifications is -22 pcm; therefore, the expected k_{eff} for the benchmark model is 0.99978.

The MSRE was modeled with the Monte Carlo code Serpent2 (version 2.1.30[14]), using the ENDF/B-VII.1 cross-section library. The temperature for cross section library is set at 900 K (627 °C) and it is pre-processed for Doppler broadened to 911 K (638 °C) by Serpent2. The thermal scattering library is based on ENDF/B-VII.0 for C in graphite, with temperature 911 K (638 °C) in the core and 305 K (32 °C) in the thermal shield, and H in water, with temperature 305 K in the thermal shield. For thermal scattering, Serpent2 applies temperature interpolation among the two closest temperature libraries. The Serpent2 model of the first criticality experiment of the MSRE with ^{235}U yielded an effective multiplication factor of 1.02132, with a standard deviation (1σ) of 0.000034.

The calculated k_{eff} is 2.154% larger than the experimental and benchmark model value. The complexity of the model makes it difficult to identify the source(s) of such discrepancy. The model was reconstructed based on the public available documents more than 50 years after the experiment. It can be noticed that k_{eff} is particularly sensitive, as obvious, to the main core components that are salt and graphite. Salt composition is particularly challenging to determine as obtained by successive addition. Changes in salt composition would largely impact k_{eff}. At the time the benchmark was prepared, thermal scattering kernel data for salt was not available, although the impact of that is likely to much smaller than the observed difference.

The accuracy of reactor neutronics calculations is sensitive to which nuclear data library was used. It was found that the use of JENDL-3.3 (Japan), compared to ENDF (US) and JEFF (Europe), yielded the k_{eff} for the HTTR (a graphite-moderated, helium-cooled reactor) criticality calculations with the best accuracy (as shown in Table 3.1), which are mainly caused by the slight difference in the neutron capture cross section of carbon at 0.0253 eV among the libraries[11].

Table 3.1: Results for the HTTR benchmark model evaluation of the fully-loaded core critical, all values from the IRPhEP benchmark (HTTR-GCR-RESR-001), Monte Carlo code MCNP was used

Neutron cross-section library	Expected k_{eff}	Calculated k_{eff}	(C-E)/E
ENDF/B-V.2	1.0025	1.0198 ± 0.0001	1.72
ENDF/B-VI.8	1.0025	1.0222 ± 0.0001	1.96
ENDF/B-VII.0	1.0025	1.0229 ± 0.0001	2.03
JEFF-3.1	1.0025	1.0236 ± 0.0001	2.10
JENDL-3.3 with ENDF/B-VII.0 S(α, β)	1.0025	1.0178 ± 0.0001	1.53

According to [11], the neutron capture cross section of carbon at 0.0253 eV was revised based on the latest measurement data in JENDL-4.0 and the discrepancies between the experimental and calculation results of HTTR were further decreased using JENDL-4.0.

The use of ENDF/B-VII.1 vs. JENDL-4.0 cross section for the MSRE critical model led to a difference of (71 ± 5) pcm in k_{eff}, as shown in Table 3.2. In addition, it was found that the eigenvalue for the MSRE core calculated using ENDF/B-VII.1 data would be decreased by (178 ± 5) pcm if only the carbon cross section was replaced by JENDL-4.0 data. The use of JENDL-4.0, especially the carbon cross section, can improve the accuracy of the MSRE calculation but the discrepancy is still around 2%.

Table 3.2: Expected and calculated benchmark-model k_{eff} values

Code (Cross section)	Calculated k_{eff}	Benchmark k_{eff}	100(C-E)/E
Serpent2 (ENDF/B-VII.1)	1.02132 ± 0.000034	0.99978 ± 0.00420	2.154
Serpent2 (JENDL-4.0)	1.02061 ± 0.000034	0.99978 ± 0.00420	2.083

Actually, for benchmarks of a carbon-enriched system, Monte Carlo codes tend to overestimate the k_{eff} of the benchmark model by 1% to 2%, as shown in Table 3.3. The bias is possibly due to uncertainties in the impurity content of the graphite blocks, the accuracy

of the neutron capture cross section of carbon and the accuracy to model the nuclear-grade graphite.

Table 3.3: Difference between calculated k_{eff} and expected k_{eff} for selected full-core benchmarks with carbon-enriched system, all values from the IRPhEP handbook

Benchmark model	Code (Cross section)	Expected k_{eff}	Calculated k_{eff}	100(C-E)/E
HTR10 high-fidelity	MCNP (ENDF/B)	1.00000	1.01190 ± 0.00021	1.190
HTR10 simplified	MCNP (ENDF/B)	1.0131	1.02500 ± 0.00021	1.175
HTTR fully-loaded	MCNP (END/B-VII.0)	1.0025	1.0231 ± 0.0001	2.03
PROTEUS Core 3	MCNP5 (ENDF/B-VII.0)	0.9999	1.00888 ± 0.00007	0.90

3.1.2 Experimental uncertainty analysis

The experimental uncertainty of k_{eff} is the uncertainty caused by experimental parameters. To determine the uncertainty from each parameter, k_{eff} is calculated perturbing one parameter at a time within its uncertainty range, in both positive and negative directions. Δk_i is obtained as follows, assuming that the change of k_{eff} is in proportion to the change of parameter i:

$$\Delta k_i = \frac{u_i}{\delta x_i}(k_{\delta_i} - k_{ref}) \tag{3.1}$$

where u_i is the standard uncertainty of parameter i, and $(k_{\delta_i} - k_{ref})$ is the change in k_{eff} induced by change δx_i on parameter i. When there is a difference between the absolute values of Δk_i calculated from positive and negative perturbations of a parameter, the larger Δk_i is selected, as shown in Table 3.4. For this evaluation, all parameters are considered uncorrelated. To hold this assumption true, for example, when perturbing ^{235}U, ^{234}U and ^{236}U mass fraction in the fuel salt, ^{238}U mass fraction was adjusted accordingly to compensate any mass fraction change and in this way, the uncertainty of k_{eff} from ^{238}U mass fraction uncertainty does not have to be calculated separately to avoid correlation. The total standard uncertainty of k_{eff} is the root mean square of all Δk_i.

The (1σ) uncertainty of the experimental k_{eff} was then calculated to be 420 pcm, as shown in Table 3.4. The graphite density, ^{6}Li enrichment and fuel salt density are the most important uncertainty contributors.

Table 3.4: Individual and total uncertainties of k_{eff}

Item	Nominal and bounding values	Δk_i, pcm
Graphite density	1.86, 1.83-1.87 g/cm^3	334
Fuel salt density	(2.3275 ± 0.0160) g/cm^3	103
Be mass in carrier salt	(309.62 ± 5) kg	8
Zr mass in carrier salt	(541.36 ± 5) kg	12
^{235}U mass fraction in the salt	(1.409 ± 0.007) *wt.*%	81
^{234}U mass fraction in the salt	(0.014 ± 0.007) *wt.*%	74
^{236}U mass fraction in the salt	(0.006 ± 0.006) *wt.*%	17
INOR-8 density	(8.7745 ± 0.0200) g/cm^3	3
Graphite core height	(166.724 ± 1.000) cm	21
Graphite core radius	(70.285 ± 0.200) cm	4
Fuel channel width	(1.0160 ± 0.0127) cm	51
Fuel channel length	(3.0480 ± 0.0127) cm	23
^{6}Li enrichment	(0.005 ± 0.001) *at.*%	172
Boron concentration in graphite	(0.000080 ± 0.000008) *wt.*%	17
Temperature of thermal shield	305 K, 600 K	2
Temperature of fuel salt	(911 ± 1) K	6
Temperature of graphite	(911 ± 1) K	1
The height of the vertical part of the bottom head	(6.475 ± 1.000) cm	9
Outlet pipe thickness	(2.511 ± 0.250) cm	3
Outlet pipe height	(36.180 ± 1.000) cm	4
Distributor thickness	(0.826 ± 0.080) cm	3
Sample basket outer diameter	(5.4287 ± 0.0127) cm	0.0
Sample basket gap	0, 0.0127 cm	5
Cell atmosphere gas composition	Mass fraction, atom fraction	0.0
INOR-8 composition (C mass fraction)	0.06%, 0.08%	5
Mo mass fraction in INOR-8	(17 ± 0.5) *wt.*%	12
Cr mass fraction in INOR-8	(7 ± 0.5) *wt.*%	5
Fe mass fraction in INOR-8	(5 ± 0.5) *wt.*%	4
Impurities in salt	Fe: 162 ± 65, Cr: 28 ± 7, Ni: 30 ± 20, O: 490 ± 49 ppm	12
Helium void in salt	0, 0.076 vol%	5
Salt absorption in graphite	0, 0.0010 vol%	2
Hf in Zr	50 ppm, 0 ppm	12

Impurities in graphite	Ash: 0.0005 ± 0.00005 $wt.\%$, V: 0.0009 ± 0.00009 $wt.\%$, S: 0.0005 ± 0.00005 $wt.\%$	4
Graphite stringer width	$(5.07492^{+0.0000}_{-0.0127})$ cm	13
Poison density	(5.873 ± 0.020) g/cm^3	0.5
Gd_2O_3 mass fraction	(70 ± 1) $wt.\%$	0.6
Control rod position	(118.364 ± 0.127) cm	0.7
Regulating rod	Rod1, Rod2 or Rod3	0.0
Graphite thermal expansion coefficient	$(1.5 \pm 0.2) \times 10^{-6}$ /°F	18
INOR-8 thermal expansion coefficient	$(7.8 \pm 0.2) \times 10^{-6}$ /°F	17
Measurement uncertainty in k_{eff}	-	10
Total (root mean square)	-	420

3.1.3 Further discussions of k_{eff}

As discussed before, the accuracy of Monte Carlo calculations for nuclear reactor neutronics analysis is sensitive to the cross section library including the thermal scattering library used for graphite which is especially important to the MSRE. The effect of different thermal scattering cross section temperatures was evaluated by Serpent2 as shown in Table 3.5. The thermal scattering library is based on ENDF/B-VII.0. It was found that a 100 K change in temperature of thermal scattering cross section of carbon in graphite will result in more than 500 pcm difference in k_{eff}.

Table 3.5: Impact of temperature of thermal scattering cross section

C-nat in graphite	C-nat in thermal shield	H-1 in thermal shield	k_{eff} (1σ)	Diff, pcm
800K	296K	293.6K	1.02723(10pcm)	0
911K (interpolated)	305K (interpolated)	305K (interpolated)	1.02132(3.4pcm)	-591
1000K	400K	350K	1.01640(10pcm)	-1083

The detailed fuel salt composition at the critical point of the MSRE zero-power experiment remains mysterious until a thorough investigation to the fuel salt preparation was conducted, mainly basing on the technique report describing the chemical behaviour in the fuel salt

during pre-nuclear operations[25]. The benchmark salt composition is chosen as the nominal salt composition provided in [25] that recorded how much salt component was put into the primary loop and this composition was checked and corrected by the experimenters to be self-consistent. There are two other reference salt compositions: one is from the chemical analyses performed with samples of the fuel salt during the experiment; another one is in the form of anticipated mole fraction of the fuel salt (65.0LiF-29.17BeF_2-5.0ZrF_4-0.83UF_4[25]), which is close to the fuel salt composition specified or expected for MSRE power operation provided in [19] (65LiF-29.2BeF_2-5ZrF_4-0.8UF_4). All of these salt options were evaluated on the benchmark model (as shown in Table 3.6), keeping the enrichment of all uranium isotopes, impurities concentration and total salt density the same.

Table 3.6: Impact of fuel salt composition, the impurities are assumed to be 0.071 wt.% for all salt options

Salt option	Li, wt. %	Be, wt. %	Zr, wt. %	U, wt. %	k_{eff} (1σ)	Diff, pcm
Benchmark salt (nominal)	10.957	6.349	11.101	4.495	1.02132 (3.4pcm)	0
Chemical analytical composition	10.327	6.695	11.016	4.440	1.02248 (10pcm)	116
Anticipated mole fraction[a]	10.970	6.324	10.972	4.641	1.02595 (10pcm)	463

[a] Composition is 65.0LiF-29.17BeF_2-5.0ZrF_4-0.83UF_4

It was found that the result from chemical analyses shows bias in determination of lithium and beryllium when compared with the other two. Actually similar measurement bias of chemical analysis was noticed on the flush salt as well. The flush salt, with a nominal composition of ^{7}LiF-BeF_2 (66-34 mole%) was employed to flush the fuel system initially and later, on occasions before and after maintenance periods. The average composition of the flush salt as determined by chemical analysis was ^{7}LiF-BeF_2 ($63.56 \pm 0.005 - 36.44 \pm 0.005$ mole%). Examinations of the material balance indicated that this discrepancy was due to an analytical bias.

The reason for choosing the nominal salt composition, instead of the anticipated mole fraction specified in [19], in the benchmark is to keep the best consistency among reference on the key parameter for the critical experiment, which is the mass fraction of ^{235}U in this case. The ^{235}U mass fraction calculated from the nominal composition, which is 1.409%, agrees the best with the tolerance range of ($1.408 \pm 0.007\%$) provided in [19].

3.1.4 Sensitivity coefficients for k_{eff} from cross section data uncertainties

Table 3.7 provides the sensitivity coefficients for the k_{eff} from nuclear data uncertainties in each important element in all the materials using Serpent2 sensitivity coefficient calculation capabilities[2]. Combined with SCALE6.2 56-group covariance matrices through the so-called sandwich rule, uncertainty for k_{eff} from cross sections was estimated to be 664 pcm and the most important uncertainty contributors are listed in Table 3.8.

Table 3.7: Sensitivity coefficients for k_{eff} from cross section data uncertainties, $\frac{dk/k}{d\sigma/\sigma}$

Nuclide	Total ($\times 10^{-5}$)	Elastic scattering ($\times 10^{-5}$)	Neutron capture[a] ($\times 10^{-5}$)	Fission ($\times 10^{-5}$)
Li-6	-1,430	0.04	-1,430	n/a
Li-7	770	2,010	-1,380	n/a
Be-9	2,920	3,250	-340	n/a
Zr-90	3	50	-64	n/a
Zr-91	-520	150	-670	n/a
Zr-92	-16	130	-160	n/a
Zr-94	-36	5	-54	n/a
Zr-96	-86	2	-89	n/a
F-19	8,410	8,080	-1,070	n/a
C-nat	51,400	39,210	-1,760	n/a
B-10	-650	0.2	-650	n/a
U-235	22,990	47	-14,080	37,020
U-238	-8,470	610	-9,170	63

[a] Reactions with no neutron yield.

Table 3.8: Uncertainties for k_{eff} from cross section data uncertainties

Reaction	Uncertainties, pcm
^{235}U $\bar{\nu}$ × ^{235}U $\bar{\nu}$	373
C elastic × C elastic	264
^{235}U χ × ^{235}U χ	257
^{7}Li(n, γ) × ^{7}Li(n, γ)	197
^{235}U(n, γ) × ^{235}U(n, γ)	172
^{19}F elastic × ^{19}F elastic	150
^{235}U(n, f) × ^{235}U(n, γ)	128
^{235}U(n, f) × ^{235}U(n, f)	120
^{58}Ni(n, γ) × ^{58}Ni(n, γ)	97
^{19}F inelastic × ^{19}F inelastic	96

3.1.5 k_{eff} of models with geometry simplifications

Given the complexity of the MSRE model, it might be challenging for many codes to reproduce the full details of the model. Here, the impacts of some geometry modifications were evaluated such that reference k_{eff} for the MSRE model with various levels of simplifications is provided.

1. Impact of removing the flow distributor

   The shape of the flow distributor, arranged at the top of the vessel to connect with the fuel salt inlet, is the half of a torus (see Figure 2.3), which may be difficult for some codes to build the geometry. If the distributor is removed from the model, $k_{eff} = 1.02032 \pm 0.000035$ (a -0.098% change as compared to the reference value since we lose some salt in the system).

2. Impact of changing the shape of the top and bottom head of the vessel

   The shapes of the top and bottom head of the reactor vessel are two identical torispherical domes. If they are modeled as flat rather than concave surfaces whereas the height of the vessel is conserved (see Figure 3.2), $k_{eff}=1.02380 \pm 0.000035$ (a 0.243% change as compared to the reference value since we add more salt in the system).

3. Impact of the sample basket

   The sample baskets are located in the most important region of the core and their geometry is complicated in the MSRE benchmark model. The following simplifications are considered:

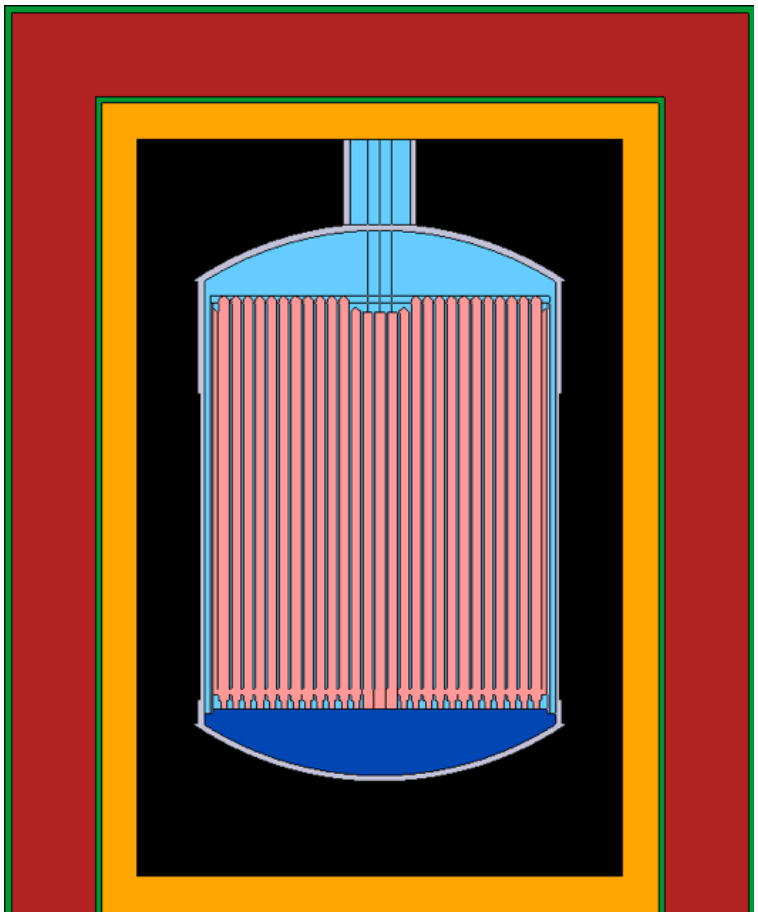

Figure 3.1: Vertical cross section of the MSRE model without the distributor (at $y = 0$).

- the sample basket is modeled as a regular channel, therefore, made of graphite (Figure 3.3b): k_{eff}=1.03790 ± 0.000035 (a 1.623% change as compared to the reference value);
- the materials in the sample basket are homogenized and the basket outer radius and the channel shape are kept unchanged (Figure 3.3c): k_{eff}=1.02094 ± 0.000034 (a −0.037% change as compared to the reference value). The change of k_{eff} is very small.

4. Impact of the shape of the fuel channel

   The shape of the fuel channel is a rectangular with round corners which may be difficult to model for some codes. The following options are considered for simplifying the geometry of the fuel channel:

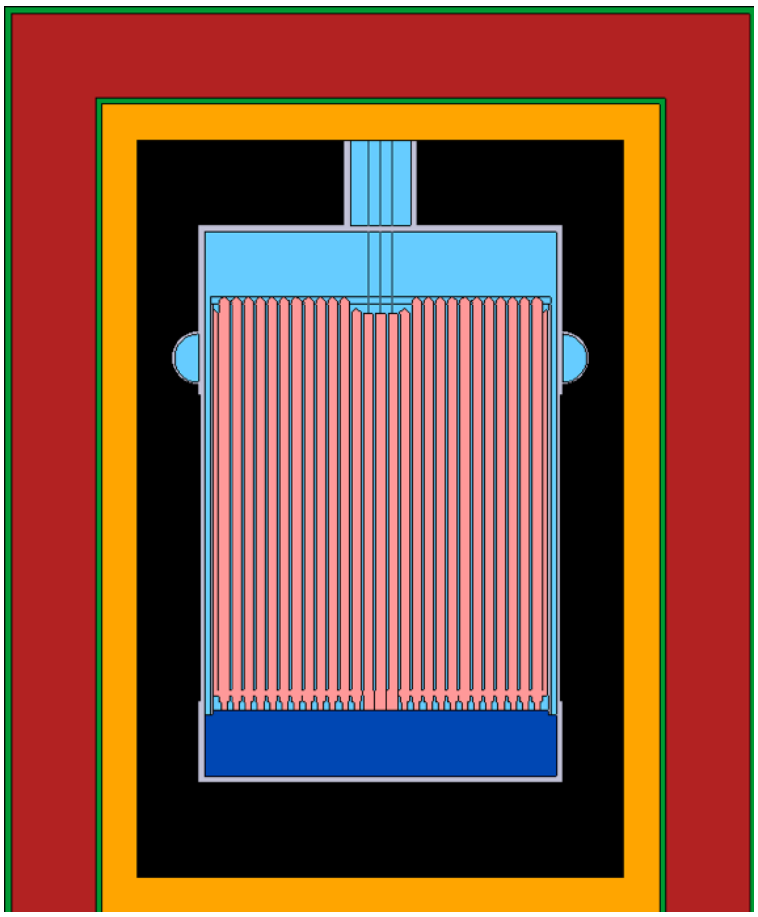

Figure 3.2: Vertical cross section of the MSRE model with flat top and bottom section (at $y = 0$).

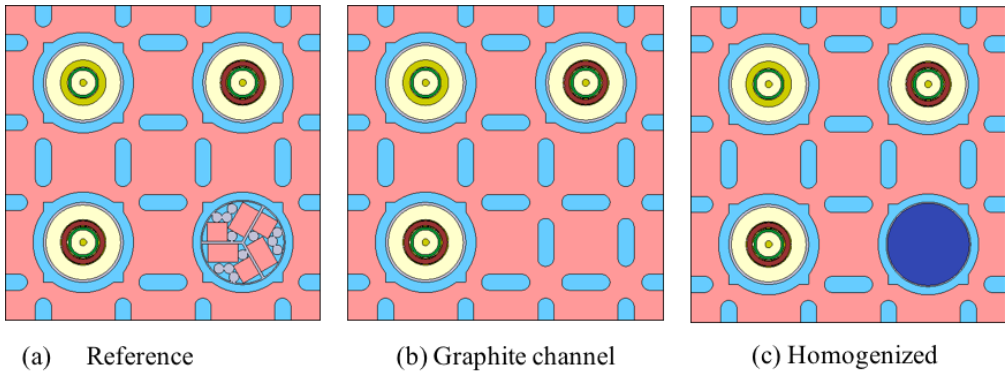

Figure 3.3: Comparison of models for the sample basket.

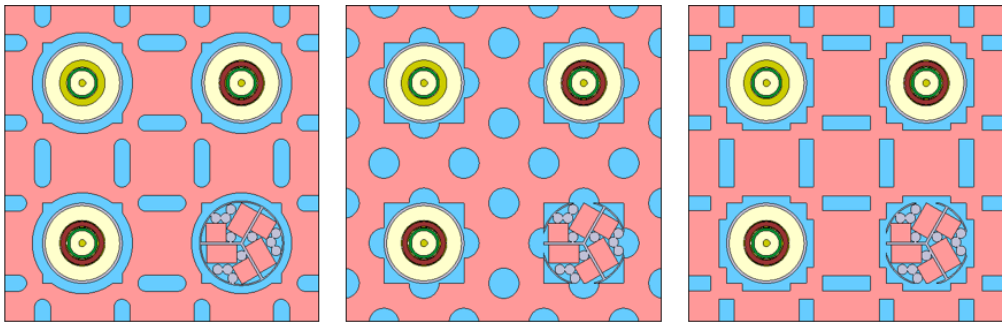

(a) Reference (b) Circular channel (c) Rectangular channel

Figure 3.4: Comparison of models for the fuel channel.

- circular channel with 0.957 cm radius in order to maintain the same cross-sectional area of the reference channels (Figure 3.4b): k_{eff}=1.02450 ± 0.000034 (a 0.311% change as compared to the reference value);
- rectangular channel (Figure 3.4c) with the long side equal to the length of the long side of the reference channel (3.048 cm) and the half length of the short side (0.472 cm) adjusted to preserve the channel cross sectional area: k_{eff}=1.02151 ± 0.000035 (a 0.019% change as compared to the reference value). The change of k_{eff} is very small.

5. Impact of removing the thermal shield

   If the thermal shield and insulation layer are removed from the model (see Figure 3.5), k_{eff}=1.01228 ± 0.000033 (a −0.885% change as compared to the reference value due to loss of neutrons that could be reflected back to the core from the thermal shield).

Table 3.9 summarizes the calculations results of models with different geometry simplifications.

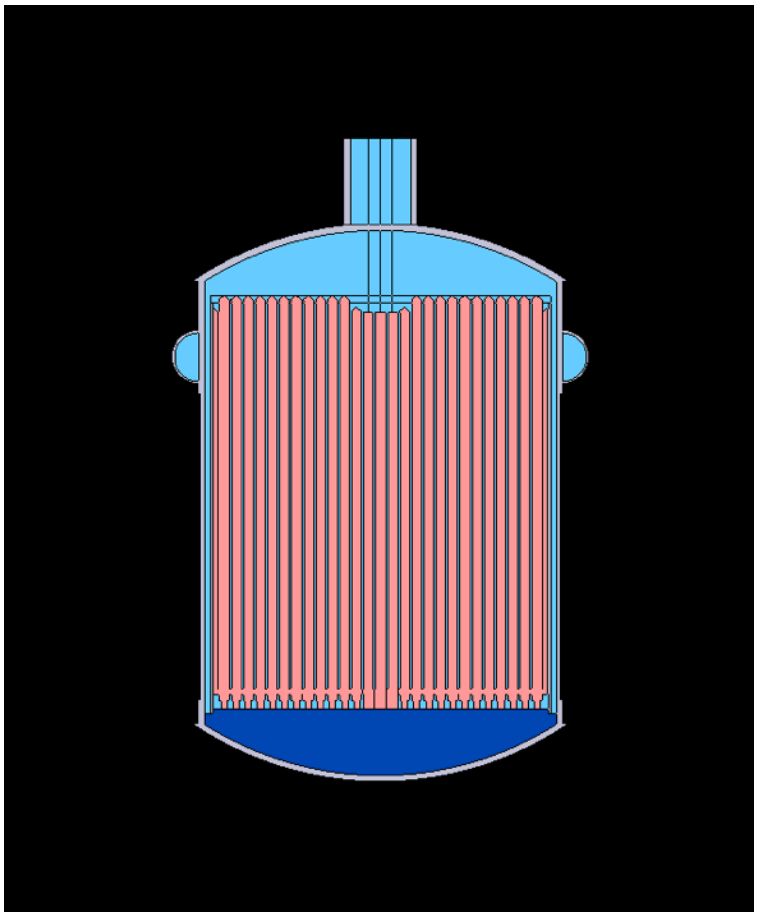

Figure 3.5: Vertical cross section of the MSRE model without thermal shield and insulation layer (at $y = 0$).

Table 3.9: Impact of geometry changes on k_{eff}

Case	k_{eff}	$100(k_{eff} - k_{ref})/k_{ref}$ [a]
No distributor	1.02032 ± 0.000035	-0.098
With flat top and bottom surfaces of the vessel	1.02380 ± 0.000035	0.243
Replace the sample basket by graphite channel	1.03790 ± 0.000035	1.623
Make the sample basket homogeneous	1.02094 ± 0.000034	-0.037
Circular fuel channels	1.02450 ± 0.000034	0.311
Rectangular fuel channel	1.02151 ± 0.000036	0.019
No thermal shield and insulation layer	1.01228 ± 0.000033	-0.885

[a] $k_{ref} = 1.02132 \pm 0.000034$.

3.2 Reactivity Effect

3.2.1 Experimental uncertainty analysis

The evaluation of the MSRE reactivity effect benchmark starts with the uncertainty analysis of experimental values. An uncertainty of 2% was attributed to the reported reactivity measurements from ORNL. It was believed that the experimental measurement uncertainty was significantly larger than the computation process uncertainty and the uncertainty of reactor period measurement contributed the most to the experimental uncertainty.

Also, there's an uncertainty caused by the correction factors which were applied to the rod sensitivity measurements to pull the measurements all on the basis of one ^{235}U concentration. This correction factor was calculated by ORNL and now checked on the MSRE benchmark model. The reactivity change of rod No. 1 between fully withdrawn and fully inserted positions was evaluated with various ^{235}U loadings in loop and the correction factor for a certain ^{235}U concentration was defined as follows:

$$cf(x) = \frac{\rho_1(x_0) - \rho_0(x_0)}{\rho_1(x) - \rho_0(x)} \tag{3.2}$$

where x is the current ^{235}U loadings in loop, x_0 is initial critical ^{235}U loading that is 65.25 kg, $\rho_1(x)$ is the reactivity with rod No. 1 fully withdrawn and $\rho_0(x)$ is the reactivity with rod No.1 fully inserted into the core.

It was found that the correction factor calculated in the benchmark model was almost linearly with the ^{235}U concentration as shown in Figure 3.6. The largest deviation from the correction factors calculated by the MSRE benchmark model to those provided by ORNL, applied for a certain ^{235}U level, was found to be less than 2%. So, the uncertainty due to the applied correction factor was assumed to be 2% by a conservative estimation. No significant bias or systematic error was observed for the correction factor applied on the measurements. The uncertainty of rod worth measurements is now the square root of the sum of the squares of the experimental uncertainty and the uncertainty in the correction factor, which is 2.83%. It was found that the reactivity effect such as the control rod worth is not sensitive to the most important uncertainty contributors of the multiplication factor. The change of the control rod worth for rod No. 1 due to 1σ change of the graphite density is only 0.014% of the original value and is negligible due to 1σ change of ^{6}Li enrichment. Therefore, it is reasonable to infer that the uncertainty of reactivity effects caused by uncertainty of model parameters are insignificant compared to 2.83%.

The basic assumption supporting the application of correction factor is that the shape of integral worth vs position curve for control rods is unaffected by ^{235}U concentration. This assumption was checked on the MSRE benchmark model. The plot of normalized rod worth

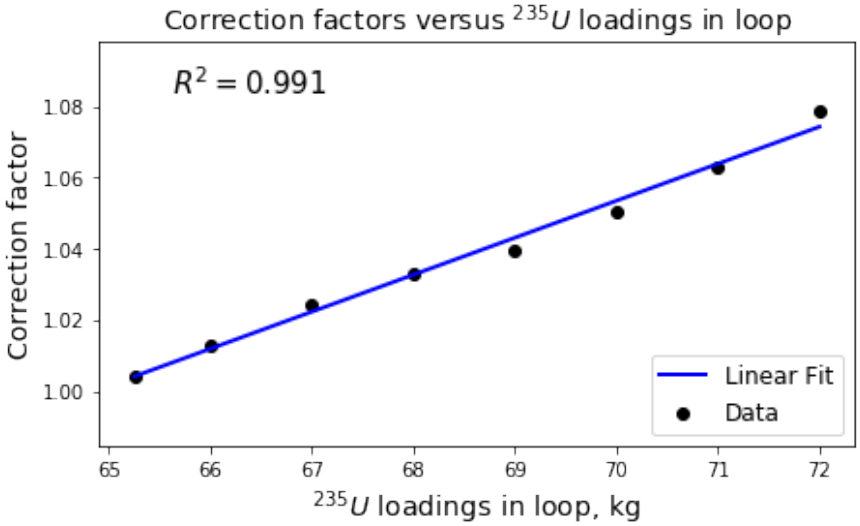

Figure 3.6: Correction factors with different ^{235}U loadings in loop.

$f(z)$ vs. normalized rod position z with three different ^{235}U concentrations is shown in Figure 3.7, where z measures the height of rods above the lower limit and this curve was normalized to zero at lower limit ($z = 0$) and to unity at the upper limit ($z = 1$). The three curves in Figure 3.7 differ very little, demonstrating the feasibility of this assumption.

3.2.2 Integral and differential rod worth

For the differential control rod worth evaluation, rod No. 1 was moved from the fully withdrawn position to the bottom of the control rod thimble while other two rods were held fully withdrawn. The integral worth curve of rod No. 1 is shown in Figure 3.8. The differential worth of rod No. 1 is shown in Figure 3.9 and Figure 3.10 with different Δx in calculating the change of reactivity. The use of a smaller Δx does not improve the accuracy of differential rod worth calculation since the control rod does not consist of homogeneous material but features a special design as shown in Figure 2.9. The code-to-experiment comparison of the differential rod worth is shown in Table 3.10.

Table 3.10: Differential worth of control rod No. 1 for the MSRE at initial critical ^{235}U loading

Rod position, inch	Calculated value, pcm/cm	Benchmark value, pcm/cm	C/E

49	6.05 ± 0.46	6.7 ± 0.2	0.90 ± 0.07
45	8.81 ± 0.46	10.0 ± 0.3	0.88 ± 0.05
41	13.10 ± 0.46	13.9 ± 0.4	0.94 ± 0.04
37	15.61 ± 0.46	17.7 ± 0.5	0.88 ± 0.04
33	19.01 ± 0.45	20.8 ± 0.6	0.92 ± 0.03
29	21.87 ± 0.46	23.0 ± 0.6	0.95 ± 0.03
25	23.23 ± 0.47	24.2 ± 0.7	0.96 ± 0.03
21	22.85 ± 0.47	24.4 ± 0.7	0.94 ± 0.03
17	23.25 ± 0.47	23.3 ± 0.7	1.00 ± 0.03
13	22.19 ± 0.48	20.9 ± 0.6	1.06 ± 0.04
9	20.02 ± 0.48	17.5 ± 0.5	1.15 ± 0.04
5	16.04 ± 0.47	13.2 ± 0.4	1.22 ± 0.05
2	13.46 ± 0.47	9.6 ± 0.3	1.41 ± 0.06
0	11.66 ± 0.48	7.1 ± 0.2	1.64 ± 0.08

The calculated differential rod worth tends to be shifted to the left from the benchmark value overall and this shift led to the mismatch in the integral worth curve as well. The higher calculated differential worth at 0 in. in Figure 3.9 indicates that the rod in the model was not inserted low enough at its fully inserted position. The initial fully withdrawn position of the control rods was obtained indirectly since, as stated before, the benchmark model was thermally expanded downward by assumption. If we artificially lower the upper limit of all rods by 10 cm, which means inserting all rods 10 cm more at the beginning, the mismatch in both the integral and differential worth could be corrected in the right direction as shown in Figure 3.11 and Figure 3.12. This phenomenon indicates the need to further investigate the initial position of all rods at room temperature and the thermal expansion mechanism of them.

3.2.3 Reactivity Equivalent of ^{235}U

Reactivity for cases with ^{235}U loadings of 65.25 kg, 66 kg, 67 kg, 68 kg, 69 kg, 70 kg, 71 kg and 72 kg in the loop was calculated, while the core configuration is set as all control rods withdrawn to their upper limit. The results are plotted in Figure 3.13.

The average value of reactivity equivalent of ^{235}U additions are obtained as the linear regression coefficient as shown in Figure 2.29. The calculated value of the reactivity equivalent of ^{235}U additions is provided in Table 3.11. The calculated value and the benchmark value are in good agreement (within 1σ).

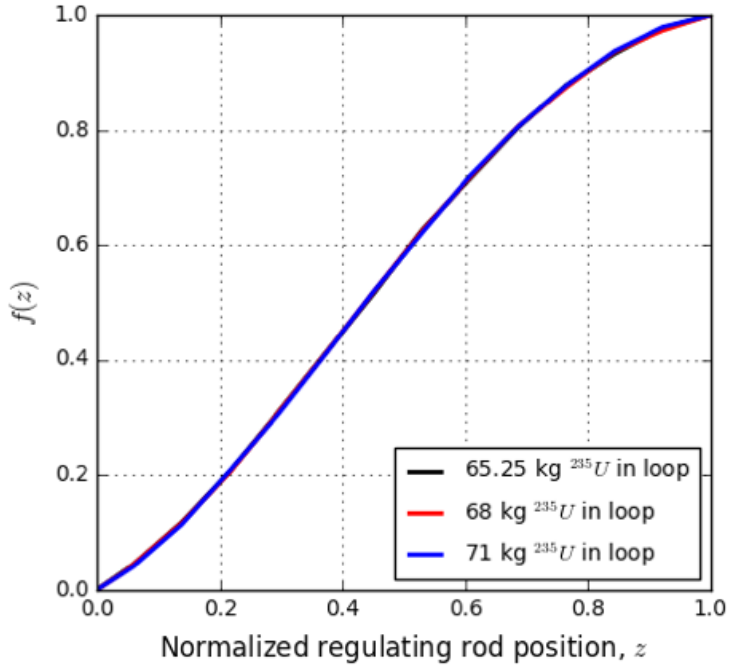

Figure 3.7: Regulating curve of rod No. 1 in the presence of (a) 65.25 kg ^{235}U in loop, (b) 68 kg ^{235}U in loop and (c) 71 kg ^{235}U in loop.

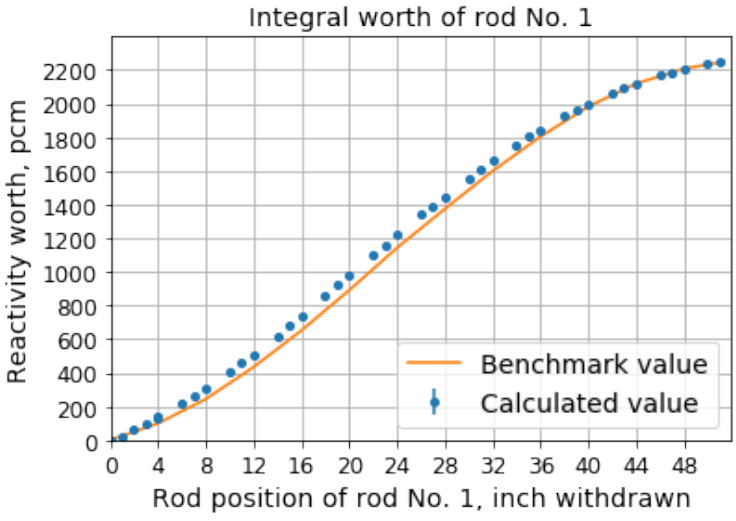

Figure 3.8: Integral worth of control rod No. 1.

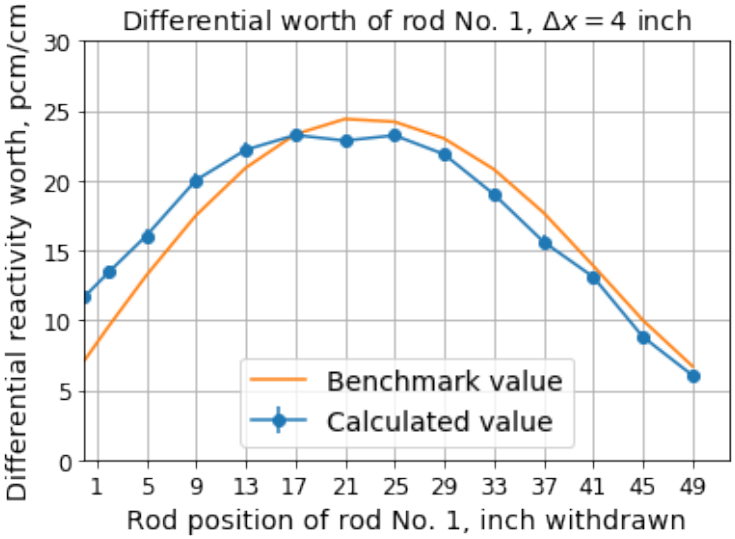

Figure 3.9: Differential worth of control rod No. 1, $\Delta x = 4$ inch.

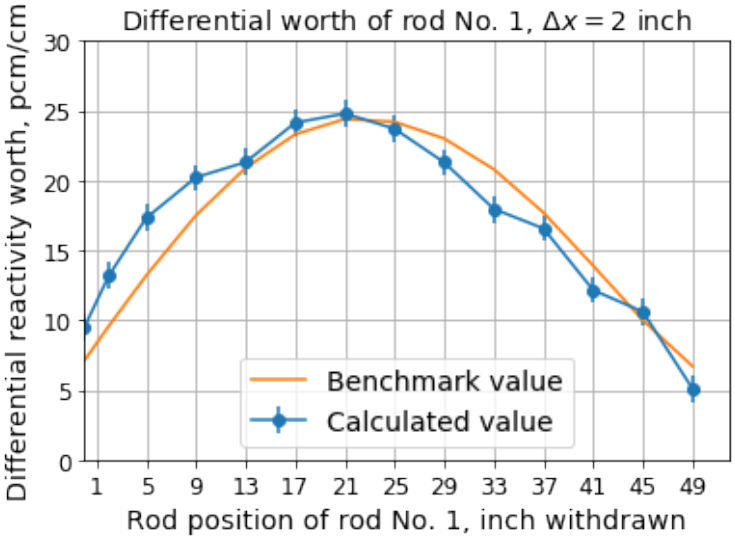

Figure 3.10: Differential worth of control rod No. 1, $\Delta x = 2$ inch.

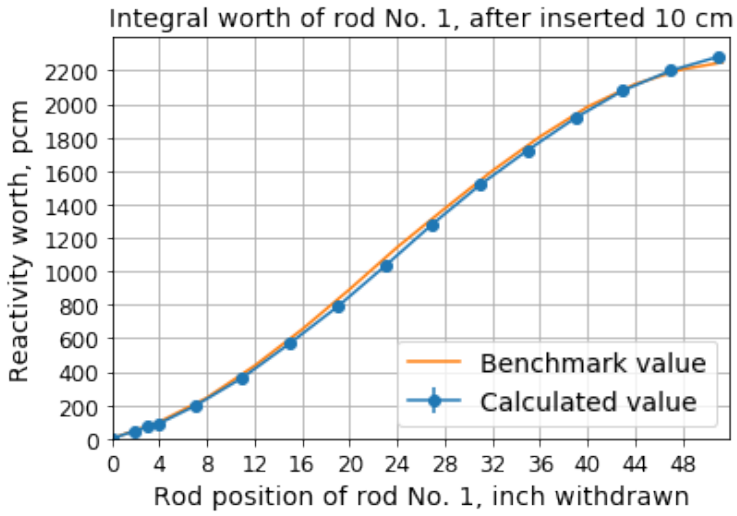

Figure 3.11: Integral worth of rod No. 1 after inserting all control rods 10 cm at the beginning positions.

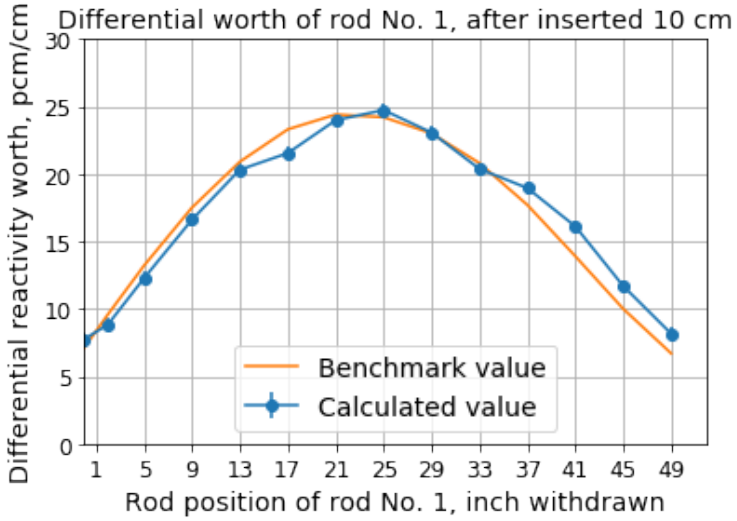

Figure 3.12: Differential worth of rod No. 1 after inserting all control rods 10 cm at the beginning positions.

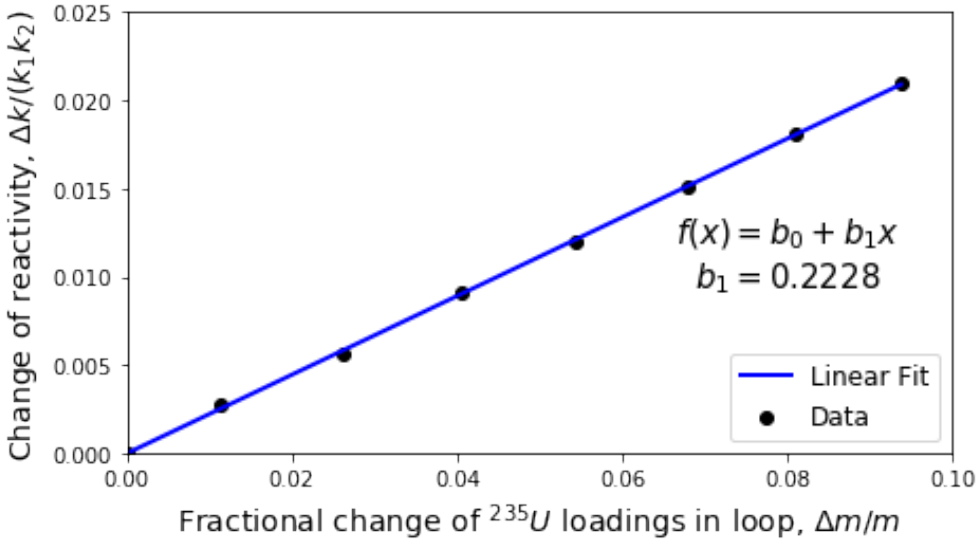

Figure 3.13: Effect of ^{235}U mass on reactivity.

Table 3.11: Reactivity equivalent of ^{235}U additions, $(\delta\rho)/(\delta m/m)$

Calculated value	Benchmark value	C/E
0.2228 ± 0.0014	0.223 ± 0.006	0.999 ± 0.029

3.2.4 Rod-shadowing effect

Rod-shadowing effect refers to the change in the critical position of the regulating rod (rod No. 1) as the shim rods (rods No. 2 and No. 3) were inserted into the core. Using the method described in Chapter 2, a preliminary code-to-experiment comparison of the rod-shadowing effect was conducted as shown in Figure 3.14. The calculated values and experimental values roughly agreed.

3.2.5 Worth of rod bank

Utilizing the results of the rod-shadowing effect experiment, the reactivity worthies of various shim and regulating rod combinations, also called rod bank, can be obtained assuming that the shape of the bank worth curve is sufficiently close to that for the single regulating rod[19]. The integral worth vs position curve for different rod banks was checked on the MSRE benchmark model. They come in slightly different shapes, as shown in Figure 3.15, but in general are very similar.

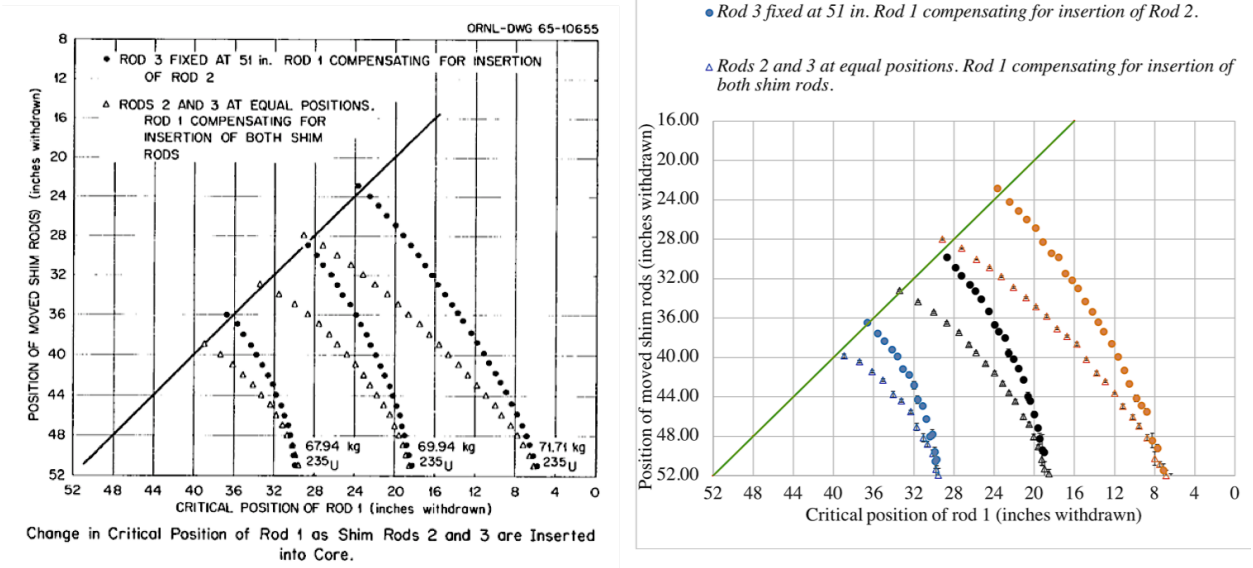

Figure 3.14: Rod-shadowing effect comparisons between calculated values and experimental values.

In the benchmark model, the control rod bank worth from rod bank No. 1 & 2 and rod bank for all three rods were calculated from the change of reactivity with rod bank fully withdrawn (51 in. withdrawn) and fully inserted (0 in. withdrawn) at three certain ^{235}U loading level. All the rods included in one bank were at held at identical elevations. The calculated k_{eff} for each case is shown in Table 3.12.

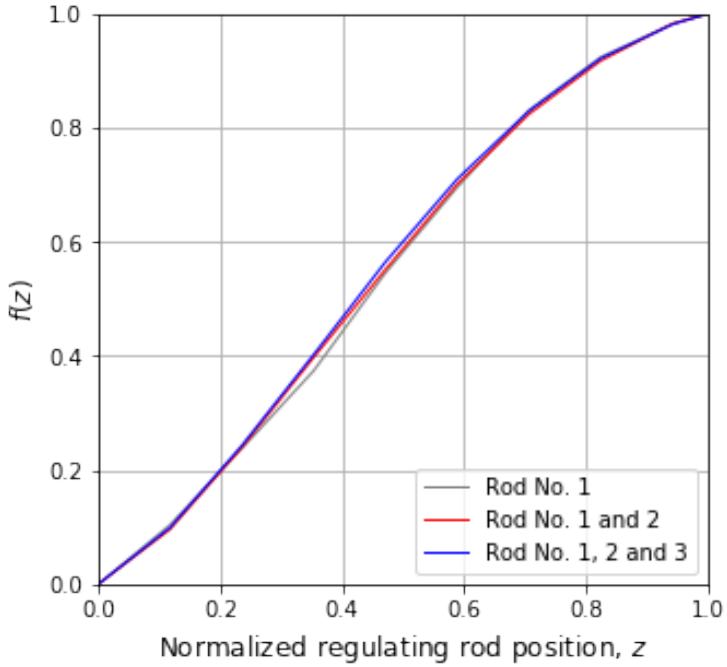

Figure 3.15: Regulating curve of (a) rod No. 1, (b) rod No. 1 and 2 and (c) rod No. 1, 2 and 3.

Table 3.12: k_{eff} for control rod bank worth calculations

Rod group	^{235}U in loop, kg	Rod group position	Calculated k_{eff}
1-2	67.94	Fully withdrawn	1.02997 ± 0.000095
		Fully inserted	0.988803 ± 0.00010
1-2	69.94	Fully withdrawn	1.03626 ± 0.000093
		Fully inserted	0.995559 ± 0.000097
1-2	71.71	Fully withdrawn	1.04186 ± 0.000094
		Fully inserted	1.00148 ± 0.000097
1-2-3	67.94	Fully withdrawn	1.02997 ± 0.000095
		Fully inserted	0.973297 ± 0.00010
1-2-3	69.94	Fully withdrawn	1.03626 ± 0.000093
		Fully inserted	0.980123 ± 0.000099
1-2-3	71.71	Fully withdrawn	1.04186 ± 0.000094
		Fully inserted	0.985755 ± 0.00010

The calculated values of the control rod bank worth are provided in Table 3.13. The cal-

culated values and the benchmark values are in good agreement (within 1σ for 5 case and within 2σ for only 1 case).

Table 3.13: Control rod bank worth (total worth at full insertion)

Rod group	^{235}U in loop, kg	Calculated value, pcm	Benchmark value, pcm	C/E
1-2	67.94	4042 ± 14	4099 ± 116	0.99 ± 0.03
1-2	69.94	3945 ± 13	3975 ± 112	0.99 ± 0.03
1-2	71.71	3870 ± 13	4075 ± 115	0.95 ± 0.03
1-2-3	67.94	5653 ± 14	5596 ± 158	1.01 ± 0.03
1-2-3	69.94	5526 ± 14	5611 ± 159	0.98 ± 0.03
1-2-3	71.71	5463 ± 14	5570 ± 158	0.98 ± 0.03

3.2.6 Reactivity effects of fuel circulation

Using the method described in Chapter 2, the calculated value for the reactivity loss due to fuel circulation is provided in Table 3.14. The calculated value shows good agreement with the benchmark value (within 1σ).

Table 3.14: Reactivity loss due to fuel circulation

Calculated value, pcm	Benchmark value, pcm	C/E
222 ± 10	212 ± 6	1.05 ± 0.06

It was assumed that the fuel salt speed is 6.11 cm/s in the lower head, 17.71 cm/s in the channeled region and 6.12 cm/s in the upper head. The time spent outside of the core is 32% of the total time required to complete a loop (25.2 s in total as shown in Table 2.1). The change of β_{eff} due to fuel circulation was calculated to be -224.83 pcm.

Figure 3.16 compares the probability of DNP decay in the centerline of the reactor for different precursor groups in the circulating and in the stationary case. It can be noticed that the fuel circulation has little to no effect on the DNP distribution for short lived DNPs compared to the case when the fuel is stationary, whereas it effectively flattens the distribution for long lived ones.

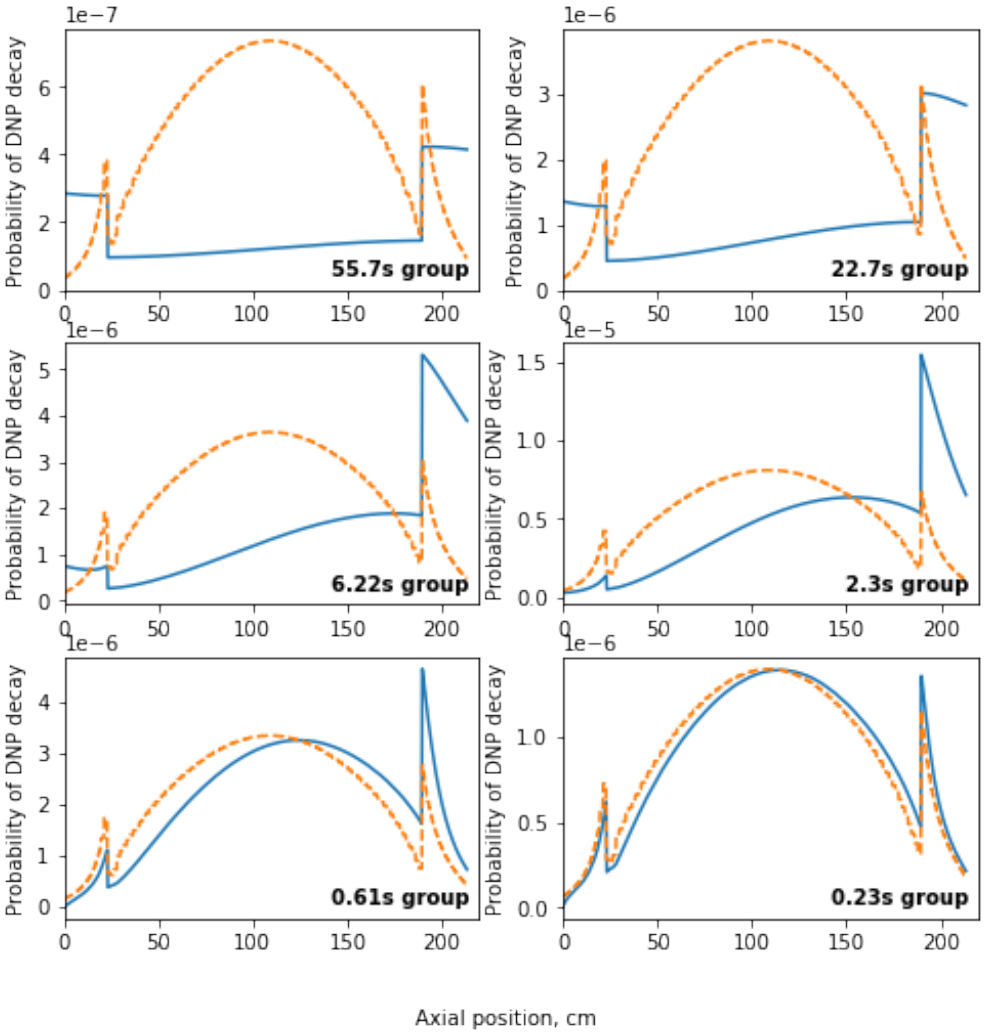

Figure 3.16: The probability of DNP decay in the centerline of the reactor in the stationary (dashed line) and the circulating (solid line) case for six decay groups—the spikes are due to the larger volume of salt in the bottom and top plena.

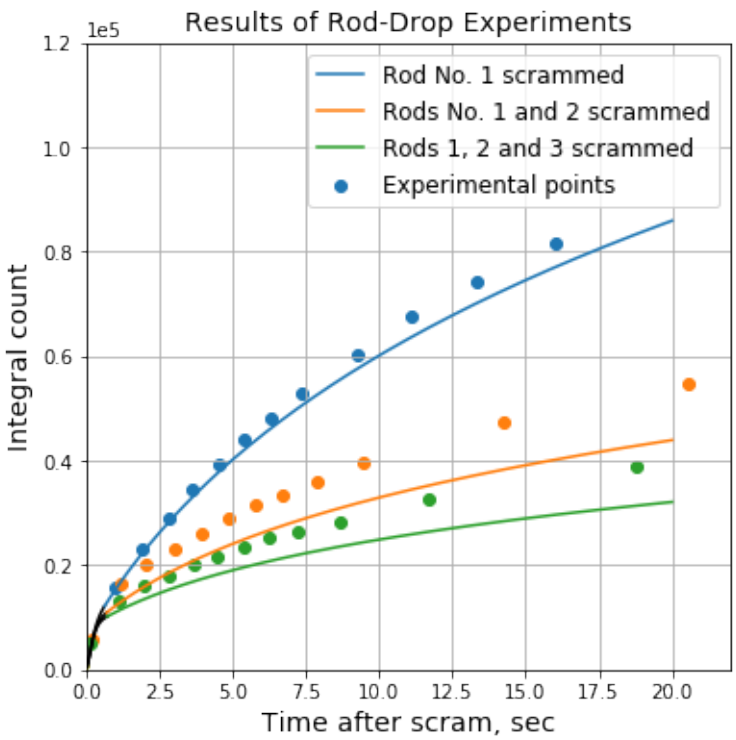

Figure 3.17: Results of rod-drop experiments after 30 capsule additions.

3.2.7 Rod-drop effects

Rod-drop experiments consisted of the simultaneous scram of the regulating rod group from its initial critical position. The integrated count as a function of time following the drop was recorded in the experiment.

Using the method described in Chapter 2, a code-to-experiment comparison of the rod-drop effect was conducted as shown in Figure 3.17 and Figure 3.18. As described above, the magnitude of the negative reactivity insertion of different rod groups ranging from the initial critical position to the scram position (-4 in.) and β_{eff} were determined by the Serpent2 model. The critical positions of the rod group with various ^{235}U concentration was obtained by method of linear regression using the position vs reactivity curve.

Accuracy of this calculation is sensitive to the magnitude of the reactivity insertion at the scram position, which depends on the fuel salt composition during the experiment which was not provided directly. The fuel salt composition was obtained by adding a certain amount of fuel capsules to the initial critical composition therefore the amount of ^{235}U contained in each capsule needs to be carefully checked. Also, the result is sensitive to the effective lag time

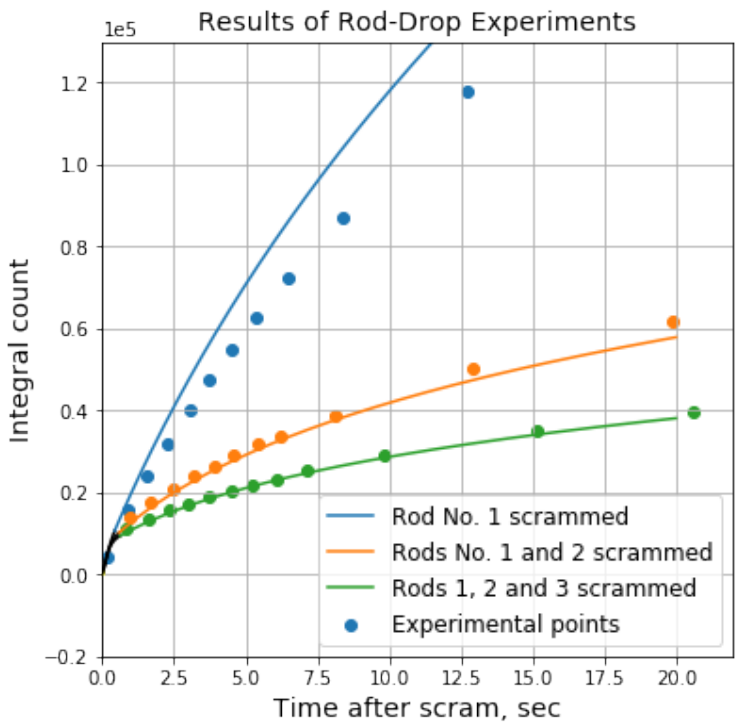

Figure 3.18: Results of rod-drop experiments after 65 capsule additions.

between scram signal and start of the rod drop, the initial count rate and the acceleration of rod-drop.

The discrepancy of the calculated result and the experimental data yields no uniform behaviour in different cases. The discrepancy may originate from calculating the initial critical position of the regulating rod group with various ^{235}U loadings, but such important information was provided in the MSRE reports. From previous calculations of rod bank worth (see Table 3.13) and the integral worth curve of rod No. 1 (see Figure 3.8), the MSRE benchmark model was proved to be able to yield an accurate estimation of the control rod worth for a single rod or a rod group. In addition, the composition of the fuel salt with ^{235}U loading specified was proved to be practical according to the code-to-experiment validation of reactivity coefficient of ^{235}U (see Table 3.11). Therefore, there may be a problem or inconsistency between the expected and as-built/actual amount of ^{235}U contained in each fuel capsule, which led to the inaccuracy of fuel salt composition representation in the rod-drop benchmark model.

3.2.8 Temperature reactivity effects

The benchmark model temperature is 922 K and it was varied ±50 K at three various ^{235}U loadings in the loop. The change in the reactor core geometry was considered with the change of temperature according the thermal expansion coefficients of materials. Both the temperature and density changes were considered for all materials inside the reactor vessel. All control rods were fully withdrawn. The calculated values for isothermal temperature coefficients at three ^{235}U loadings are provided in Table 3.15. The calculated values are slightly smaller than the benchmark value but they agree within 1σ. There's no obvious relationship between the ^{235}U loading in the fuel salt and the isothermal temperature coefficient.

Table 3.15: Isothermal temperature coefficient

^{235}U in loop, kg	Calculated value, °F^{-1}	Benchmark value, °F^{-1}	C/E
67.86	$-(6.95 \pm 0.13) \times 10^{-5}$	$-(7.45 \pm 0.85) \times 10^{-5}$	0.93 ± 0.11
69.85	$-(6.69 \pm 0.13) \times 10^{-5}$	$-(7.24 \pm 0.83) \times 10^{-5}$	0.92 ± 0.11
71.71	$-(6.56 \pm 0.13) \times 10^{-5}$	$-(7.30 \pm 0.83) \times 10^{-5}$	0.90 ± 0.10

To calculated the fuel salt temperature coefficient, only the fuel salt temperature was varied ±50 K in the system. The density of the fuel salt was adjusted with the change of temperature. All three control rods were fully withdrawn. The ^{235}U loading was arbitrarily chosen as the initial critical amount. The calculated value of the fuel temperature coefficient is provided in Table 3.16. The calculated value is slightly smaller than the benchmark value, similar to the bias of isothermal temperature coefficient calculation, but they agree within 1σ.

Table 3.16: Fuel temperature coefficient

Calculated value, °F^{-1}	Benchmark value, °F^{-1}	C/E
$-(4.30 \pm 0.14) \times 10^{-5}$	$-(4.7 \pm 0.7) \times 10^{-5}$	0.92 ± 0.14

3.3 Conclusions

A set of MSRE benchmarks was created basing on the first zero-power criticality experiment and the series of control rod calibration experiments performed at the MSRE in 1965. The fully-detailed benchmark model for the MSRE, using Monte Carlo code Serpent2, was utilized to analyze the effective multiplication factor when ^{235}U was progressively added to the fuel salt in order to achieve criticality with stationary salt and isothermal conditions.

The calculated multiplication factor in such conditions was 1.02132 (±3 pcm). The total uncertainty for experimental k_{eff} was estimated to be 420 pcm.

Basing on the Serpent2 model of the MSRE, new methods were developed to analyze the reactivity effects and reactivity coefficients measurement. An uncertainty of 2% was attributed to the reported reactivity measurements from experimenters and it was believed that the uncertainty of reactor period measurement contributed the most of the experimental uncertainty. An addition 2% uncertainty was added to all reactivity measurements to represent the uncertainty for the correction factor applied to pull all the measurements on the same uranium concentration and this uncertainty was reasonably inferred by evaluating this factor on the MSRE benchmark model. The calculated reactivity equivalent of ^{235}U additions (0.2228 ± 0.0014, represented as the change of reactivity over the relative change of ^{235}U mass in loop) matches well with the experiment value (0.223 ± 0.006), strengthening the confidence of accurate representation of the fuel salt composition in the MSRE model. Most of other calculations, including the control rod bank worth, reactivity effects of fuel circulation and isothermal and fuel temperature coefficients show good agreement with experiment values (within 1σ) as well.

Chapter 4

Code-to-Code Verification: Benchmark of Fluoride-Salt-Cooled Reactors

4.1 Introduction

Fluoride-salt-cooled high-temperature Reactors (FHRs) are a relatively new reactor concept, employing the same TRISO coated fuel particles used in many high temperature gas-coolant reactors (HTGRs) (see Figure 1.1) with fluoride salt as the coolant. There are a few different designs for fuel assemblies or elements, including pebbles, plates and prismatic blocks. The FHR with a pebble bed geometry is of great interest. To date, no fueled experiments using pebbles immersed in salt have been conducted.

The U.S. Department of Energy awarded a three year Integrated Research Project (IRP) to four universities, including the University of California at Berkeley, to address major challenges in developing commercial FHRs. In the scope of the IRP, to understand and model the core neutronics for FHRs, a code-to-code comparison/verification benchmark was created by the University of California, Berkeley, aiming to verify the credibility of neutronics codes in modeling reactors with TRISO particle type fuel and a pebble bed geometry.

As a reference code-to-code comparison benchmark with pebbles, the Pebble-Bed Modular Reactor (PBMR) "Pebble Box" benchmark included in IAEA-TECDOC-1694[17] is of particular interest, which consists of a number of test cases on a $1\,m^3$ pebble box with clearly defined material and conditions to investigate the effects of scattering and steaming of neutrons throughout the core and the treatment of thermal neutrons on the core-reflector interface. The design of test cases for the IRP FHR neutronics benchmark are very similar to the Pebble Box benchmark, both of which start with a simple, infinite cell containing pebbles and is examined with varying levels of homogenization. This allows some quantification of

the resonance self-shielding and neutron streaming effects. The second benchmark scenario includes a graphite reflector and black boundaries to simulate a simplified reactor geometry, allowing for quantification of leakage and reflector effects.

4.2 Unit cell model

The unit cell model benchmark focuses on the neutronics physics behavior of a Face-Centered Cubic (FCC) unit cell system which consists of three cases:

- Case 1: the homogeneous mixture case which is a cube unit cell with a side length of 9.2575 cm filled with a homogeneous mixture of coolant and pebble components;
- Case 2: the single level heterogeneity case which is a cube unit cell filled with pebbles and coolant (as shown in Figure 4.1);
- Case 3: the double level heterogeneity case where the inner fuel region of pebbles is filled with particles and graphite matrix (as shown in Figure 4.2).

The dimensions of TRISO particles used in the double heterogeneity case is provided in Table 4.1 and material information is provided in Table 4.2. Pebbles are comprised of an inner fuel region and a shell. The inner fuel region of pebbles is comprised of 11558 fuel particles and graphite matrix. The packing factor of fuel particles is 6.97%. The temperature is set to 900 K. The Li-7 enrichment is 99.99%.

Table 4.1: Geometry information of TRISO particles

Property	Value
Centre fuel kernel radius	0.025 cm
Buffer layer thickness	0.009 cm
Inner PyC layer thickness	0.004 cm
SiC layer thickness	0.0035 cm
Outer PyC layer thickness	0.004 cm
Particle radius	0.0455 cm

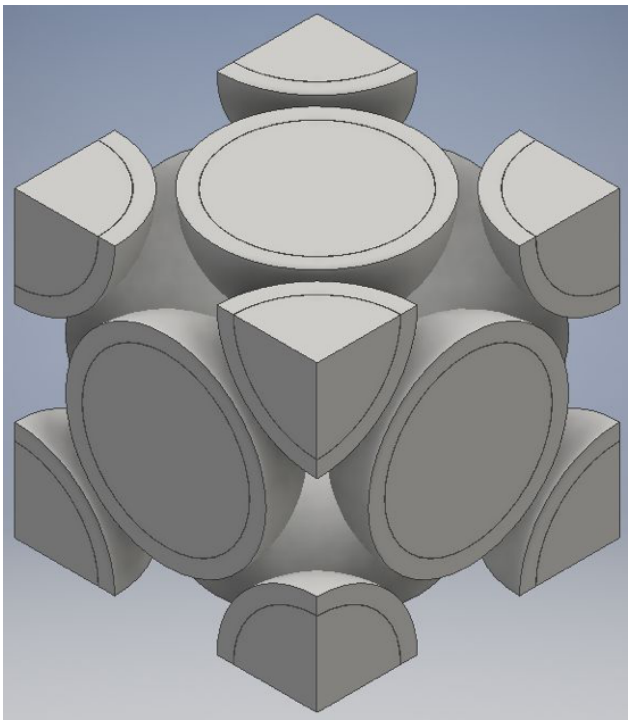

Figure 4.1: Configurations of the single level heterogeneity case. The pebbles are comprised of a homogeneous inner fuel region and a carbon shell. The radius of pebbles is 3 cm, the radius of their inner fuel region is 2.5 cm and the side length of the cube unit cell is 9.2575 cm, generating a packing factor of 57.02% to be consistent with the full-core model. The space among pebbles is filled with FLiBe coolant.

Table 4.2: Material used in the double level heterogeneity case

Material	Density, g/cm^3
Fuel, UO_2	10.5
Buffer layer, C	1.05
PyC layer, C	1.90
SiC	3.18
Matrix (shell), C	1.73
FLiBe	1.9740

The following parameters are expected to be calculated by different codes to compare:

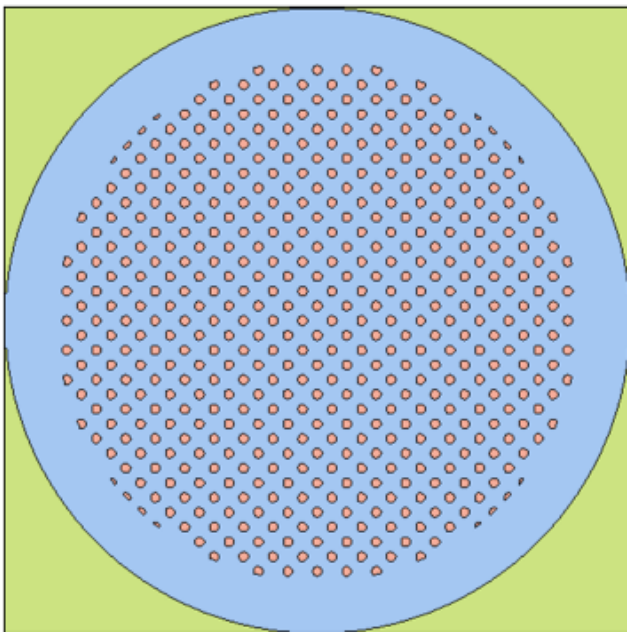

Figure 4.2: Configurations of the pebble in the double level heterogeneity case. The radius of fuel particles is 0.0455 cm. For the ordered particles, the side length of the particle FCC lattice is 0.2828 cm.

- the effective multiplication factor, k_{eff};
- the effective delayed neutron fraction, β_{eff};
- the prompt neutron generation time, Λ, and lifetime, l;
- neutron spectrum;
- 4-group microscopic cross section for selected reactions.

A reference result was calculated by Serpent2 with ENDF/B-VII.0 cross section library. Thermal scattering library was used for carbon. As shown in Table 4.3, due to the homogenization approach of the pebble region and the full unit cell, the k_{eff} decreased, the β_{eff} increased, the prompt neutron generation time increased while the prompt neutron lifetime decreased from Case 3 to Case 1, with the spatial self-shielding effect fading away. The neutron spectrum for different cases and for different regions in the unit cell model are plotted in Figure 4.3 and Figure 4.4. Due to the homogenization approach of this unit cell model, the neutron spectrum was hardened slightly.

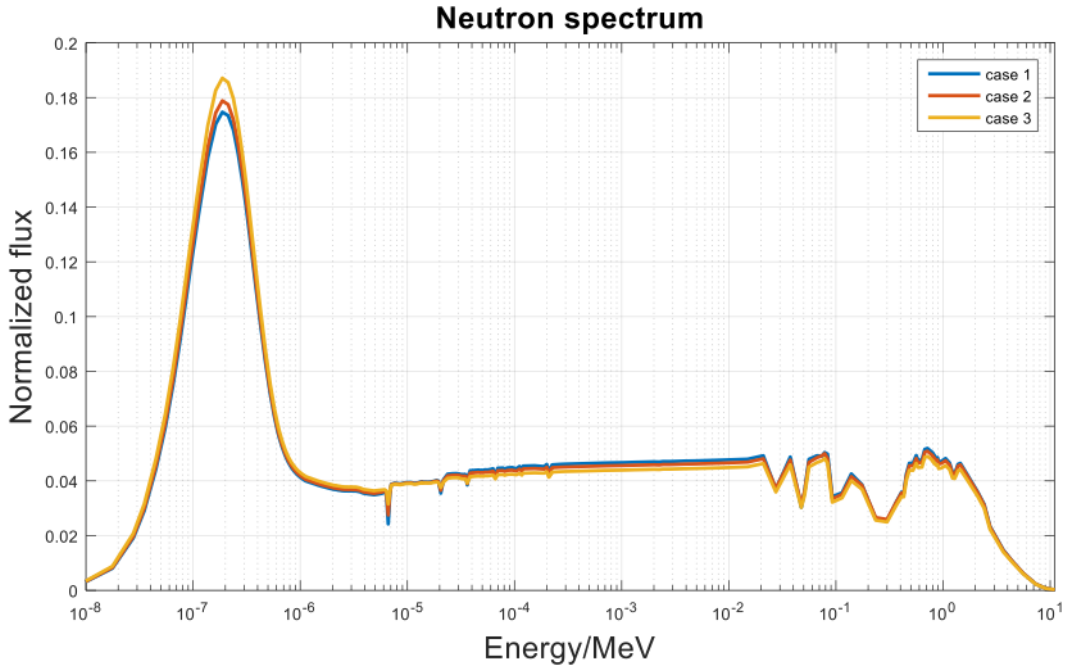

Figure 4.3: Average neutron spectrum for FHR unit cell models.

Table 4.3: Calculation results of FHR unit cell models

	Case 1	Case 2	Case 3
k_{eff}	1.30504 ± 0.00003	1.34638 ± 0.00004	1.42187 ± 0.00004
β_{eff}, pcm	651.08 ± 0.58	650.99 ± 0.57	648.76 ± 0.54
Λ, μs	288.46 ± 0.03	283.16 ± 0.03	274.49 ± 0.03
l, μs	376.45 ± 0.03	381.19 ± 0.03	390.27 ± 0.03

4.3 Full core model

The second stage of this benchmark development is a simplified model of the TMSR-SF1 core, developed by the Shanghai Institute of Applied Physics. The FHR full core benchmark model is designed to be a solid fuel molten salt cooled high-temperature reactor. It uses 6.0-cm-diameter spherical fuel elements, which contains 17.12 wt. % uranium. The coolant of primary loop is 2LiF-BeF_2 molten salt. The temperature is set to 900 K. The layout of the core is shown in Figure 4.5.

The cylinder core includes a middle cylinder active region, top reflector, bottom reflector

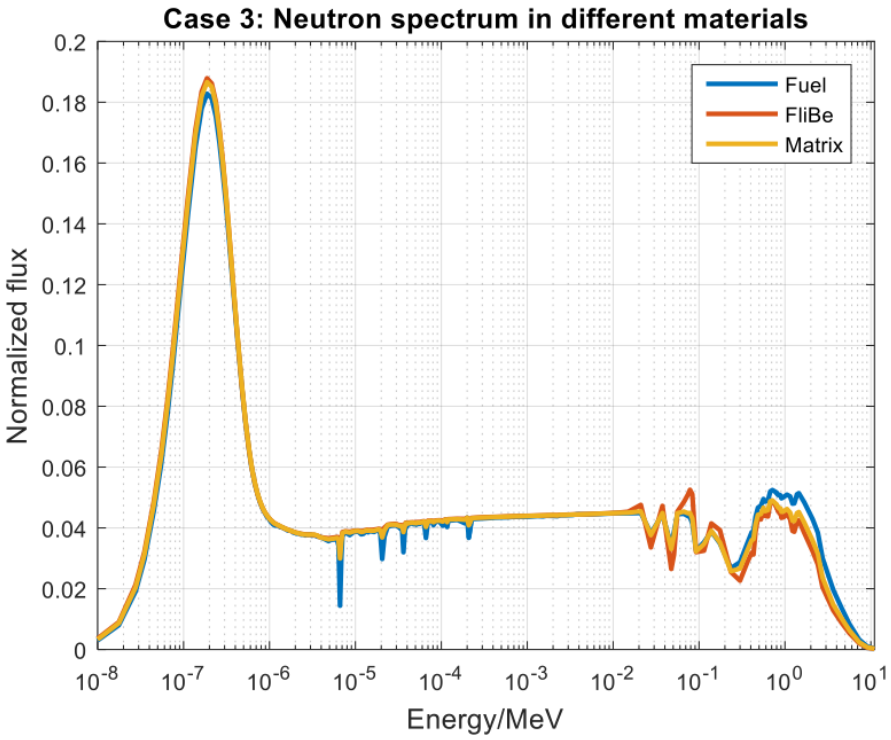

Figure 4.4: Neutron spectrum in different materials in the double heterogeneity case.

and radial reflector. Top and bottom reflectors, with a diameter of 135 cm and height of 50.35 cm, are mixture of graphite and coolant. For the top reflector, the volume ratio of FLiBe and graphite is around 1:3.70 and for the bottom reflector, the volume ratio of FLiBe and graphite is around 1:3.08. The radial reflector, with an outer diameter of 285 cm and height of 306.4 cm, is made of pure graphite. The active region, with a diameter of 135 cm and height of 205.7 cm, consists of a fuel region and a pure coolant region. Fuel pebbles are distributed randomly in the fuel region with a packing factor of 57.02%, which is the upper section of active core. The gap among pebbles and the bottom section of active core are filled by coolant.

The model includes 7168 pebbles, the number required to achieve criticality using a random packing with a fresh core and no control elements. Besides using explicitly defined pebble locations, a regular lattice of the FCC arrangement was used as well to investigate the effect of randomization of pebbles. Due to the regular lattice, the pebbles on the periphery of the core were cut and the exact fuel volume was not known. The pitch of the particle lattice was first tweaked so that the effective particle packing factor was maintained. Following that, the pitch of the pebble lattice was iterated to preserve the nominal pebble packing factor. As such, it should be noted that the lattice used in the unit cell and the simplified full core

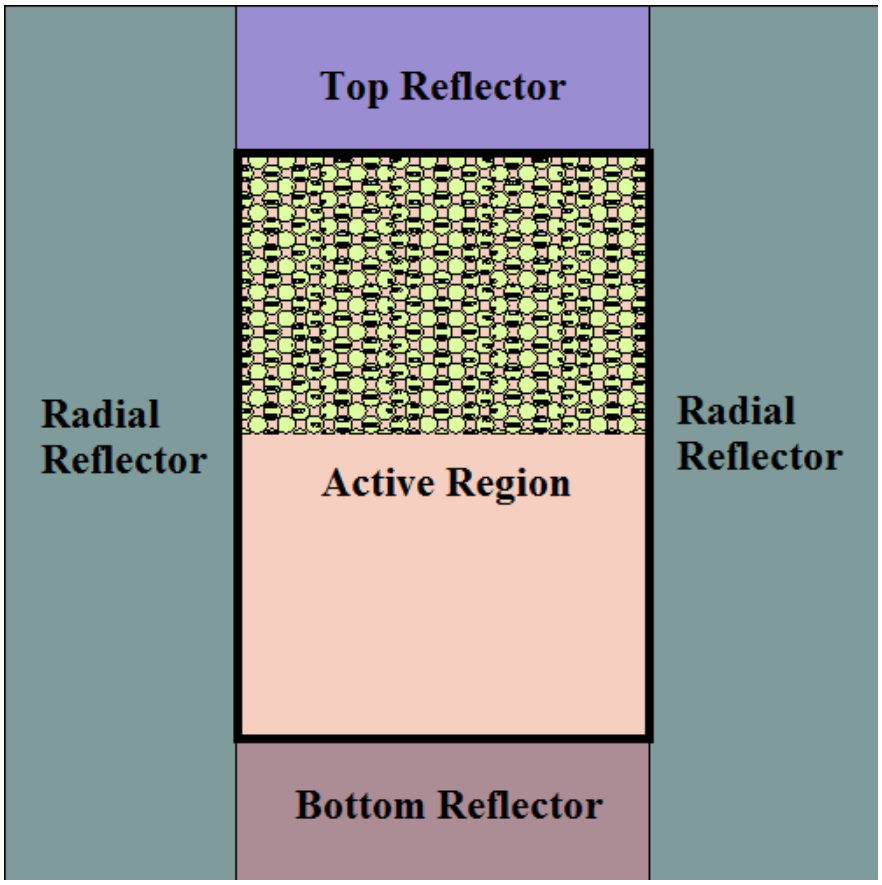

Figure 4.5: Vertical section of the FHR full core benchmark model.

model are very similar, but not identical.

The following parameters are expected to be calculated by different codes to compare:

- the effective multiplication factor, k_{eff};
- the effective delayed neutron fraction, β_{eff};
- the prompt neutron generation time, Λ, and lifetime, l;
- neutron spectrum, especially in the fuel region inside kernels;
- radial and axial leakage;
- power flux spectrum in different locations;

- reactivity coefficients.

The density of FLiBe is calculated by the following formula where the unit of temperature T is °C:

$$\rho(\mathrm{kg/m^3}) = 2279.92 - 0.488 \times T \tag{4.1}$$

A reference result was calculated by Serpent2 with ENDF/B-VII.0 cross section library. Thermal scattering library was used for carbon. The calculated k_{eff}, β_{eff}, Λ and l are provided in Table 4.4. The randomization of pebbles and particles led to a 728 pcm increase of k_{eff} and obvious decrease of the prompt neutron generation time and lifetime.

The neutron leakage from radial, top and bottom of the core with ordered pebbles and TRISO particles were calculated to be 11.46%, 5.64% and 0.16%. Figure 4.6, Figure 4.7, Figure 4.8 and Figure 4.9 plot the thermal flux distribution in detail. There are peaks in thermal flux within the reflector regions, radially or axially, since fast neutrons that enter the reflector are effectively moderated to thermal neutrons in the reflector. The calculated reactivity coefficients are summarized in Table 4.5.

Table 4.4: Calculation results of FHR full core models

	Ordered pebbles and particles	Random pebbles and particles
k_{eff}	0.993376 ± 0.00008	1.00066 ± 0.00008
β_{eff}, pcm	677.81 ± 0.75	676.69 ± 0.73
Λ, μs	666.77 ± 0.13	639.13 ± 0.12
l, μs	667.13 ± 0.19	644.24 ± 0.19

Table 4.5: Calculation results of reactivity coefficients

Doppler, pcm/K	Coolant, pcm/K	Void, pcm/K
-2.22 ± 0.04	-1.67 ± 0.04	-11.07 ± 2.35

4.4 Code-to-code comparison

For a code-to-code verification benchmark, the identification of modeling issues and other simulation phenomena is important. There are two primary methodologies to rebuild the

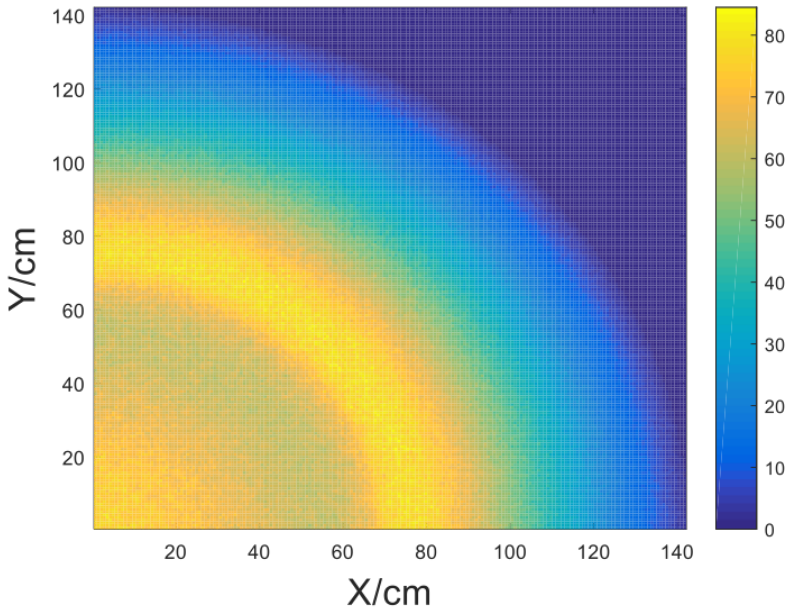

Figure 4.6: Thermal flux in X-Y plane of the FHR full core benchmark model.

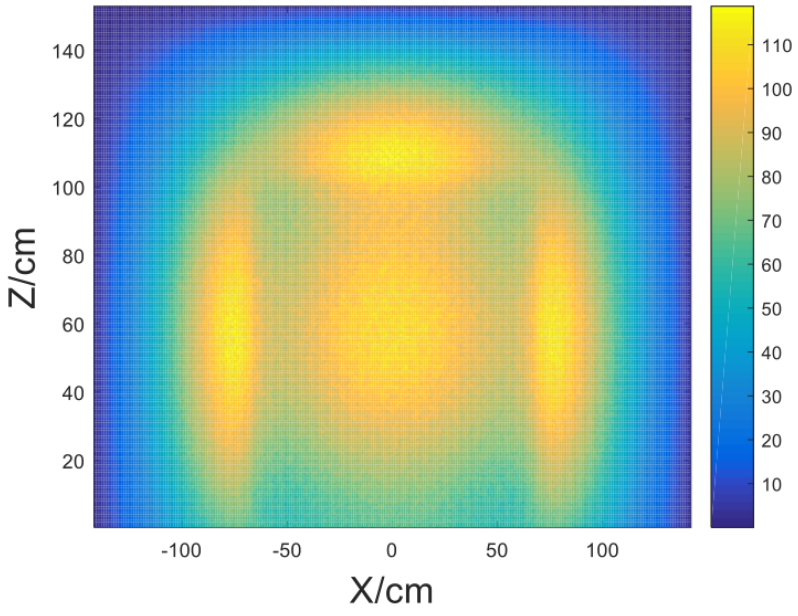

Figure 4.7: Thermal flux in X-Z plane of the FHR full core benchmark model.

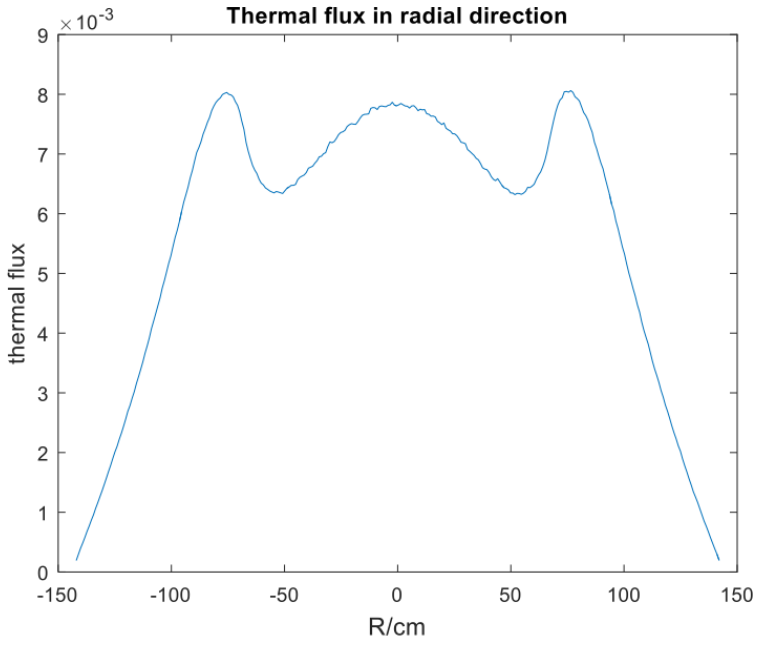

Figure 4.8: Radial thermal flux of the FHR full core benchmark model.

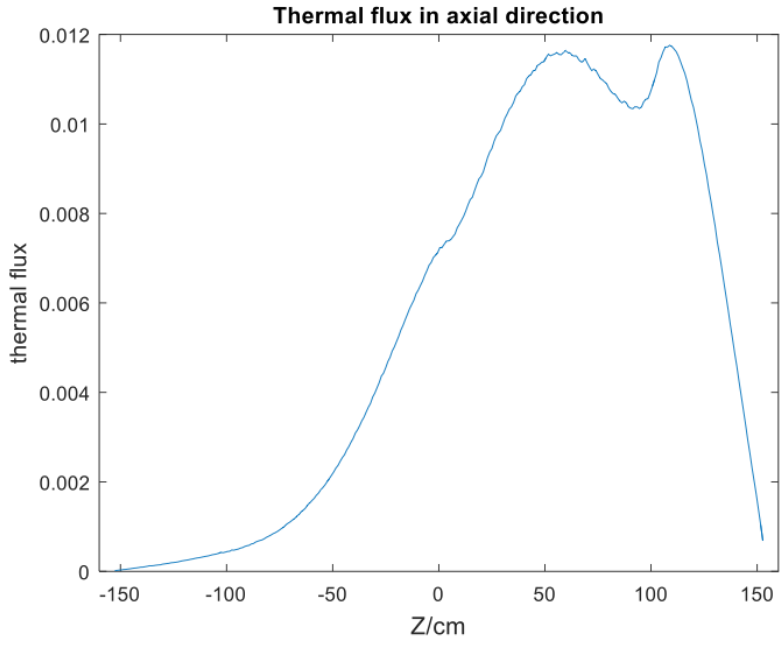

Figure 4.9: Axial thermal flux of the FHR full core benchmark model.

benchmark model and calculate parameters of interest defined by the benchmark specification: deterministic and stochastic. Compared to the traditional deterministic approach, the stochastic approach, also called Monte Carlo method, offers a higher-fidelity and flexible simulation, avoiding making many approximations necessary to solve the problems. Especially in models with TRISO/pebble fuels, the stochastic approach is a better option that can balance the high fidelity and high flexibility in building the complex geometry.

[15] summarizes the code-to-code comparison results utilizing the series of FHR neutronics benchmark described above. MCNP6 and SCALE6.1 were used to compare with Serpent2 calculations. The main conclusions were summarized here:

- For unit cell models, the k_{eff} results generally agree well among all codes utilizing continuous energy mode. There's a 250-300pcm difference exists between the continuous energy mode and the multi-group mode in Case 1 and Case 2, while in Case 3 the difference vanishes. The effective delayed neutron fraction, prompt neutron generation time and lifetime calculated by Serpent 2 and MCNP6 agree well with each other.
- For the full core models, the k_{eff} calculated by MCNP6 and SCALE6.1 are about 400 pcm lower than Serpent2. The neutron leakage, reactivity coefficients calculated by Serpent2 and MCNP6 agree well with each other. Figure 4.10 and Figure 4.11 show comparisons of thermal neutron flux calculated by Serpent2 and MCNP6 and there's a good agreement as well.

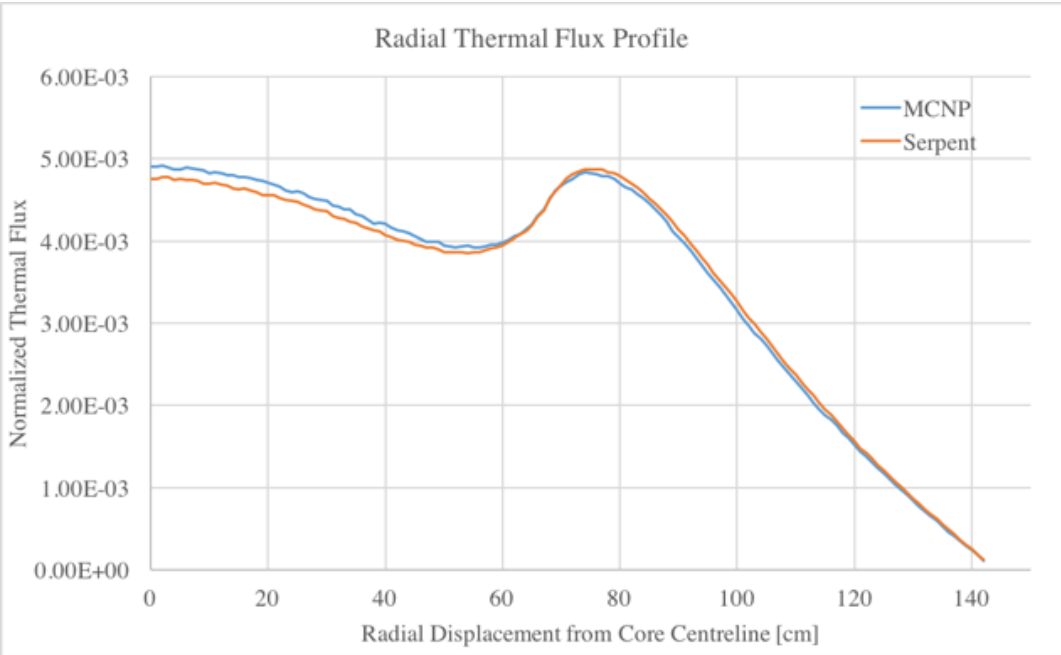

Figure 4.10: Comparison of radial thermal neutron flux calculated by Serpent2 and MCNP6.

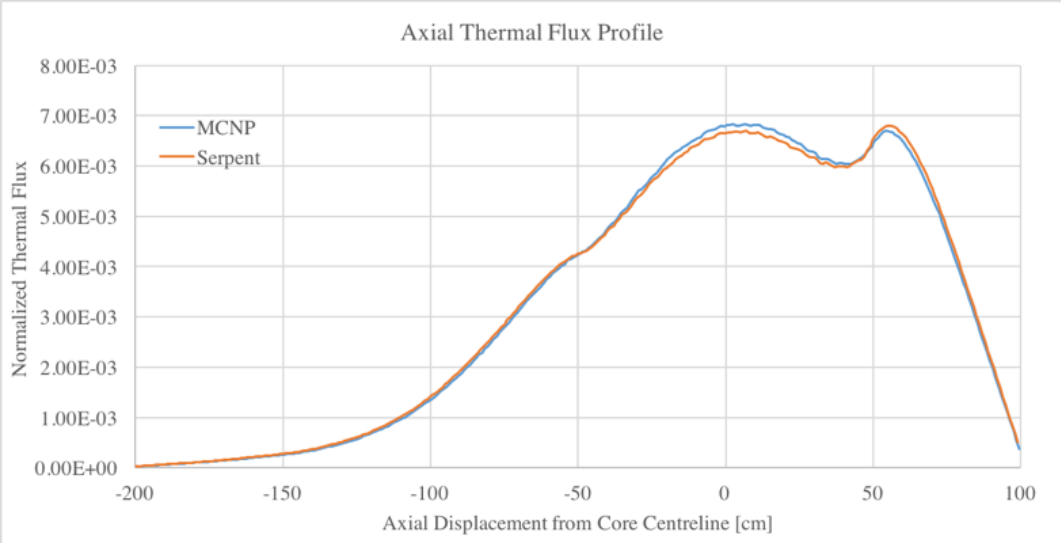

Figure 4.11: Comparison of axial thermal neutron flux calculated by Serpent2 and MCNP6.

Chapter 5

Conclusions and Future Work

This dissertation investigated the computational code validations for MSRs in order to support the licensing process of this reactor technology. The world-first, MSR-related reactor physics benchmark was created basing on the series of zero-power experiments of the MSRE for the IRPhEP handbook by the University of California, Berkeley collaborated with ORNL, the place where the MSRE was designed and operated. This benchmark effort will fill the knowledge gap of MSR benchmarking.

The three-dimensional high-fidelity benchmark model for use in the MSRE benchmark was developed with Monte Carlo neutron transport code Serpent2 and multiple nuclear data evaluations (ENDF/B.VII and JENDL). To accurately model reactivity effect experiments of the MSRE, new methods were developed basing on the Serpent2 model to account for, for example, the unique feature of fuel salt motion in the core.

The calculated multiplication factor for the criticality experiment, when ^{235}U was progressively added to the fuel salt in order to achieve criticality with stationary salt and isothermal conditions, was 1.02132 ($\pm$3 pcm). The total uncertainty for experimental k_{eff} was estimated to be 420 pcm. The calculated k_{eff} is 2.154% larger than the experimental and benchmark model value, which is approximately 5 times the benchmark model uncertainty. Such bias is not uncommon in benchmarks of systems containing large volume of graphite (or other carbonaceous materials). According to the IRPhEP handbook[4], the calculated k_{eff} is 1.190% larger than the expected value for HTR10. For HTTR, the calculated k_{eff} is 2.03% larger than the expected value. The bias is possibly due to uncertainties in the impurity content of the graphite blocks, the accuracy of the neutron capture cross section of carbon and the accuracy to model the nuclear-grade graphite.

Uncertainty quantification is the essential part of an IRPhEP benchmark, the uncertainty caused by each important parameter in the benchmark model was evaluated independently. Also, with the new features developed in Serpent2, the sensitivity coefficients and total un-

certainty for the k_{eff} from nuclear data uncertainties in each element in all the materials were quantified. An uncertainty of 2% was attributed to the reported reactivity measurements from experimenters and it was believed that the uncertainty of reactor period measurement contributed the most of the experimental uncertainty. An addition 2% uncertainty was added to all reactivity measurements to represent the uncertainty for the correction factor applied to pull all the measurements on the same uranium concentration and this uncertainty was reasonably inferred by evaluating this factor on the MSRE benchmark model. The calculated reactivity equivalent of ^{235}U additions (0.2228 ± 0.0014, represented as the change of reactivity over the relative change of ^{235}U mass in loop) matches well with the experiment value (0.223 ± 0.006), strengthening the confidence of accurate representation of the fuel salt composition in the MSRE model. Most of other calculations, including the control rod bank worth, reactivity effects of fuel circulation and isothermal and fuel temperature coefficients show good agreement with experiment values (within 1σ) as well.

A code-to-code verification benchmark for FHR was also introduced to illustrate the scenario of building a benchmark for conceptual MSRs without fueled experiments to compare.

Based on the time and resources available for this project, the produced benchmark will be limited to the zero-power experiments concerning criticality and reactivity effects under various conditions with ^{235}U molten salt fuel. Nevertheless, the baseline developed in this benchmark, such as the system model and the simulation tools, can serve as a foundation for future extensions that will cover other experimental campaigns carried at the MSRE, for example, in order to understand reactor dynamics of the MSRE and the behavior of the system with ^{233}U loaded.

The MSRE benchmark model will be calculated by different Monte Carlo codes to make code-to-experiment validations, strengthening the confidence to the capability of these codes or figuring out the area of improvement. Also, it can be used to test various nuclear cross section data, such as ENDF/B.VIII.0, as a baseline of graphite-moderated molten salt reactor.

Bibliography

[1] Manuele Aufiero et al. "Calculating the effective delayed neutron fraction in the molten salt fast reactor: analytical, deterministic and Monte Carlo approaches". In: *Annals of Nuclear Energy* 65 (2014), pp. 78–90.

[2] Manuele Aufiero et al. "A collision history-based approach to sensitivity/perturbation calculations in the continuous energy Monte Carlo code SERPENT". In: *Annals of Nuclear Energy* 85 (2015), pp. 245–258.

[3] Briggs Blair, E Sartori, L Scott, et al. "The International Reactor Physics Experiment Evaluation Project (IRPhEP)". In: (2006).

[4] J Blair Briggs, John D Bess, and Jim Gulliford. "Integral benchmark data for nuclear data testing through the ICSBEP & IRPhEP". In: *Nuclear Data Sheets* 118 (2014), pp. 396–400.

[5] R.B. Briggs. *Molten-Salt Reactor Program Semiannual Progress Report ORNL-3626*. Tech. rep. Oak Ridge National Lab., Tenn, 1964.

[6] Re B Briggs. "Molten-salt reactor program, semiannual progress report for period ending August 31, 1965". In: *ORNL* 3872 (1965), p. 127.

[7] US DoE. "A technology roadmap for generation IV nuclear energy systems". In: *http://gif. inel. gov/roadmap/pdfs/gen_iv_roadmap. pdf* (2002).

[8] Thomas James Dolan. *Molten salt reactors and thorium energy*. Woodhead Publishing, 2017.

[9] Charles W Forsberg, Per F Peterson, RA Kochendarfer, et al. "Design options for the advanced high-temperature reactor". In: *Proceedings of ICAPP*. Vol. 8. 2008, pp. 8–12.

[10] Charles W Forsberg, Per F Peterson, and Paul S Pickard. "Molten-salt-cooled advanced high-temperature reactor for production of hydrogen and electricity". In: *Nuclear Technology* 144.3 (2003), pp. 289–302.

[11] Minoru Goto, Satoshi Shimakawa, and Yasuyuki Nakao. "Impact of revised thermal neutron capture cross section of carbon stored in JENDL-4.0 on HTTR criticality calculation". In: *Journal of nuclear science and technology* 48.7 (2011), pp. 965–969.

[12] P.N. Haubenreich et al. *MSRE design and Operations Report: Part III. Nuclear Analysis*. Tech. rep. Oak Ridge National Lab., Tenn., 1964.

[13] Paul N Haubenreich and JR Engel. "Experience with the molten-salt reactor experiment". In: *Nuclear Applications and technology* 8.2 (1970), pp. 118–136.

[14] Jaakko Leppänen et al. "The Serpent Monte Carlo code: Status, development and applications in 2013". In: *SNA+ MC 2013-Joint International Conference on Supercomputing in Nuclear Applications+ Monte Carlo*. EDP Sciences. 2014, p. 06021.

[15] L Maul, D Shen, and M Fratoni. "Neutronics Code Benchmark of Fluoride-Salt-Cooled Reactors". In: *Trans. Am. Nucl. Soc., In Press* (2016).

[16] H.E. McCoy and B. McNabb. *Postirradiation examination of materials from the MSRE*. Tech. rep. Oak Ridge National Lab., Tenn., 1972.

[17] M Methnani and B Tyobeka. "Evaluation of High Temperature Gas Cooled Reactor Performance: Benchmark Analysis Related to the PBMR-400, PBMM, GT-MHR, HTR-10 and the ASTRA Critical Facility". In: *International Atomic Energy Agency, Vienna, Austria* (2013).

[18] Jeffrey J Powers and Brian D Wirth. "A review of TRISO fuel performance models". In: *Journal of Nuclear Materials* 405.1 (2010), pp. 74–82.

[19] B.E. Prince et al. *Zero-power physics experiments on the molten-salt reactor experiment, ORNL-4233*. Tech. rep. Oak Ridge National Lab., Tenn., 1968.

[20] B.E Prince, J.R Engel, and C.H Gabbard. *Reactivity balance calculations and long-term reactivity behavior with 235U in the MSRE*. Tech. rep. Oak Ridge National Lab., Tenn., 1972.

[21] R.C. Robertson. *MSRE design and operations report. Part I. Description of reactor design*. Tech. rep. Oak Ridge National Lab., Tenn., 1965.

[22] MW Rosenthal, PR Kasten, and RB Briggs. "Molten-salt reactors—history, status, and potential". In: *Nuclear Applications and Technology* 8.2 (1970), pp. 107–117.

[23] Raluca O Scarlat and Per F Peterson. "The current status of fluoride salt cooled high temperature reactor (FHR) technology and its overlap with HIF target chamber concepts". In: *Nuclear Instruments and Methods in Physics Research Section A: Accelerators, Spectrometers, Detectors and Associated Equipment* 733 (2014), pp. 57–64.

[24] Dan Shen et al. "Zero-power criticality benchmark evaluation of the molten salt reactor experiment". In: *Proceedings of the International Conference on Physics of Reactors. PHYSOR 2018, Cancun, Mexico, April 2018*. 2018.

[25] Roy E Thoma. *Chemical aspects of MSRE operations, ORNL. 4658*. Tech. rep. Oak Ridge National Lab., Tenn, 1971.

[26] G.M. Tolson and A. Taboada. *MSRE control elements: manufacture, inspection, drawings, and specifications*. Tech. rep. Oak Ridge National Lab., Tenn., 1967.

[27] Dalin Zhang et al. “Review of conceptual design and fundamental research of molten salt reactors in China”. In: *International Journal of Energy Research* 42.5 (2018), pp. 1834–1848.